A Search for the Evidence of Type-III Seesaw Mechanism in Multileptonic Final States at the LHC

A thesis
Submitted in partial fulfillment of the requirements of the degree of

Doctor of Philosophy

by:

Kunal Kothekar
Registration ID 20123224

Department of Physics
INDIAN INSTITUTE OF SCIENCE EDUCATION AND RESEARCH
PUNE-411008, India

February 2019

Certificate

Certified that the work incorporated in the thesis entitled **"A Search for the Evidence of Type-III Seesaw Mechanism in Multileptonic Final States at the LHC"** submitted by **Kunal Kothekar** was carried out by the candidate, under my supervision. The work presented here or any part of it has not been included in any other thesis submitted previously for the award of any degree or diploma from any other university or institution.

Date: May 5, 2018 (Supervisor)

Declaration of Authorship

I hereby certify that the work which is being presented in the thesis entitled **"A Search for the Evidence of Type-III Seesaw Mechanism in Multileptonic Final States at the LHC"** in partial fulfillment of the requirements for the award of the Degree of **Doctor of Philosophy** and submitted in the Department of Physics of the Indian Institute of Science Education and Research Pune is an authentic record of my own work carried out during a period from August, 2012 to May, 2018 under the supervision of Dr. Sourabh Dube, Assistant Professor, Department of Physics, Indian Institute of Science Education and Research Pune. The matter presented in the thesis has not been submitted by me for the award of any other degree of this or any other institute.

Date: April 5, 2017 (Kunal Kothekar)

"Somewhere beyond the sink-hole, past the magnolia, under the live oaks, a boy and a yearling ran side by side, and were gone forever."

Marjorie Kinnan Rawlings, The Yearling (1938)

Abstract

The standard model(SM) of particle physics is an experimentally tested successful theory of the modern physics era. However there exist phenomena which the SM does not describe. Among others, the neutrino mass hierarchy which has been observed by experiments like Super-Kamiokande has no explanation in SM. This requires an extension or perhaps new physics beyond the SM. One of the extensions for the standard model, type-III seesaw mechanism introduces a fermionic triplet, which can explain why the neutrino masses are small and why they indeed have the mass hierarchy. The fermionic triplet in type-III seesaw mechanism decays to the multileptonic final state via electroweak interactions. The multileptonic final decay has an advantage of being rare, relative to other standard model backgrounds.

In my thesis, I have undertaken a search for type-III seesaw signal in events with 3 or more leptons (e, mu, and tau). The data on which this search has been performed corresponds to 35.9 fb^{-1} of integrated luminosity in pp collisions at $\sqrt{s} = 13$ TeV collected by the CMS experiment at the LHC. Since the signal populates channels with at least three leptons and diverse kinematic properties, the data is binned in exclusive channels. The primary selection is based on the number of leptons and the invariant mass of opposite-sign dilepton systems which helps discriminate the signal against the Standard Model background. The final optimization for the type-III seesaw signal is based on the sum of leptonic transverse momenta and missing transverse energy. Control samples in data are used to check the robustness of background evaluation techniques and to minimize the reliance on simulation. The observations are consistent with expectations from Standard Model processes. No sign of type-III seesaw fermion production is observed. The results are used to exclude heavy fermions of the type-III seesaw model with masses below 840 GeV.

Acknowledgements

An acknowledgment for any thesis starts with the heartfelt gratitude towards the guide, he/she can never be appreciated enough for the central role they play in graduate students work. My fondness for Prof. Sourabh Dube, though cannot be described in these thankful words. He has played a pivotal role not only in my graduate work but all aspects of my life making me a better person than I was and most importantly a humble human being. I will carry not only the physics training but that extra ounce of positivity from him, forever with me.

Speaking of the physics training, Prof. Seema Sharma has been a great mentor and played a major role in my education. Her no-nonsense attitude has always compelled me to put forward my best foot. I can not thank her enough. These two wonderful people brought a balance in my training and at a time kept me in check too. What can I say more, I was lucky enough to be the first (and a tricky one) student to both of them and was always extra-spoiled by their lovely attention.

I am thankful to Prof. Sunil Somalwar and wonderful people at Rutgers University including Halil, Maxi, Peter, Matt who all are present/past members of the multilepton group, for the collaborative effort of multilepton analysis which has resulted in this thesis.

Shubhanshu, Anshul and I joined the newly founded EHEP group, one after another and almost at the same time. Since then we are partners in almost every aspect of our work-life, be that a daily coffee ritual or relaxed outing or even occasionally full-blown arguments. This analysis has their equal efforts. Thank-you guys for everything and I wish a great future to you. A special thanks are also due to Angira, our newest addition to the multilepton group, for all the help she provided me in the last round. The EHEP group is one of the busy bee's of IISER Pune in terms of productivity, and I feel grateful to have the choicest company of all the EHEP members including Vinay, Aditee, Shubham, and Bhumika. I wish a great future to all of them.

Coming to the physics department of IISER Pune, I am grateful to my research advisory committee members Prof. Bhas Bapat and Prof. Rejish Nath, for their meaningful inputs throughout this work. Invaluable time has been saved by Prabhakar, Dhanashree, Santosh, and Prashant by their immense help in administrative tasks; these guys made sure the conferences were fun enough for us by taking out the boring tasks themselves. The physics department of IISER Pune is a great place to work, there is informality in the air, people are enthusiastic, and no extra effort is needed for the spot-on collaboration. I feel grateful to be part of such a wonderful community and wish best to them for the future.

I also wish to express my gratitude towards IISER Pune for all the financial support and kick-starting my science career. There are no dearth of words by many great people for CERN and CMS collaboration which I am part of, I can just give my humble thanks to them for making this analysis possible.

This acknowledgment cannot be completed without the mention of my friends. Rohan, Pankaj, Manish, Jeetu, and Prateek were with me before I embarked on this journey and they all chipped in to make sure that I complete this one. Aditya, Ravi, Nandi, Sunil, provided an eventful Ph.D. life and everlasting memories. Sneha made certain that no sun-sets were ever lonesome in this long journey. Thank-you guys for making this possible.

The last word goes for my mother, father, and brother whose relentless never-ending support kept me floating. My brother Bhushan's belief and credit card never maxed out on me. Guys, you are everything to me.

Contents

List of Figures

List of Tables

For all S, B & K's in my life...

Chapter 1

Introduction

"*Why do humans do science? Why do they do art? The things that are least important for our survival are the very things that make us human.*"
–Savas Dimopoulos

"*The history of atomism is one of reductionism- the effort to reduce all the operations of nature to a small number of laws governing a small number of primordial objects.*"
–Leon M. Lederman

Modern particle physics is the quintessential branch of physics which deals with the questions very fundamental by nature, "where did universe come from?", "what is everything made up of?" to name a few. It's a relatively modern branch of physics and in the last 50–60 years has seen a tremendous development in this subject. One of the most significant accomplishments of this field is the standard model(SM) of particle physics. The standard model of particle physics is a collection of theories which describes the elementary particles and their interactions through the electromagnetic, the weak and the strong forces. Evolved in the 1960s, the SM has proven to be astonishingly robust and has stood the test of time. It has been verified by a number of experiments with great precision; the final piece of the puzzle the Higgs boson was discovered at the large hadron collider (LHC) by two of its experiments ATLAS and CMS in the year 2012. With this discovery, the SM has truly become the most prominent milestone of the modern era physics.

From 1967 to 2012, experimental particle physics has been guided by the standard model. This era also has seen experimental particle physics shifting to higher energies, more massive accelerators, big detectors, so much so that it has come to known as experimental high energy physics. The were many notable experiments during this period which provided breakthrough's and verified the predictions of the SM. Chief among them

were, SPS(Super Proton Synchrotron) at CERN, Collider Detector at Fermilab(CDF), DESY, etc. paving ways for breakthrough discoveries of principal constituents of the standard model such as W, Z boson, tau lepton, top quark to name a few. The most recent effort being the LHC, hailed as world's largest and most powerful particle collider, which firmly established the SM with its discovery of Higgs boson in 2012.

For all its importance and being hugely successful in describing the elementary particles and their interaction, the SM does not represent the complete picture. There are various shortcomings of the SM both conceptual (omission of gravity, gauge hierarchy, free parameters, etc.) and observational (for example, dark matter and energy, neutrino oscillation.) level, which creates need for a look beyond the standard model of particle physics. There are various proposals extending the standard model and also candidate theories beyond the standard model. As an experimentalist one's job is to examine and test the creative theories put forward by the particle physics community.

The tool required for such an experimental verification and bring these theories within reach is readily provided by LHC. The LHC at the European Organization for Nuclear Research (CERN) has been designed and built to collide protons and heavy ions at the highest energies available, and is instrumented with four major detectors, the CMS, ATLAS, ALICE, and LHCb detectors. The LHC scientific program was launched in 2008, eventually reaching 7 TeV center-of-mass energy in proton-proton collisions in 2010, and 8 TeV in 2012. Since the Higgs boson discovery of 2012, LHC is now chiefly looking at the data for the hint of physics beyond the standard model. After the technical stop of two years, since 2015 the LHC has started colliding protons at the unprecedented new frontier of 13 TeV center-of-mass energy. A modern-day approach in experimental particle physics is to analyze the immense data emerging from high energy hadron collisions, compare it with the established standard model processes and perform a statistical analysis in search for a peculiar "signal" which fills the shortcomings of the SM.

The subject of this thesis is to try to establish one of the popular extension of the standard model, the type–III seesaw mechanism. The search for the type–III seesaw mechanism is conducted using the proton-proton collision data collected at a center-of-mass energy of 13 TeV by the CMS detector at the CERN LHC during 2016. The search targets the event with three or more electrons or muons (termed as light leptons sometimes throughout the text) in the final state. Selection criteria based on the number of leptons and the invariant mass of oppositely charged lepton pairs are used to distinguish the signal from the standard model background. Also presented is a possible extension of this search if a hadronic tau lepton is included along with the light leptons. This is

the most sensitive probe to date of the type-III seesaw mechanism and shows around a factor of 500 improvement in sensitivity over previous searches.

This thesis is organized as follows. Chapter 2, provides a theoretical groundwork for the coming work, it also briefly reviews the various seesaw mechanisms in existence. Chapter 3 then starts with the essentials of the field, the experimental set-up, it introduces the LHC briefly and discusses the details of CMS detector. Chapter 4 gives the essentials of how the objects are reconstructed and identified at CMS detector, it also discusses the particular selections of the objects with their systematic uncertainties utilized in the search. Chapter 5 and 6 forms the main crux of the search where strategy and background estimates are discussed. Chapter 7 provides a brief overview of the statistical techniques employed along with the final results. Finally, chapter 8 discusses a possible extension to the existing search channels with the inclusion of hadronic taus.

Chapter 2

Theoretical Background

2.1 The Standard model of particle physics

The modern approach to fundamental particles is based upon the Standard Model theory (SM), developed in the 1970's with the works of Glashow, Weinberg, Salam, Higgs and others [14–21]. The SM is a quantum field theory that describes the three fundamental forces of nature (the electromagnetic, the weak and the strong) and their connection to the elementary particles. The SM has been extremely successful in describing the nature as we know it, verified by many experiments. The final piece of the theory, the Higgs Boson was discovered recently in the joint efforts at Large Hadron Collider in 2012, which makes the SM an important milestone of the elementary particle physics. However this grand theory has its own limitations and issues which we shall see in the course of this chapter.

The discussion about the SM mostly follows Ref. [22–24]. According to the SM, all the particle contents can be divided in three groups:leptons, quarks and mediators (bosons). The SM particle content and their properties are summarized in Fig. 2.1.

The SM is a gauge quantum field theory based on the symmetries of $SU(3)\times SU(2)\times U(1)$ unitary product group. The particle content of the SM, which pretty much describes all the elementary particles known, is chiefly divided into two categories:the fermions and the gauge bosons. The fermions are those that form the matter and the gauge bosons are force carriers that mediate the particle interactions. Fermions and bosons are further divided into sub-classes based on the particle characteristics.

Fermions are half-integer spin particles, obeying Fermi-Dirac statistics. They are further divided in leptons and quarks, based on the interactions in which they take part. The leptons do not take part in strong interactions, and interact only via electroweak

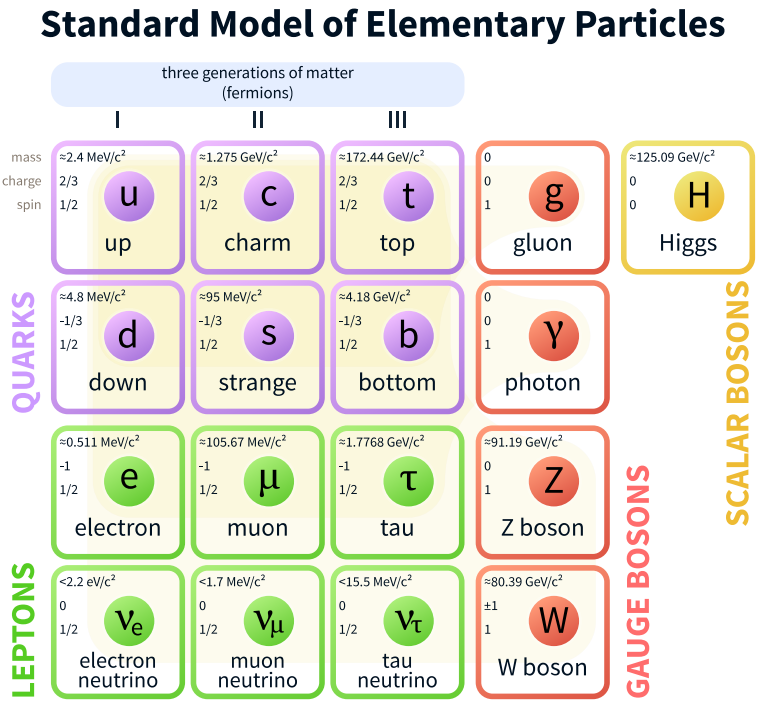

FIGURE 2.1: The SM particle content and their properties are listed here. The particles are grouped as lepton, quarks, gauge bosons and a scalar Higgs boson [1]

interactions. Leptons have three generations, each generation forms an isospin doublet of left-handed states $\begin{pmatrix} \nu_\ell \\ \ell \end{pmatrix}_L$, where ℓ represents an e, μ, τ, with a non-zero weak isospin along with a singlet of right-handed state ℓ_R with zero weak isospin. Out of this doublet pair, one particle(e, μ, or, τ) carries an integer charge of -1, whereas the other (neutrinos ν_e, ν_μ, ν_τ) is electrically neutral. Quarks interact via strong and electroweak interactions. Quarks have fractional charges of $-\frac{1}{3}$or $+\frac{2}{3}$. The quarks come in 3 "colors" $c = r, b, g$ and 6 "flavors"(up, down, charm, strange, bottom, and top). The left-handed quarks form isospin doublets $\begin{pmatrix} U \\ D \end{pmatrix}_L$, whereas the right-handed quarks form $SU(2)$ singlets. This difference between the left-handed and right-handed quarks explains why the weak interactions disrespect parity symmetry. The particles of each generation differ by their masses, particles in earlier generation are lighter than corresponding particles of later generations. The electron, the up and down quarks make up all the stable matter in the universe.

The gauge bosons or simply "bosons" with integer spin of 1, are the force carriers that mediate the strong, weak and electromagnetic interactions. Photons mediate the electromagnetic interaction and are mass-less. The W^+, W^- and Z bosons mediate the weak interaction, and are massive. The $W^\pm$ carries an electric charge of +1 and -1 and couples to the electromagnetic interaction. These three bosons along with the photon

are electroweak mediators. There are eight type of gluons (based on color charge) which mediates strong interaction. Finally, there is a boson, termed as the Higgs boson with spin-0 which is responsible for electroweak symmetry breaking. The Higgs boson, which is a massive particle, provides answer to the question that why the elementary particles except gluon and photon have mass.

Like any other quantum field theory, the SM is expressed in terms of a *Lagrangian* from which the evolution and interactions of the fields can be inferred. The standard model Lagrangian is built upon the principle of local gauge invariance and described by $SU(3) \times SU(2) \times U(1)$ group. The $SU(3)$ part represents quantum chromodynamics, the theory of strong interactions. The $SU(2) \times U(1)$ subgroup describes the electroweak sector of the standard model [25].

The SM theory is constructed under the local gauge invariance expectation, which means the theory remains symmetric under the following transformation,

$$\psi(x) \rightarrow e^{i\alpha(x)}\psi(x) \tag{2.1}$$

for the $U(1)$ abelian group, which represents electromagnetic interactions. Here $\alpha(x)$ represents the localized phase transformation parameter for a complex function $\psi(x)$ of the space-time coordinates. The local gauge invariance of the Lagrangian requires the introduction of the covariant derivatives, which is defined as,

$$D_\mu \equiv \partial_\mu - ieA_\mu \tag{2.2}$$

where A_μ is a vector field which transforms as,

$$A_\mu \rightarrow A_\mu + \frac{1}{e}\partial_\mu \alpha \tag{2.3}$$

The above described invariance is possible if only the new field A_μ is massless and the Lagrangian has no terms such as $\frac{1}{2}m^2 A_\mu A^\mu$. This field A_μ represents the physical photon field. On similar terms, the non-abelian $SU(3)$ group which forms a quantum chromodynamics, is predicted to have a massless quanta, gluon.

In the electroweak sector, photons are massless but the bosons governing weak interactions, $W^\pm$, Z are massive. Some mechanism has to be introduced for spontaneous symmetry breaking owing to these facts, otherwise just introducing mass terms such as $M^2 W_\mu W^\mu$, renders the theory non invariant under gauge transformations. The spontaneous symmetry breaking is achieved through the action of a new scalar field, whose

corresponding particles are the Higgs bosons. The local gauge symmetry of the $SU(2)$ is spontaneously broken through Higgs mechanism, allowing local gauge invariance to be maintained , while still generating masses for the W, Z bosons. In this mechanism, the resulting massless scalars which occur according to the Goldstone theorem, known as Nambu-Goldstone bosons, gets incorporated in gauge bosons, giving them mass. Consider a potential of the form,

$$V(\phi) = \mu^2\phi^\dagger\phi + \lambda(\phi^\dagger\phi)^2 \tag{2.4}$$

by choosing $\mu^2 < 0$ and $\lambda > 0$, two minima of the potential can be obtained at, $\pm\sqrt{\frac{-\mu^2}{2\lambda}} \equiv \nu/\sqrt{2}$. This potential represented by Eq. 2.4 can be considered as Higgs field. The minimization of this potential is chosen such that it spontaneously breaks the $SU(2) \otimes SU(1)$ symmetry , giving three massive states ($W^\pm$, Z) and a massless state (the photon). The Higgs boson the quanta of the Higgs field is a boson with spin zero, no electric charge and no colour charge. The SM does not predict the mass of the Higgs boson. The LHC in July 2012 announced the discovery of the Higgs boson, with two of its experiments measuring the mass of the previously unknown boson: CMS measured the mass at 125.3 ± 0.6 GeV [26] whereas ATLAS measured it at 126.0 ± 0.6 GeV [27], the studies so far has shown that this unknown boson is consistent with the SM Higgs boson [28]

The whole of SM can be written in a compact Lagrangian form. This Lagrangian, known as the SM Lagrangian can be described as follows,

$$\begin{aligned}\mathcal{L} = &\text{ (boson kinetic energies and self-interactions)}\\ &+ \text{ (fermion kinetic energies and their interactions with the bosons)}\\ &+ \text{ (mass terms for the bosons, Higgs and their couplings)}\\ &+ \text{ (fermion mass terms and their coupling to the Higgs)}\end{aligned}$$

where the fermion mass terms originate from interactions with the Higgs fields from the Yukawa couplings. An easy to follow reference for the terms in this Lagrangian can be found here [29].

2.2 A look beyond standard model

Although extremely successful, the standard model of particle physics is not the last word on the subject. This is because there are unresolved phenomena and some conceptual questions are still posed before this theory [30–32]. There are various proposals such as

Supersymmetry [33], various extensions beyond the existing framework which tries to resolve these questions, collectively referred to as beyond standard model (BSM) or new physics. The existence of BSM physics is strongly motivated through direct experimental evidences such as the existence of neutrino masses, the existence of dark matter and dark energy, or the matter-antimatter asymmetry, as well as through conceptual problems in the SM, such as the large number of free parameters, the "hierarchy problem" or the coupling unification. I will briefly describe these issues with the standard model. One of the issue (neutrino masses) provides a motivation for this thesis work, which I will discuss in bit more detail in subsequent section.

Conceptual issues with the standard model

- The standard model as of now, does not include an explanation for gravity, which is one of the fundamental forces of the nature.
- Free parameters in the SM which are as many as nineteen, especially in scalar sector might be hinting toward a more general and elegant theory than the SM.
- Another conceptual issue arises due to so-called gauge hierarchy problem [34]. The issue is connected to the huge energy difference between the Plank scale and the electroweak scale. The SM particle masses are set by the vacuum expectation value of the neutral Higgs fields. This value is around 246 GeV. Radiative corrections to the scalar boson squared mass are quadratically proportional to the ultraviolet momentum cutoff, which is at least equal to the energy to which the SM is valid without any addition of new physics. These radiative corrections are derived from higgs couplings to fermions and gauge bosons, and from its self-couplings. If one considers that the SM is valid up to the Planck mass, the quantum correction to m_H^2 is about thirty orders of magnitude larger than m_H^2, which needs some incredible fine tuning of the Higgs mass. Even if the renormalization process absorbs these corrections, some may find uncomfortable with this sensitivity to the details of high scales.
- The large mass differences between fermions, related to Yukawa couplings that can differ by up to six orders of magnitude in the case of the electron and the top quark. This is termed as the fermion mass hierarchy problem.

Dark matter and dark energy

Astronomical evidences such as galaxy rotation curve, accelerating universe and other observations shows that SM represents only about 5% of the mass/energy content of the universe. The rest is Dark Matter (about 20%) and Dark Energy (about 75%) [35].

The plot of tangential velocity as a function of distance from the galactic centre, referred to as "rotation curves" of galaxies, measured for numerous galaxies, shows clear discrepancy. The rotation curves measured for various galaxies instead of showing $1/\sqrt{r}$ dependency, shows an increasing trend. This evidence hints at the unaccounted matter referred to as a dark matter permeates a halo well outside the galactic centre. The SM provide no explanation for this evidence [36].

The story does not end at matter and dark matter, with the discovery of accelerated expansion of universe it was necessary to have a cosmological constant in the form of "dark energy" associated with the vacuum expectation value of some quantum field. Dark energy in effect is a constant term in the stress tensor, spreading all space uniformly. The nature of this field is still a mystery and SM has no say in this [36]

Matter/Antimatter asymmetry

Our surrounding world is all made up of matter, with no traces of an antimatter. It is widely believed that after the big bang the matter and antimatter were created in equal amounts. It is natural to ask then "what mechanism has disfavoured the matter over antimatter? or where has all the antimatter gone?". The probability that our matter-dominated corner of the universe is balanced by another corner of the universe dominated by antimatter is very negligible. Even if this would have been the case, this would have been seen as perturbations in the CMB [37]. Sakharov, in 1967, laid down mechanisms necessary to obtain a global matter/antimatter asymmetry [38],

- Interactions in the universe out of thermal equilibrium at a given moment of the universe history;
- Baryon and lepton number violation;
- C- and CP-violation (the rate of a process $i \to f$ can be different from the CP-conjugate process $\tilde{i} \to \tilde{f}$).

In the SM, CP-violations occurs in the weak interactions of quarks, and is sourced to the residual phase in the CKM matrix. These sources are nowhere near enough to account for the matter prevalence of the known universe.

2.3 Neutrinos and the seesaw mechanism

Experiments like SuperKamiokande and others has consistently shown that the neutrino has a mass hierarchy by the virtue of their oscillations [39–41]. This is in contradiction with the SM which in its minimalist form considers neutrinos mass-less. This is a consequence of the SM containing only left-handed neutrinos. With no suitable right-handed partner, it is not feasible to add a renormalizable mass term to the standard model Lagrangian. Measurements have indicated that neutrinos spontaneously change flavour. Such oscillations are possible only if neutrinos have masses. Flavor eigenstates $(\nu_e, \nu_\mu, \nu_\tau)$ are then linear combinations of the fields of at least three mass eigenstate neutrinos ν_1,ν_2,ν_3. Neutrino masses are not known yet, only upper bounds on the neutrino masses have been obtained as of now ($m_\nu < 2$ eV) [42, 43]. The oscillation measurements have made it possible to measure the differences between the neutrino squared masses: $\Delta m^2_{12} = (7.53 \pm 0.18) \times 10^{-5} eV^2$ and $\Delta m^2_{32} = (2.44 \pm 0.06) \times 10^{-3} eV^2$ [1]. Direct measurement of neutrino masses and their other properties is an active area of search, many experiments are planned in this direction to solve this one of the main puzzles of modern particle physics [44–47]. LHC might also provide a hint in this direction, there are many active dedicated searches going on in LHC phase-space to understand the nature of neutrinos [48–50]. The analysis described in this thesis has been published in Ref. [51].

The upper limit of 2 eV on neutrino masses makes them at least five orders of magnitude lighter than the other particles in the standard model which in turns necessitates the extension of the SM that could explain how neutrinos get their mass, but also why the mass is so small. There can be many approaches to have the SM extension. One of the simplest approach, the so-called seesaw mechanism, is to add right-handed neutrinos and have these couple to left-handed neutrinos with a Dirac mass term.

There are three and only three different realizations of the seesaw mechanism, I will briefly discuss them. In the course of discussion it will also become clear that why these are termed as "seesaw" mechanisms. The main idea is still a renormalizable completion of the SM that can lead to small neutrino masses. The discussion closely follows the reference [2].

Type–I seesaw

The more intuitive extension of the SM is the introduction of ν_R (per family of fermions), a gauge singlet chiral fermion. This ν_R is a right handed neutrino, which fits naturally due to the inherent structural quark – lepton symmetry.

In the SM, if a right handed neutrino is added, the leptonic sector is given by,

$$\begin{pmatrix} \nu \\ e \end{pmatrix}_L, e_R, \nu_R \tag{2.5}$$

The corresponding Yukawa couplings [52] are,

$$\Delta\mathcal{L}_Y = y_D(\overline{\nu e})_L i\sigma_2\Phi^*\nu_R + \frac{M_R}{2}\nu_R^T C\nu_{\mathrm{R}} + h.c. \tag{2.6}$$

where we include the Majorana mass term M_R for the right-handed neutrino since it is a SM singlet.

Let us introduce Majorana spinors,

$$\nu_M \equiv \nu_L + C\overline{\nu}_L^T, N_M \equiv \nu_R + C\overline{\nu}_R^T \tag{2.7}$$

using,

$$\overline{\nu}_M N_M \equiv \overline{N}_M \nu_M \tag{2.8}$$

we get,

$$\Delta\mathcal{L}_Y = \frac{1}{2}(i\overline{\nu}_M\gamma^\mu\partial_\mu\nu_M + i\overline{N}_M) + \frac{1}{2}m_D(\overline{\nu}_M N_M + \overline{N}_M\nu_M) + \frac{M_R}{2}\overline{N}_M N_M \tag{2.9}$$

where $m_D \equiv y_D\upsilon$ and $\upsilon = \langle\phi^0\rangle$ is the vacuum expectation value of the neutral component of Φ.

We arrive at the mass matrix for ν and N,

$$\begin{pmatrix} 0 & m_D \\ m_D^T & M_R \end{pmatrix} \tag{2.10}$$

M_R and m_D represents Majorana and Dirac mass terms. We will consider three scenarios, in first case if $M_R \ll m_D$ neutrinos would be majorly Dirac particles. The second case for $M_R \simeq m_D$, would lead to a complex combination of Dirac and Majorana neutrinos, whereas the third case, for $m_D \ll M_R$ we will have a predominantly Majorana neutrinos. The third case represents the so-called seesaw mechanism, the approximate eigen values in this case N with mass $M_N \equiv M_R$ and ν with a very tiny mass,

$$M_\nu = -m_D^T\frac{1}{M_N}m_D \tag{2.11}$$

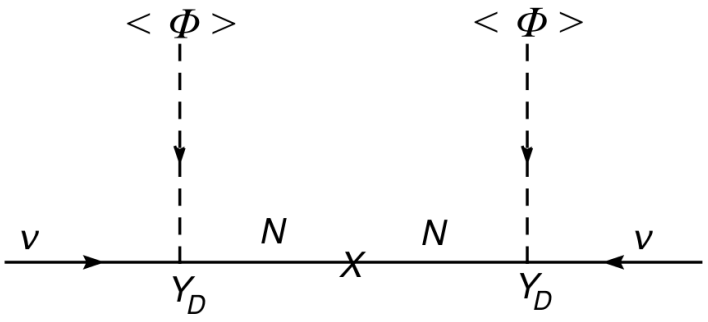

FIGURE 2.2: Diagram representing the seesaw mechanism, here heavy propagator N brings tiny mass to the neutrino [2].

Equation 2.11 represents type–I seesaw mechanism in all its essentiality. It also tells us that with heavy ν_R, neutrino gets a Majorana mass, justifying the term "seesaw" hailed in the name of this mechanism.

From the mass matrix represented in equation 2.10, it is clear that the number of ν_R's dictates the number of massive light neutrinos. In other words for each ν_R only one ν_L gets the mass which in turn,tells us that at least two ν_R are required to account for both solar and atmospheric neutrino mass differences.

In Fig. 2.2, we have the diagrammatic representation of seesaw mechanism, it's clear from the diagram that the heavy neutrino propagator brings in the seesaw mechanism.

Type–II seesaw

In the place of ν_R, a $Y = 2$ triplet $\Delta \equiv \vec{\Delta} \cdot \vec{\sigma}$ could be brought in to play the same role. This introduction of $Y = 2$, $SU(2)_L$ forms the heart of the type–II seesaw mechanism. The new Yukawa couplings like Eqn. 2.9 would then be,

$$\Delta\mathcal{L}(\Delta) = y_\Delta^{ij} \ell_i^T C \sigma_2 \Delta_L \ell_j + h.c. \tag{2.12}$$

where $i, j = 1, ...N$ counts generations. Neutrinos have a mass when Δ_L gets vacuum expectation value,

$$M_\nu = y_\Delta \langle \Delta \rangle \tag{2.13}$$

The vacuum expectation value emerges from the cubic scalar interaction,

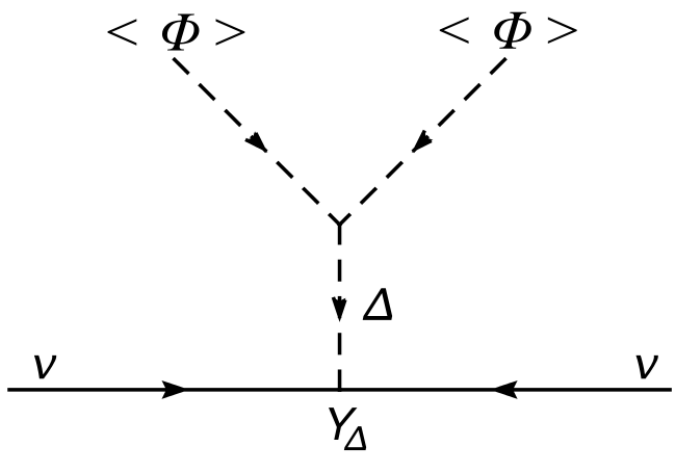

FIGURE 2.3: Diagram representing the type–II seesaw mechanism [2].

$$\Delta V = \mu \Phi^T \sigma_2 \Delta_L^* \Phi + M_\Delta^2 Tr \Delta_L^\dagger \Delta_L + ... \tag{2.14}$$

leading to,

$$\langle \Delta \rangle \simeq \frac{\mu v^2}{M^2} \tag{2.15}$$

where μ is expected to be of order M_Δ. If $M_\Delta \gg v$, neutrinos will be naturally light. It is essential to note that 2.13 and 2.15 gives neutrino a Majorana mass.

The diagrammatic representation of type–II seesaw mechanism is shown in figure 2.3.

Type–III seesaw

The Yukawa interaction described in Eqn. 2.9 for a new singlet fermions applies directly to $SU(2)$ new fermionic triplets also. One can write the Yukawa interaction using Majorana notation where for simplicity the generation index is suppressed and also an index counting the number of triplet. As discussed, at least two triplets are needed in order to provide two massive light neutrinos.

$$\Delta \mathcal{L}(T_F) = y_T \ell^T C \sigma_2 \vec{\sigma}.\vec{T}_F \Phi + M_T \vec{T}_F^T C \vec{T}_F \tag{2.16}$$

Following the same procedure as that of type–I, one gets a type–III mass relation in the case of, $M_T >> v$ as

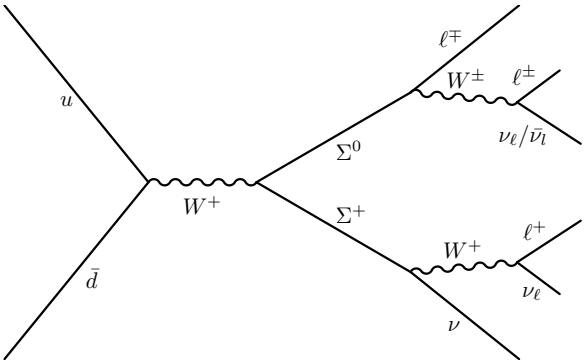

FIGURE 2.4: Feynman diagram example of the fermion production and decay in the type-III seesaw model.

$$M_\nu = -y_T^T \frac{1}{M_T} y_T v^2 \tag{2.17}$$

As in case of type–I, two such triplets(or a triplet and a singlet) are needed to make the case for solar and atmospheric neutrino oscillations. Also as before, Eqn. 2.17 gives neutrino a Majorana mass for large M_T.

If the SM extension we are talking about is assumed to be restricted to single type of new particles added, type–I, type–II and type–III seesaw mechanisms exhaust all the cases of giving Majorana mass to the neutrinos within $SU(2) \times SU(1)$ symmetry principle.

The type-I, II, III seesaw mechanisms are also chronological and in order of their popularity. It is important to note that a new theory beyond standard model may turn out much more complex, than the addition of single type of particles and having simple extension in one of three forms of seesaw mechanism. However, these mechanisms provides us with definitive experimental final state signatures at the LHC. The successful search of these mechanism will provide a direction for the physics beyond SM.

The topic of this thesis is to search for type–III seesaw model, which adds a fermionic triplet as an extension to the existing SM. As discussed earlier within the type-III seesaw model, the neutrino is considered a Majorana particle whose mass arises from the mediation of new massive fermions that form an SU(2) triplet of heavy Dirac charged leptons $\Sigma^{\pm}$ and a heavy Majorana neutral lepton Σ^0. In pp collisions, these massive fermions may be pair-produced through leading order electroweak interactions.

Final states arise with three or more charged leptons arise from the following decays from pair produced Σ's,

- $\Sigma^{\pm} \rightarrow \mathrm{W}^{\pm}\nu_\ell$
- $\Sigma^0 \rightarrow \mathrm{W}^{\pm}\ell^{\mp}$

- $\Sigma^{\pm} \to Z\ell^{\pm}$
- $\Sigma^{0} \to Z\nu_{\ell}$
- $\Sigma^{\pm} \to H\ell^{\pm}$
- $\Sigma^{0} \to H\nu_{\ell}$;

Where ℓ represents e, μ or τ, an example Feynman diagram for a complete decay chain is shown in Fig. 2.4 The renewed interest in the type-III seesaw models emphasizes the importance of exploring such signatures at the CERN LHC [53–58].

Chapter 3

Experimental Set-up

3.1 The Large Hadron Collider

The Large Hadron Collider(LHC) [59, 60] is a superconducting hadron accelerator and collider. It is located along the Swiss-French border at the European Organization for Nuclear Research (CERN). As the name suggests, the LHC was designed to accelerate and collide protons(as well as heavy ions) at centre-of-mass energy of $\sqrt{s} = 14\,\text{TeV}$ at it's peak capacity. The aim of the experiment is exploring, the nature of electroweak symmetry breaking and the beyond standard model (BSM) physics.

With the circumference of about 27 km and at a depth of about 100m, the LHC houses five main detectors/experiment across the ring. Out of the five, the Compact Muon Solenoid(CMS) and ATLAS detectors are general purpose detectors. The remaining three, LHCb (to explore B-physics), ALICE (for heavy ion collision studies), and TOTEM (to measure the total proton-proton cross section to high precision), are specialized detectors [3].

The Fig. 3.1 shows the structure of LHC complex along with the positions of various detectors and acceleration mechanics. Protons produced from hydrogen gas and injected from a Duoplasmatron source [61] are accelerated through a chain of linear and circular accelerators. Before injecting into LHC ring, protons are accelerated through the Linear Accelerator2 (Linac2), Proton Synchrotron Booster(PSB), Proton Synchrotron (PS), and Super Proton Synchrotron (SPS), to energies of 50 MeV, 1.4 GeV, 25 GeV and 450 GeV, respectively. Protons of 450 GeV are injected into main LHC ring, where they are further boosted and finally brought into collision at the four previously defined interaction points, where detectors are situated. At LHC lead ions are also accelerated and collided with a dedicated detector ALICE, utilized to study ion collision.

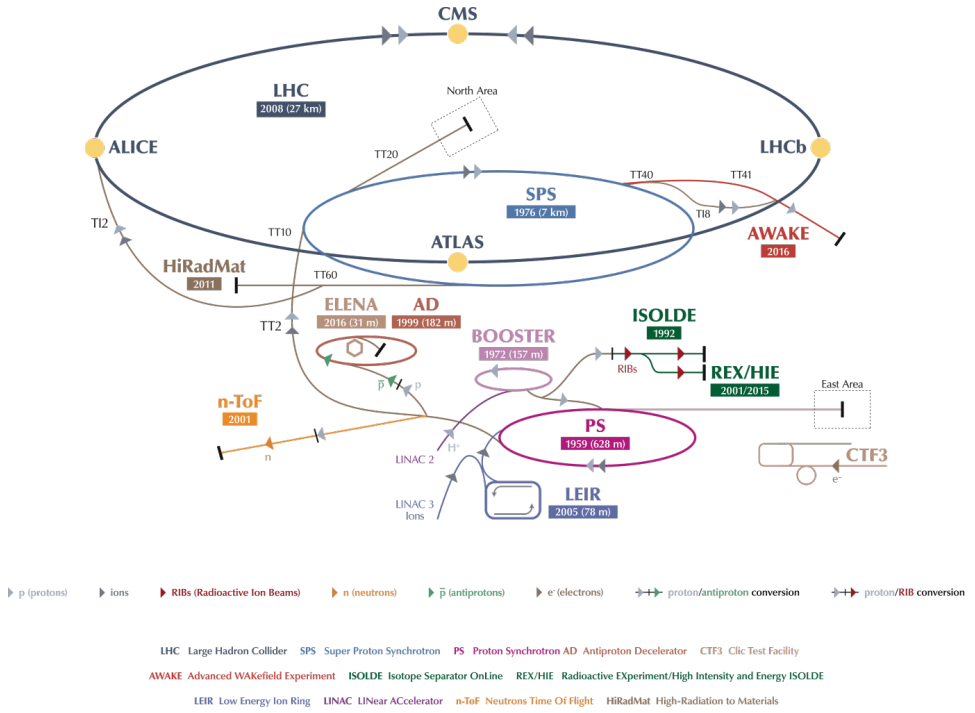

FIGURE 3.1: The schematic view of CERN-LHC accelerator complex) [3]

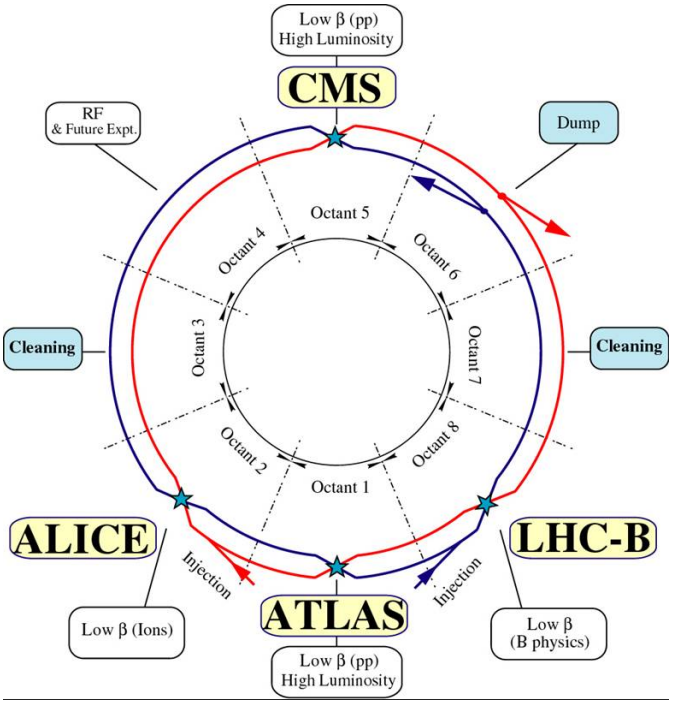

FIGURE 3.2: The schematic view of the collider ring [3]

The LHC ring is composed of eight arcs and eight straight sections labeled as eight octants as shown in Fig. 3.2. Twin bore superconducting dipole magnets (NbTi) situated along the arcs, provide magnetic field up to 8.3 Tesla and are used to bend the proton beam. The magnets are operated at the temperature of 1.9 Kelvin by using liquid helium for cooling. Radio frequency cavities operated at 400.8 MHz are used for capturing, focusing and further accelerating and storing the injected proton beams. The proton beams circulating in both directions in separate rings are brought together for collisions at various detector points. Quadrupole magnets are further used to focus the beams at the collision point. The LHC beam pipes are maintained at 10^{-11} mbar around the room temperature sections near the detectors in order to achieve the target beam lifetime of around 100 hours. Kicker magnets are provided to dump the beam.

The instantaneous luminosity($\mathcal{L}$) which is an important parameter for a collision of proton beams, is related to the production rate($\frac{dN_p}{dt}$) and cross-section(σ_p) of any given process as,

$$\frac{dN_p}{dt} = \sigma_p \mathcal{L} \tag{3.1}$$

Assuming round, Gaussian bunches in the beam, the instantaneous collider luminosity can be expressed as,

$$\mathcal{L} = \frac{N_b^2 n_b^2 f_{rev} \gamma}{4\pi \sigma_x^* \sigma_y^*} F = \frac{N_b^2 n_b^2 f_{rev} \gamma}{4\pi \epsilon_n \beta^*} F, \tag{3.2}$$

where N_b is the number of particles per bunch crossing, n_b is the number of bunches per beam, and f_{rev} is the revolution frequency and σ_{xy}^* denotes the transversal beam sizes in x and y directions. The emittance ϵ_n corresponds to the average normalized phase space occupied by the beam and describes the spread in the momentum and positions of the protons. The measure of the transverse beam width at the collision point, is referred to as β^*. The cross-sectional area expressed as $A = \frac{4\pi\epsilon_n\beta^*}{F\gamma}$, where F is the geometric factor describing the crossing angle at the interaction point, and γ is the Lorentz factor. The superscript asterisk denotes values taken at the CMS interaction point [60].

At ultra-relativistic speeds, particles take about 89 μs to circulate the LHC, and the ring can nominally accommodate 2808 proton bunches with a spacing of 25 ns. During the 8 TeV run, termed as Run-I of the LHC, a total of 23.3 fb^{-1} pp collision data was delivered, out of which 21.8 fb^{-1} data was collected by CMS. After technical shut down of two years, the LHC resumed its operation in 2015, and started delivering the data, known as run-II campaign. The result presented in this thesis is based on the data collected by CMS experiment in 2016, during run-II. During Run-II of the LHC the

TABLE 3.1: Comparison of proton running conditions in the LHC during operation till June 2016, in Run-I(2010-12) and Run-II(2015-16), shown together with initially designed parameters [13]. Here unit σ represents the width of the Gaussian assuming the beam to have a Gaussian shape in the transverse direction.

Parameters	Design	2010	2011	2012	2015	June 2016
Beam Energy (TeV)	7.0	3.5	3.5	4.0	6.5	6.5
Protons/bunch (average at start of collisions)(10^{11} p)	1.15	1.0	1.3	1.5	1.1	1.1
Maximum number of bunches	2808	368	1380	1380	2244	2076
Maximum stored energy per beam (MJ)	362	23	112	143	277	266
Bunch Spacing (ns)	25	150	50	50	25	25
Transverse normalized emittance ϵ_n, typical value in collision (μm)	3.75	2.6	2.4	2.4	3.5	3.4
Half crossing angle (μrad)	143	100	120	146	145	185
Primary collimator cut (σ)	6.0	5.7	5.7	4.3	5.5	5.5
Secondary collimator cut (σ)	7.0	8.5	8.5	6.3	8.0	7.5
Tertiary collimator cut (σ)	8.3	15.0	11.8	9.0	13.7	9.0
Smallest allowed magnet aperture (σ)	8.4	17.5	14.1	10.5	15.5	9.9
β^*(m)	0.55	2.0-3.5	1.0-1.5	0.6	0.8	0.4
Maximum peak luminosity ($10^{34} cm^{-2} s^{-1}$)	1.0	0.021	0.35	0.77	0.51	1.01
Total integrated luminosity (fb^{-1})		0.048	5.5	22.8	4.2	8.1

center-of-mass energy is increased at 13 TeV, yielding a peak instantaneous luminosity $1.5 \times 10^{34} cm^{-2} s^{-1}$ in 2016.

In 2016 the LHC operated with 2076 bunches spaced at 25 ns and each bunch contained up to 1.1×10^{11} protons at an energy of 6.5 TeV [13]. The optimized parameters for 2016 run, along with the comparison with other data taking periods is presented in Table 3.1. During 2016, the LHC has delivered an integrated luminosity of 40.82 fb^{-1} to the ATLAS and CMS experiments, of which 37.76 fb^{-1} have been recorded by the CMS detector and 35.9 fb^{-1} have been certified for physics analyses [4, 62]. The data collection efficiency of the detector depends upon number of calibration constants such as calibration time, the number of pile-up interactions per bunch crossing and the filling scheme of the LHC or number of active bunches. A detailed discussion about luminosity measurement and its systematic effect is given in the reference [63]. Under the 13 TeV operation conditions, the average number of additional primary vertices in the collision of the two beams in the same proton bunch crossing (pileup) was observed to be around 30, with tails extending as high as 60 [4]. The time-evolution of the total integrated delivered and recorded luminosities as well as the distribution of pileup interactions during the 13 TeV, 2016 run are illustrated in Fig. 3.3. A pile-up distribution made with 15.9 fb^{-1} of data when the analysis was maturing with all the constituent of backgrounds is shown in Fig. 3.4. The pile-up distribution, as seen, has to be corrected using a pile-up re-weighting procedure [64, 65].

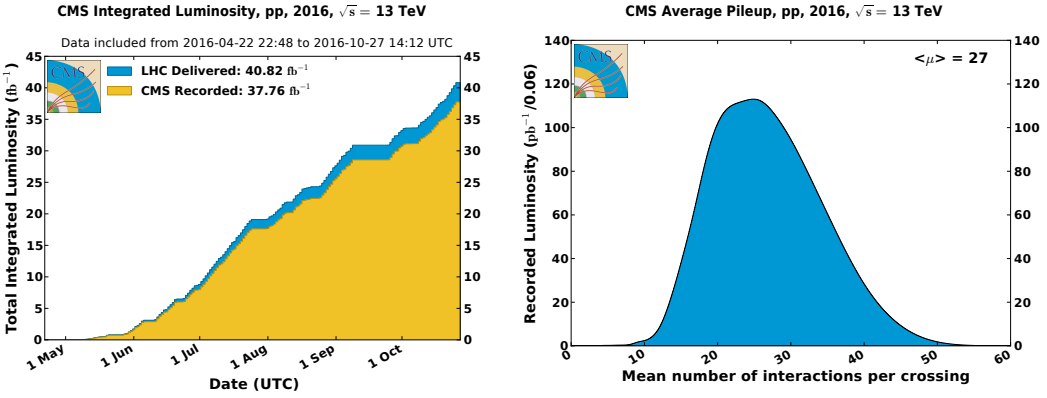

FIGURE 3.3: Integrated luminosity versus time delivered to (blue), and recorded by the CMS detector (yellow), evolution (left), and the distribution of mean number of interactions per bunch crossing (right) during stable beams and for pp collisions at 13 TeV in 2016 [4]

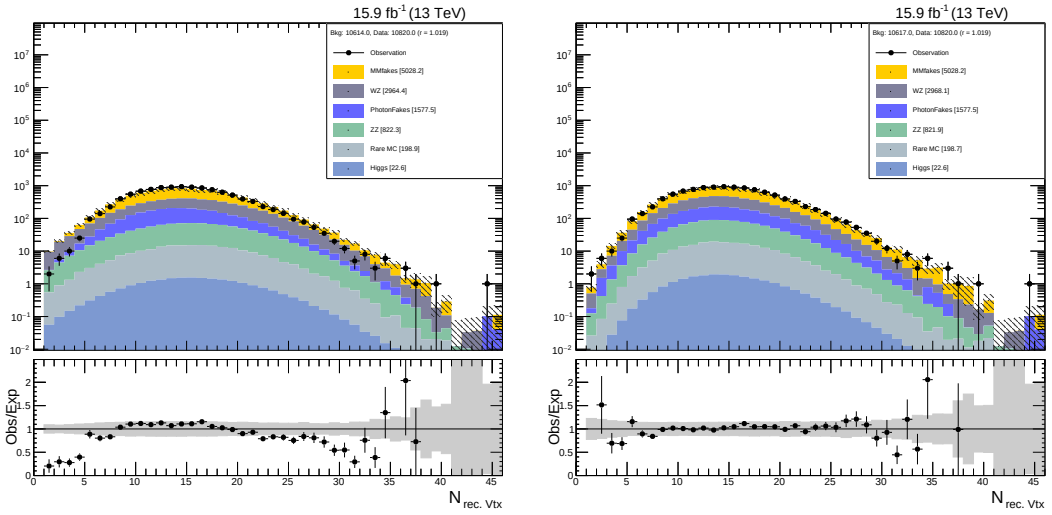

FIGURE 3.4: Pileup distribution(Left) with its re-weighted version(Right) with $15.9\,\mathrm{fb}^{-1}$ of data.

3.2 The CMS Detector

The CMS experiment [5] is a multi-purpose apparatus, designed to cover a wide range of physics goals, from the discovery of Higgs boson to the ongoing search for BSM physics. Its main specifications to meet these goals are excellent muon identification and momentum resolution, good charged-particle momentum resolution by virtue of its inner tracker. A good electromagnetic energy resolution, missing-transverse-energy and dijet-mass resolution is also achieved in line to cover physics objectives. The main distinguishing features of CMS are a high-field solenoid(designed to precisely measure muons), a full-silicon-based inner tracking system, and a electromagnetic calorimeter, made of scintillating crystals.

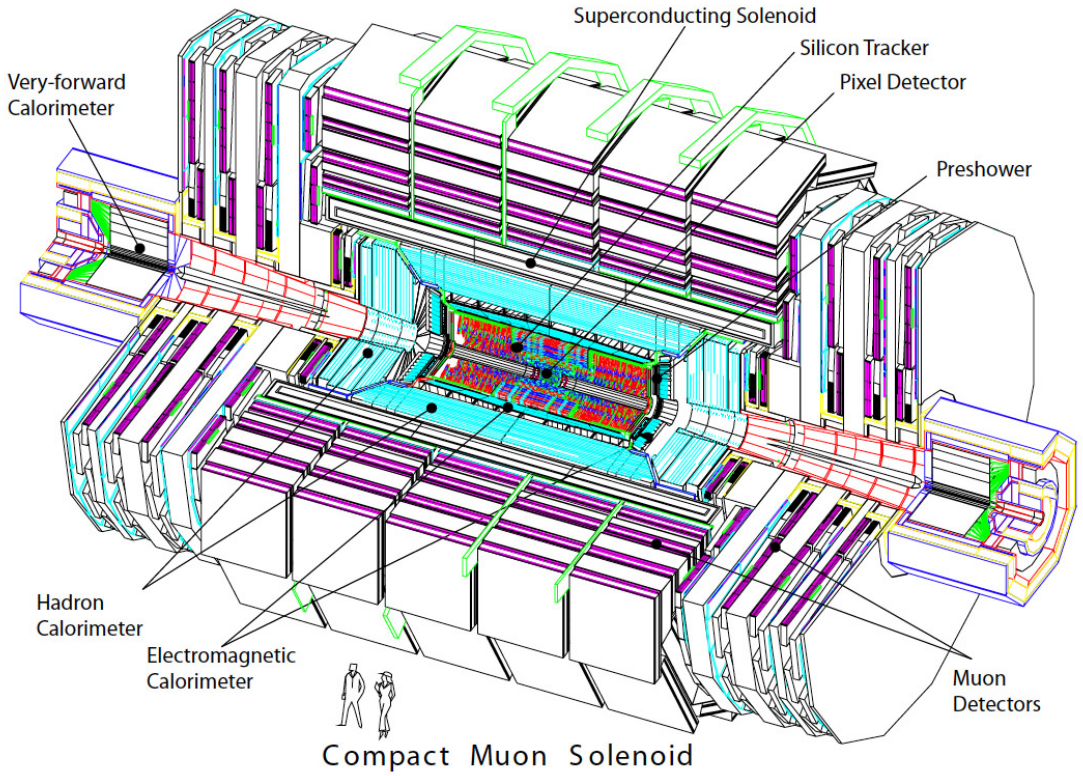

FIGURE 3.5: Schematic view of the CMS detector [5]

Weighing around 14000 tons, measuring 28 m in length and 15 m in diameter the CMS is a modern detector, and still compact by the standards. The main feature, a 13-m long, 6-m-inner-diameter, 3.8-T superconducting solenoid providing a large bending power (12Tm) before the muon system. The inner tracker and calorimetry are housed within the bore of the solenoid magnetic coil. The inner tracker consists of silicon strip and pixel detectors. On the calorimetry side, CMS consists of a lead tungstate crystal electromagnetic calorimeter, and a brass-scintillator hadron calorimeter. A schematic view of the CMS detector is shown in Fig. 3.5.

The CMS detector is described using a right-handed co-ordinate system, with the origin at the nominal collision point. The x-axis points radially towards the center of the LHC and the y-axis points vertically. The z-axis is orthogonal to the other axes and is directed along beam direction. The azimuthal angle ϕ is measured in the plane defined by the x- and y-axes, from the x-axis. The polar angle θ is measured from the z-axis, in a plane orthogonal to the xy-plane and containing the z-axis, and is used to define the pseudorapidity (η), which is used for the measurements:

$$\eta = -\ln[\tan(\theta/2)]. \tag{3.3}$$

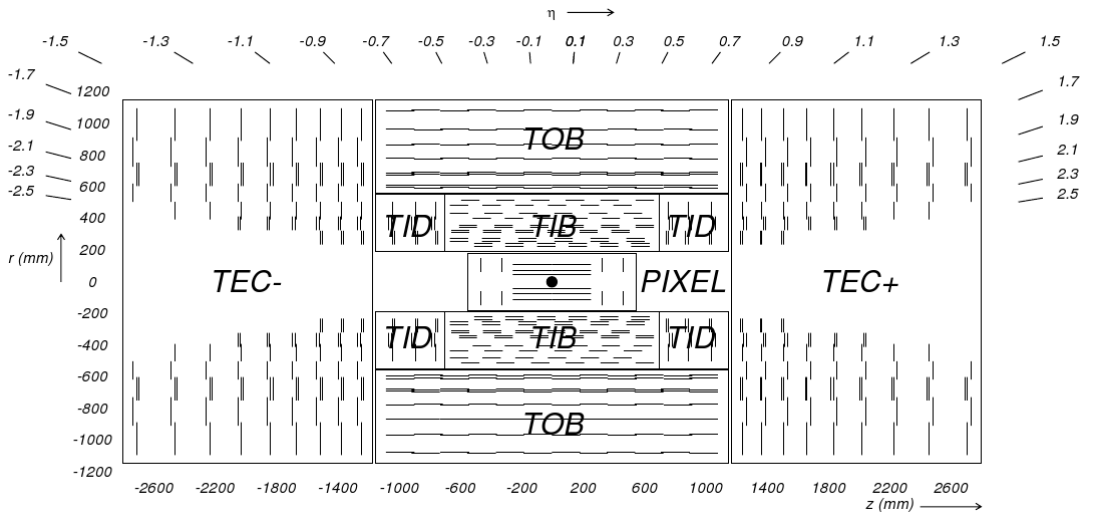

FIGURE 3.6: Sectional view of the inner tracking system of the CMS detector [5]

The pseudorapidity is a good approximation for particles with $E >> m$ of the rapidity y,

$$y = \frac{1}{2}\ln(\frac{E + p_z}{E - p_Z}) \tag{3.4}$$

I will now describe the components of CMS detector in detail.

3.2.1 Tracker

Closest to the beam pipe, inner tracking system [66, 67] of CMS provides a precise and efficient measurement of the trajectories of charged particles as well as a precise reconstruction of vertices. The inner tracker entirely made of silicon, surrounds the interaction point and has a length of 5.8 m and a diameter of 2.5 m. Because of the high number of particles produced in overlapping pp collisions, it is of primary importance that the tracker has a high granularity. While the quantity of the material had to be kept low to limit photon conversion, multiple scattering, bremsstrahlung and nuclear interactions, the tracker had to have a capability to support a larger power density and to be radiation resistant.

The CMS tracker is composed of a pixel detector with three barrel layers at radii between 4.4 cm and 10.2 cm and a silicon strip tracker with 10 barrel detection layers extending outwards to a radius of 1.1 m. Each system is completed by endcaps which consist of 2 disks in the pixel detector and 12 disks in the strip tracker on each side of the barrel, extending the acceptance of the tracker up to a pseudorapidity of $|\eta| < 2.5$. A sectional representation of a tracking system is illustrated in Fig. 3.6. The Tracker Inner Barrel

and Disks (TIB/TID) are composed of 4 barrel layers supplemented by three disks at each end. The TIB/TID is surrounded by the Tracker Outer Barrel (TOB), consisting of six layers. Additionally two endcaps, each composed of 9 disks, in either Z direction, TEC± provides further eta coverage. In total, the inner tracker consists of 1440 silicon pixel and 15148 strip detector modules. The resolution on the transverse momentum for a 100 GeV charged particle is about 2.0%. The impact parameter resolution achieved by the inner tracker is about 15μm.

3.2.2 Electromagnetic Calorimeter

The electromagnetic calorimeter of CMS (ECAL) [68] is a hermetic homogeneous calorimeter made of 75848 lead tungstate ($PbWO_4$) crystals, in a cylindrical shape, consisting of a barrel and two endcaps with an additional preshower detector in front of the each end cap. The main objective of the ECAL is accurate detection of electrons and photons and provide a good energy resolution for these particles. The ECAL of CMS detector covers the pseudorapidity range of $|\eta| < 3.0$. Electromagnetic showers produced by electrons or photons entering crystals, ionize the crystal atoms, which emit a scintillation light on de-excitation, collected by photo-detectors to generate an electronic signal. In case of the lead tungstate ($PbWO_4$), a blue-green scintillation light with a broad $420 - 30$ nm wavelength is produced upon particle interaction, which is then detected by silicon avalanche photo-diodes (APDs) in the barrel region ($|\eta| < 1.479$) and vacuum photo-diodes (VPTs) [69] in the endcap region ($1.479 < |\eta| < 3.0$).A preshower detector which is a sampling calorimeter consisting of two layers of silicon sensors and lead of total $3X_0$(X_0 denotes one radiation length = 0.85 cm) is located in front of the ECAL endcaps. A transverse view of ECAL is represented in Fig. 3.7 elaborating its geometry.

The use of the lead tungstate ($PbWO_4$) crystals with short radiation length (0.89 cm), a Moliére radius of 2.2 cm, and a high density($8.28 g/cm^3$) provides a fine granularity and a compactness of the ECAL. Crystal front-end faces and length measure 2.2×2.2 cm^2 by 23 cm and 2.86×2.86 cm^2 by 22 cm, and are equipped by APDs in the barrel and VPTs in end cap regions. About 80% of the light is emitted in 25 ns by these crystals, which has advantage of being as the same order of magnitude as the LHC bunch crossing time. The light gain is highly sensitive to the temperature ($-2.1\%^{\circ}C^{-1}$ at 18°C [70]), collecting about 4.5 photo-electrons per MeV are collected in both APDs and VPTs with a gain of about 50 and 10 respectively. ECAL is operated at a steady temperature of 18°C.

The preshower detector which is placed in front of each endcap, covers a region of $1.653 < |\eta| < 2.6$. Its mainly aimed at increasing the granularity of the ECAL endcap

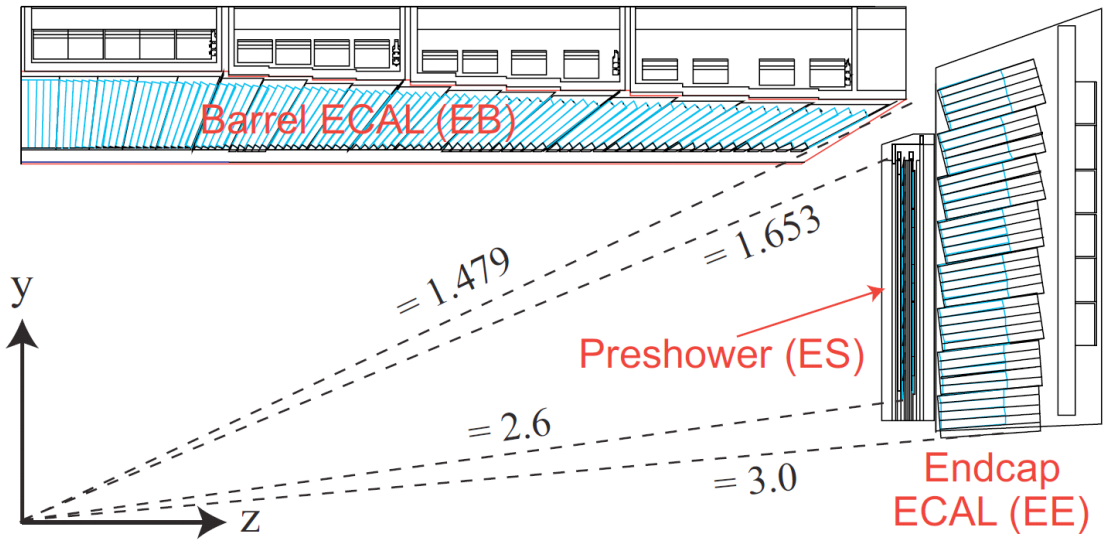

FIGURE 3.7: Sectional view of the quarter of the CMS ECAL [6], where crystals are denoted in light blue, detector boundaries are termed in η.

regions, and thus resolving the diphoton originating from the $\pi^0 \to \gamma\gamma$ processes that could potentially be mis-reconstructed as single photons. It also helps the identification of electrons against minimum ionizing particles. The preshower is a sampling calorimeter consisting of 2 layers of lead instrumented with 2 orthogonal layers of silicon 2 mm width. The total thickness of the preshower is 20 cm, along z direction, corresponding to 3 radiation lengths.

The energy resolution of the ECAL, for incident electrons as measured in a beam test, obtained from Gaussian fits to the reconstructed energy is represented as,

$$(\frac{\sigma}{E})^2 = (\frac{S}{\sqrt{E}})^2 + (\frac{N}{E})^2 + C^2 \tag{3.5}$$

and it takes the following form in the test conditions without magnetic field and without material in front of ECAL,

$$(\frac{\sigma}{E})^2 = (\frac{2.8\%}{\sqrt{E(\,\mathrm{GeV})}})^2 + (\frac{12\%}{E(\,\mathrm{GeV})})^2 + 0.3\% \tag{3.6}$$

In Eq. 3.5 the stochastic term S represents statistical fluctuations on the number of secondary particles produced, N is the noise coming from the electronics, and C is a constant that accounts for inter calibration residuals and for the leak of part of shower outside of the calorimeter. The ECAL is reported to be operating in stable conditions throughout the 2015 and 2016 LHC Run-II operation. The analysis using 2.5 fb^{-1}

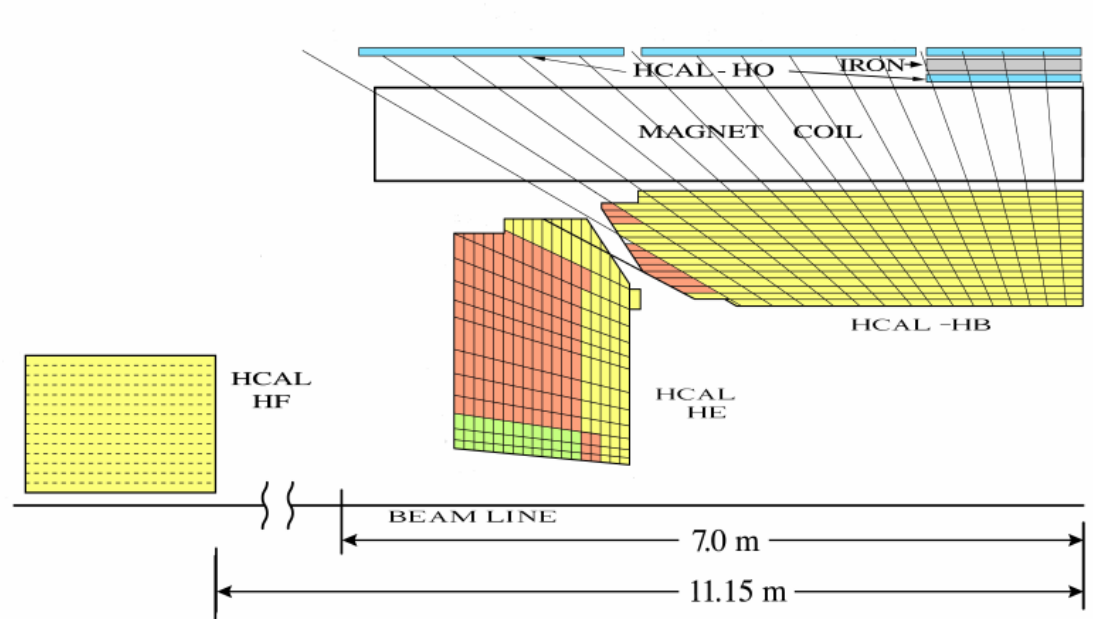

FIGURE 3.8: Longitudinal view of CMS detector showing the physical location of HB, HE, HO and HF [7], where as solid lines extending outwards from the interaction point on the right-bottom corner denote HCAL tower segments and the coloring scheme follows the longitudinal segmentation of each HCAL tower.

collision data collected in 2015 at 13 TeV shows that a relative energy resolution between 1.4-3% for electrons is achieved in the barrel, and 3-4% in the endcap [71].

3.2.3 Hadron Calorimeter

The hadron calorimeter (HCAL) [72] is of particular importance as it measures the hadron jets and neutrinos or exotic particles in apparent missing transverse energy [73]. HCAL is placed in a space restricted on one side by the electromagnetic calorimeter (R = 1.77 m) and on the other side by the magnetic coil (R = 2.95 m). Because of the limited space, the CMS HCAL is compact in design, primarily made from materials with short interaction length. The HCAL is also aided by an outer hadron calorimeter or *tailcatcher* to compensate for its compact size and increase the resolution by catching the tails of the hadronic shower. The HCAL is a hermetic, non-compensating, sampling calorimeter [74], composed of layers of brass absorbers and plastic scintillators, that measures destructively the energy of hadron jets. The forward hadron calorimeter is placed at 11.2 m from the interaction point to extend the pseudorapidity coverage($3.0 < |\eta| < 5.0$). The HF sub-detector is a Cerenkov light detector made up of quartz fibers embedded within a 165-cm-long steel absorber.

Fig. 3.8 shows the longitudinal view of the CMS HCAL. The HCAL detector is organized into four major subsections. These are barrel (HB), endcap (HE), forward calorimeter

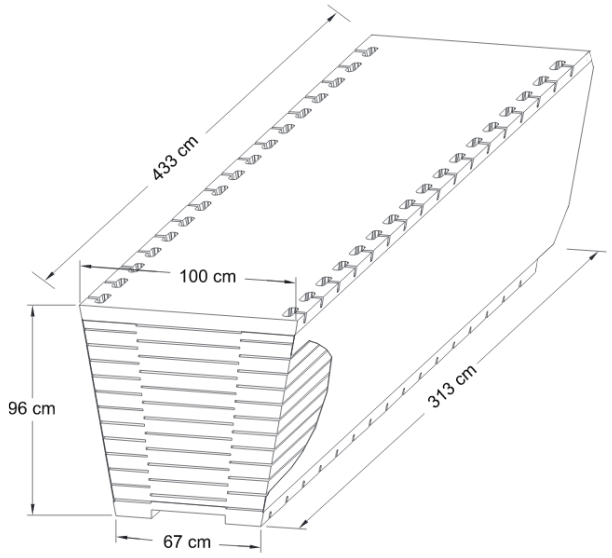

FIGURE 3.9: The isometric projection of an HB wedge [8].

(HF) and outer calorimeter (HO). The HB covers the pseudo-rapidity range up-to 1.4, the HE covers the range from 1.4 to 3.0, whereas the HF covers the range from 2.9 to 5. The outer calorimeter serves to detect escaped particles from inner detectors. There are 18 equal slices in the azimuthal direction for both HB and HE, and they serve as a calorimeter towers (wedges), see Fig. 3.9. The front-end electronics of each of these wedges are housed in read out boxes (RBXs). There are in total 72 RBXs shared between the HB and HE. Each RBX houses 4 hybrid photo detectors (HPDs) [72, 75] which convert the scintillator light into proportional electrical signals. The light collected through scintillators goes via calorimeter towers to HPDs. The general work-flow can be described as: at first, channels collect scintillator light output, then this light is converted into proportional electrical signals through HPDs and finally converted into digital form by analog to digital converters.

HB and HE towers have a granularity of $\Delta\eta \times \Delta\phi = 0.087 \times 0.087$ in $|\eta| < 1.6$, and about $\Delta\eta \times \Delta\phi = 0.17 \times 0.17$ in $|\eta| \geq 1.6$. The outer calorimeter complements the HB detector by detecting and measuring any late showering jets, leaking beyond the HB. The proportion of such late showering jets is about 4.3% for 300 GeV pions. HO utilizes the passive body of the CMS magnet as its absorber layer in rings ± 1 and ± 2, whereas the innermost ring is supplemented by a second iron absorber layer in between the 2 HO scintillators. The total HCAL+ECAL material (excluding HO and HF) provides a minimum of about 7 interaction lengths around $\eta = 0$ in the barrel, increasing up-to 10 in the endcap. HO increases the total minimum depth of the barrel calorimeter system to 11.8 interaction lengths, with the exception of the barrel-endcap boundary region.

The forward calorimeter is a cylindrical steel structure with an outer radius of 130 cm and length of 165 cm. The front face of the calorimeter is located at 11.2 m from the interaction point. The hole for the beam pipe is cylindrical, with radius 12.5 cm from the center of the beam line. The calorimeter consists of still absorber layers with fibers inserted in between them. Due to its peculiar place in front of beam-line, the HF is subject to extremely high particle fluxes and radiation levels thus requiring radiation-hard materials and shielding.The active elements of HF (quartz fibers) are sufficiently radiation-hard to survive very high levels of radiation with limited deterioration. These active elements when struck by particles, yield a Cherenkov light. HF is thus mostly sensitive to the electromagnetic component of the particle showers and practically insensitive to neutrons and to low energy particles from the decay of activated radionuclides [5]. The photo-multiplier tubes (PMTs) are used to convert the light yield into electrical signals, which operate at a bias voltage of 2 kV and delivering the gain of about 10^6.

The ECAL and the HCAL combined can measure the energy of hadrons with a resolution $\Delta E/E \simeq 100\%/\sqrt{E(\,\mathrm{GeV})} + 5\%$. For run-II in 2015-16, the HCAL has gone under major upgrades. The major component of the HCAL barrel and endcap upgrade is the replacement of HPDs with silicon photo-multipliers (SiPMs). The SiPM is an array of Geiger-mode operated avalanche photo-diodes, divided into pixels of micron size. SiPMs exhibit a recovery time of less than 10 ns, ensuring that time-shifts in response from pileup events are minimal. Similarly to the barrel and endcap upgrade SiPM up-grade, the HF has also undergone a replacement of its photo-detectors, in this case an upgrade to new photo-multiplier tubes [76].

3.2.4 Superconducting Magnet

The main feature of CMS is a superconducting solenoid magnet [77], with 6 m in diameter and 12.5 m in length, it surrounds the inner tracking system as well as the electromagnetic and hadron calorimeters and designed to reach at a 4 T with stored energy of 2.6 GJ at full current. It consists of 4-layer niobium-titanium ($NbTi$) coils cooled to around 4.5 K with the help of liquid helium. The flux is returned through a 10000-t yoke comprising 5 wheels and 2 endcaps, composed of three disks each. A schematic is illustrated in Fig. 3.10. The operating magnetic field is restricted to 3.8 T in order to increase the longevity of the solenoid [9].

A uniform high magnetic field combined with high precision on the spatial resolution and alignment of the detectors achieves a good momentum resolution. The momentum measurement of charged particles in the detector is based on the bending of their

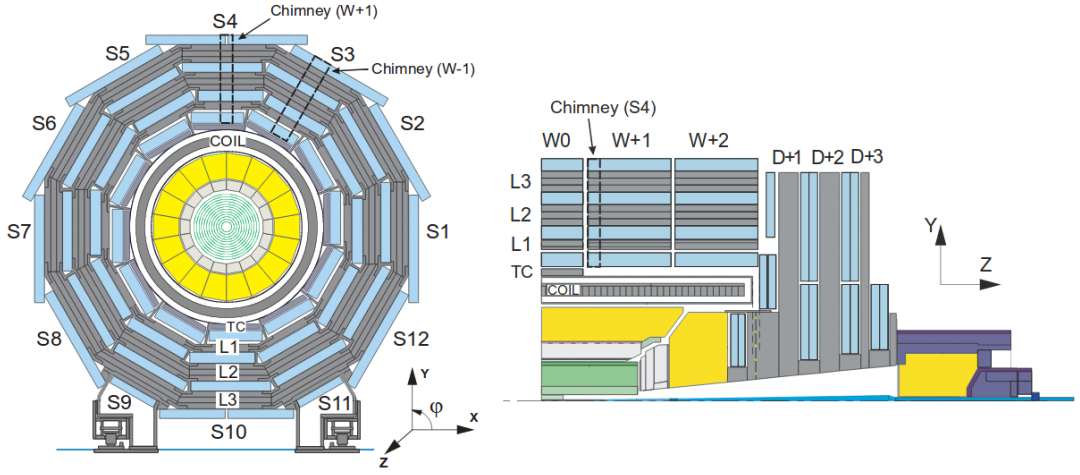

FIGURE 3.10: Schematic views of the CMS detector transverse (left) and longitudinal view of one quarter (right), with the numbering convention for azimuthal sectors (S), wheels (W), barrel yoke layers (L) and endcap disks (D). The magnet are shown in grey, and muon stations in between yoke layers are denoted with light blue. The chimney's shown are used for cryogenic transfer lines and power cables of the magnet system [9].

trajectory. The magnetic field provided by the solenoid is important in achieving the target muon resolution of about 1% at 100 GeV, up to $|\eta| < 2.4$. The 4T magnetic field also bring benefits for calorimetry - it enables the detection of many isolated electrons produced by the decays of W's, and Z's.

3.2.5 Muon System

Muons are charged particles that are just like electrons and positrons, but are 200 times heavier. They are minimum ionizing particles and they leave a very little signature in ECAL and HCAL and generally punches through the yoke, it calls for a separate muon system to detect their path, outside the yolk. CMS fulfill this requirement by employing a separate muon detection system. The muon system [78] is of central importance to CMS, as one of the important goal of the experiment was accurate muon observation. The Muon system's main functions are muon identification, momentum measurement, and contribution to muon triggers. Muon detection has proved to be a powerful tool for recognizing signatures of interesting processes over the period of run-I and run-II in spite of having high background rate.

The muon system is an assembly of three gaseous detectors, located outside the magnetic solenoid, covering a pseudo rapidity region of $|\eta| < 2.4$. The three gaseous detectors are, the Drift Tube chambers (DT), Resistive Plate Chambers (RPC), and Cathode Strip Chambers (CSC) [5, 79]. Fig. 3.11, shows the location and pseudo-rapidity coverage of the muon detectors in CMS.

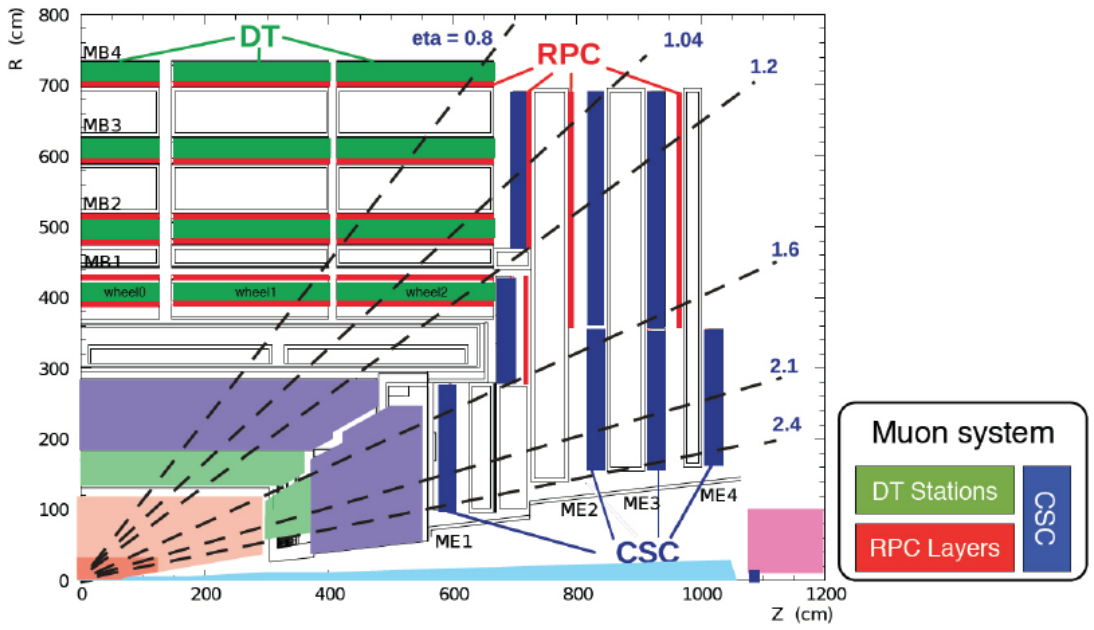

FIGURE 3.11: Longitudinal view of the one quarter of the CMS muon system [6]. The three sub-systems, the drift tube chambers (DTs), resistive plate chambers (RPCs), and cathode strip chambers (CSCs) along with the Muon Barrel (MB) stations are shown.

The muon detector is again cylindrical in shape, barrel section and 2 planar endcap regions. The barrel part extends to $|\eta| < 1.2$, whereas the endcaps, consisting each of four disks, cover pseudorapidities up to $|\eta| < 2.4$. Barrels and endcaps are equipped with 4 muon stations (MBS and MES), each muon station consists of several layers of DTs in the barrel region and CSCs in the endcap region, complemented by RPCs. A mixture of $Ar/CO_2/CF_4$ is employed as a gas which is optimized to suit the design of CMS [80]. A particle is measured by fitting a path to hits among the four muon stations. By tracking its position through the multiple layers of each station, combined with tracker measurements the detectors precisely trace a particle's path. In total there are 1400 muon chambers: 250 DTs and 540 CSCs track the particles positions and provide a trigger, while 610 RPCs form a redundant trigger system, which quickly decides whether to keep the acquired muon data.

Drift tubes are used as tracking and triggering devices in the barrel region of the muon spectrometer. The drift tube system is composed of 4 layers of concentric cylinders in the $|\eta| < 1.2$ region and consists of 250 DT chambers, each of which measures approximately $2m \times 2.5m$. Each DT chamber is composed of 12 layers of drift cell, organized as 3 super-layers (SL) with 4 drift cell layers per SL. A rectangular drift cell with a transverse size of $4.2cm \times 1.3cm$, filled with a $85/15\% Ar/CO_2$ gas mixture. Two SL's measure the coordinate in the CMS bending plane$(r - \phi)$, whereas the other single SL measures the coordinate along the beam line (z) in the 3 innermost station rings. The CMS DTs

design resolution, for single reconstructed hits, is expected to be around$\sim 250\mu$m, for a final resolution of $\sim$100μm for offline segments reconstructed in the $r-\phi$ view [6, 81]. Owing to the upgrades after year 2015, the performance of the first level trigger by means of an early combination of DT spatial resolution with RPC timing response is expected to improve [81].

The CSC system covering $0.9 < |\eta| < 2.4$ in the two endcap regions, serve as tracking and trigger detector in the muon system end-cap regions. Individual CSC chambers are organized in trapezoidal detector chambers arranged, within four disks in each end-cap, in 2 or 3 concentric rings, according to the disk position. The full CSC system presently consists of 540 chambers, 72 of which were installed in the outermost disk layers during long shutdown 1 (2012-2014), completing its design layout. Each chamber filled with $Ar/CO_2/CF_4$ mixture, is made of 6 layers of 9.5 mm-thick arrays of anode wires enclosed between cathode planes. One of the cathodes is segmented with strips of variable width (8.4 to 16 mm) which allow precise position measurement in $r-\phi$ plane. The CSC strip design resolution for single reconstructed hits is expected to vary between roughly 75 and 150μm. A triple readout ganging (applied during run-I), was removed during first long shut down with the refurbishment of the CSC readout electronics in the high-$|\eta|$ region. This upgrade allows to exploit the full detector granularity in turn improving the resolution offline and trigger segments above $|\eta| > 2.1$.

The RPCs are resistive gaseous parallel plate detectors which equip the CMS muon with $|\eta| < 1.6$. Their good timing resolution accounts for their use in trigger. In total 480 chambers, arranged similarly to DT ones are present in the barrel. Whereas 576 chambers, arranged similarly to CSCs are present in the endcaps. CMS employs double gap RPC chambers working in avalanche mode, and filled with the mixture of $C_2H_2F_4/I_{so} - C_4H_{10}/SF_6$ gas. The RPC strips allows measurement in $r-\phi$ plane with precision of around 1 cm whereas the hit timing resolution is around 2 ns. During the long shut down upgrade the fourth endcap layers are equipped with additional 144 chambers, improving trigger efficiency while bringing redundancy to the measurement.

The CMS muon system is designed to achieve a momentum(p_{T}) resolution of $< 10\%$ and $10-15\%$ in the barrel and endcap regions respectively, for muons with $15 < p_{\mathrm{T}} < 100\,\mathrm{GeV}$ and $|\eta| < 2.4$. The trigger muon-system-only trigger efficiencies are found to be $> 95\%$ in 2016 [81]. The upgrades involving muon detectors as well as the added redundancy to the system after run-I have resulted in increased pileup robustness and improved CMS muon identification.

3.3 Trigger and Data Acquisition

At a center-of-mass energy of 13 TeV (during run-II), the total pp cross section is around $72 - 78$ mb [82, 83], which is many orders of magnitude higher than the production cross sections for the most interesting processes at LHC. This yields an average of 25 interactions within the CMS detector per bunch crossing [4]. Considering a typical event size of around 1 MB, recording each bunch crossing with 25 ns intervals can yield 40 TB of data per second [84]. The function of the trigger systems of the CMS experiment is to keep this data acquisition rate in feasible range. In the CMS experiment this is implemented as a two-level system, with the first level (Level-1) based on custom hardware and with a software-based second level (HLT) running on a large farm of computers [85]. With the start of LHC Run II, trigger rates have increased due to the increase in luminosity, the increase in centre-of-mass energy, and by the higher pile-up (the number of interactions per bunch crossing). The CMS detector electronics limit the Level-1 (L1) trigger rate to 100 kHz. The CMS physics program requires the sensitivity for electroweak scale physics and for TeV scale searches be maintained at the level it was in Run I, which motivated the upgrade of the CMS Level-1 trigger system [86].

The L1 Trigger [85] is a hardware implemented fixed latency trigger, which has design output rate of 100 kHz and a response time of around 4 μs. The L1 trigger hardware comprises chiefly of Field Programmable Gate Array technology with application-specific integrated circuits and programmable memory look-up tables used in special case where speed, and radiation resistance are of high importance. The L1 trigger system relies on the coarse information provided by the calorimeters and the muon system to select or reject the objects. A schematic representation is shown in Fig. 3.12.

The information obtained known as trigger primitives (TP) from ECAL and HCAL (the calorimeter trigger) and from the muon detectors are processed in various steps, and the combined event information is evaluated in the global trigger (GT) and the decision is made about event acceptance. After every bunch crossing HCAL and ECAL produces TP based on the transverse energies and quality flags from over 8000 ECAL and HCAL towers. The Regional Calorimeter Trigger(RCT) receives and processes the TP's from ECAL and HCAL, and sends the output to the Global Calorimeter Trigger (GCT). The GCT sorts the electron(or photon), finds physics objects and calculates global quantities such as missing transverse energy. The outputs of GCT are fed to the CMS Global Trigger (GT). In a similar way, the objects identified by muon sub-detectors and sorted by regional muon track finders are transmitted to the Global Muon Trigger (GMT). The task of the GMT is then to merge muon candidates found by more than one system to eliminate possible duplication's of a muon candidate across multiple muon triggers. The GMT also performs further quality checks, so that at final trigger

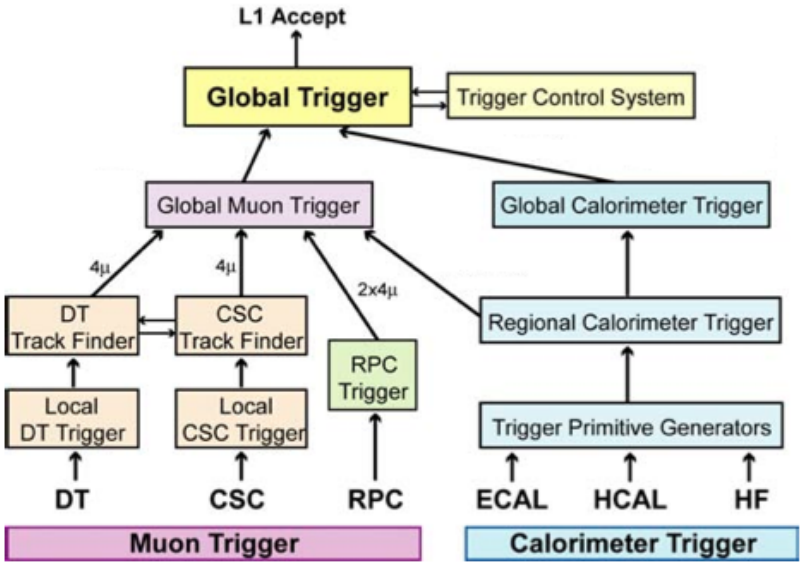

FIGURE 3.12: Schematic of CMS L1 trigger system [5]. It shows the trigger decision flow before data transfer to acquisition system.

stage low quality candidates can be discarded. The GT is the final layer of the CMS L1 trigger, it receives all the trigger objects from previous layer, applies programmable topological selection sets and energy thresholds, as required by the algorithms of High Level Trigger (HLT).

The L1 trigger has gone under number of upgrades before 2016 data taking campaign [86]. The highlights of the upgrades are as follows,

- In the muon track finders the upgrade brings together data from three sub-detectors early in the track finding procedure to improve resolution and robustness in the case of dead detector chambers or channels.
- The upgraded e/γ finding algorithm is based on dynamic clustering, which gives improved energy containment for showering electrons and photon conversions without being affected by pileup.
- The upgraded τ-lepton finding algorithm is also based upon the dynamic clustering optimized for τ-leptons.

The events accepted by L1 trigger are then submitted to the CMS HLT, which performs more complex calculations, based on the information available from different sub-detectors. Objects are reconstructed and identification criteria are applied to select the events which are of possible interest for physics analyses. The HLT is a software based trigger, processed on the single processor farm consisting of commodity computers and

the event filter farm. The event filter farm operates on builder units, which assembles the complete event based on the individual event fragments from the detector. Events accepted by the HLT are sent for the storage. The sorted event data is eventually transferred to CMS Tier-0 computing centre for offline processing and permanent storage.

The dilepton triggers having typical efficiencies around 1, are used in the analysis presented in this dissertation. The full list of the triggers used and efficiency measurement details are given in Appendix B.

Chapter 4

Object Identification and Reconstruction

Various particles interact with different parts of CMS detector and leave traces of their interaction behind. These interaction traces collected from different sub-detectors are combined to reconstruct the path and defining properties (such as momentum, position, energy, and charge etc.) of that particle. The bending of the particle path inside a magnetic field of the CMS detector gives an effective handle to measure the particle momentum. A particle if it is a charged one will leave signatures in the tracker. Short-lived particles like b quarks and short-lived kaons, can also be identified with the tracker. ECAL determines the energy deposited in its crystals by photons, electrons, neutral pions and kaons. HCAL usually identifies the energy deposited by hadrons, jets, which have punched through ECAL. Muons are detected by the specially dedicated muon sub-detectors, whereas neutrinos are inferred from the account of the imbalance in the total energy of the event, termed as missing transverse energy (MET or $E_{\mathrm{T}}^{\mathrm{miss}}$ or $p_{\mathrm{T}}^{\mathrm{miss}}$). An illustration of various particle detection in CMS, is represented in Fig. 4.2.

In addition to the information collected from various sub-detectors, CMS employ "Particle flow"(PF) event reconstruction algorithm to reconstruct an event. Based on the information collected from various sub-detectors, PF algorithm attempt to coherently identify and reconstruct all the particles way back to the pp collision. Other composite objects such as MET, hadronic taus, jets are built with the information from the reconstructed event.

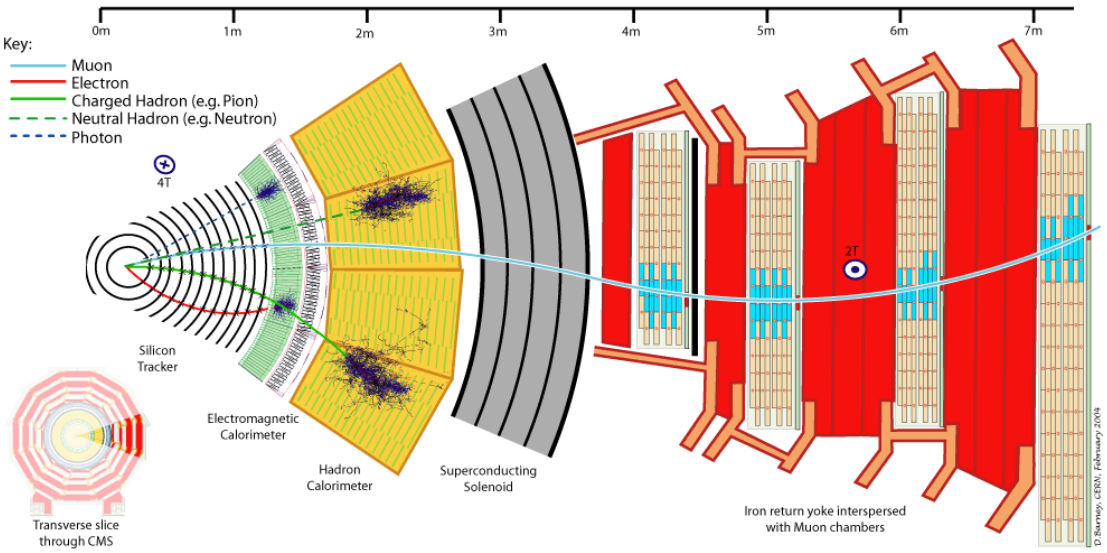

FIGURE 4.1: Various Particle Detection at CMS [10]

4.1 Particle Flow Algorithm

Each CMS sub-detector, is independently capable of fully reconstructing the particle it has interacted with it, thus a combined information may serve as a reconstructed event. A greatly improved event description can be obtained by PF reconstruction [87–89] which correlates the basic elements from all detector layers (tracks and clusters) to identify each final-state particle, and by combining the corresponding measurements to reconstruct the particle properties on the basis of this identification. A PF algorithm requires certain detector properties such as a highly-segmented tracker, a fine-grained electromagnetic calorimeter, a hermetic hadron calorimeter, a strong magnetic field, and an excellent muon detector, all of this are readily possessed by the CMS detector. Thus, a PF algorithm tuned to the CMS detector has been developed. For each collision, the comprehensive list of final-state particles identified and reconstructed by the PF algorithm provides a global event description consisting of jet and hadronic tau decay reconstruction, missing transverse momentum determination, and electron and muon identification. The PF algorithm also allows particles from pileup interactions to be identified and enables efficient pileup mitigation methods.

The information from each sub-detectors, serves as a building bricks, or “elements”, of the particle-flow event reconstruction. The track reconstruction algorithm is performed with an iterative tracking strategy, which achieves a high efficiency and a low misidentification rate. A calorimeter clustering algorithm is employed to reconstruct neutral particles and to complement the tracking to measure the energy of charged particles among others. Particle candidates in an event are reconstructed based on tracks and calorimeter clusters that are linked together using a linking algorithm, resulting in a

list of PF candidates found in the event. A single particle can give rise to the multiple PF elements such as a track and several calorimeter clusters, thus the link algorithm is performed for each pair of elements in the event and defines a distance between any two linked elements to quantify the quality of the link. The link algorithm gets rid of any possible double counting from different detectors.

4.2 Tracks and Vertex Reconstruction

Charged particles follow a helical path parallel to the magnetic field inside the CMS detector. These particles leaves energy deposits (hits) along their trajectories in the inner tracking system 3.2.1. The path of the charged particle reconstructed on the basis of hits, is commonly referred as a track. Charged particle tracks are of great importance of reconstructing the collision events, contributing to the reconstruction of electron, muons, tau, hadron candidates and also in determination of primary interaction and displaced vertices. Track reconstruction [90] is based on the collection of hits from the pixel and strip trackers and is performed by the Combinatorial Tracker Finder (CTF) algorithm, , which is an adaptation of the combinatorial Kalman filter [91–93], which in turn is an extension of the Kalman filter [94] to allow pattern recognition and track fitting to occur in the same framework.

The collection of reconstructed tracks is produced by multiple passes (iterations) of the CTF track reconstruction sequence, in a process called iterative tracking. Initially tracks are seeded and reconstructed with very tight criteria, leading to a moderate tracking efficiency, but a negligibly small fake rate. The next steps proceed by removing hits unambiguously assigned to the tracks found in the previous iteration, and by progressively loosening track seeding criteria. An iteration typically consists of four steps. In the first step, a seed defining, the initial estimate of the trajectory parameters and their uncertainties, provides initial track candidates made up of typically 2-3 hits. In second step, track finding, based on Kalman Filter extrapolates the seed trajectories along the expected flight path of a charged particle, searching for additional hits that can be assigned to the track candidate. In third step, track candidates are fitted with a Kalman filter and smoother, to provide the best possible estimate of the parameters of each trajectory. Finally, track selection sets quality flags, and discards tracks that fail certain specified criteria. The track reconstruction efficiency for isolated muons with $1 < p_{\mathrm{T}} < 100\,\mathrm{GeV}$ is over 99%, while the fake rate is completely negligible [90].

In this thesis, particles originating from the hard collision of two protons are vital, thus it is very important to identify the point of origin *i.e.* the primary vertex. Reconstructed

tracks, together with pixel-based beam spot measurement are used to reconstruct primary vertices in the event including the "signal" vertex and any vertices from pileup collisions. From the available prompt tracks in an event, the tracks are chosen on the basis of their compatibility with the beam spot, number of hits and fit quality.

Tracks which are close to each other in primary interaction region in the z-direction are clustered to form primary vertex candidates using the Deterministic Annealing (DA) clustering algorithm [95]. After identifying candidate vertices based on the DA clustering in z, those candidates containing at least two tracks are then fitted using an adaptive vertex fitter [96] to determine the vertex characteristics. Each vertex, based on the sum of track weights (between 0 and 1), is assigned a number of degrees of freedom,

$$n_{dof} = -3 + 2 \sum_{N_{tracks}}^{i=1} w_i \tag{4.1}$$

The variable n_{dof} can be used to identify the true pp interactions and to reduce vertex fake rate as well. Reconstructed vertices are sorted according to the $\sum p_{\mathrm{T}}^2$ of the tracks found in the track cluster. The vertex corresponding to the highest $\sum p_{\mathrm{T}}^2$ is considered primary vertex and in this analysis as well.

4.3 Jets and Missing Transverse Momentum

A jet is a extremely useful experimental "object" defined as a cluster of reconstructed objects such as tracks, calorimeter tower deposits, and particle candidates. It is useful in the sense that it acts as a representative of hadrons from quark and gluons, which otherwise can not be observed as isolated particles. Charged and neutral hadrons are the major component in a jet along with smaller contributions from heavier masons and baryons. A Jet algorithm provides a mapping between the partons, hadrons and the detector signatures. In the CMS collaboration, several jet algorithm have been developed of which anti-k_t jet clustering algorithm is of relevance in this analysis.

The anti-k_t reconstruction algorithm [97, 98] clusters individual objects to form a jet. In a given collection of input objects, it defines the distances d_{iJ} between objects (particles, pseudo-jets) i and j , and distances d_{iB} between an object and the beam(B). The inclusive clustering proceeds by identifying the smallest of the distances. If the smallest distance is d_{iJ}, it recombines them into a new object, whereas if the smallest one is d_{iB} i is considered as a jet and gets removed from the list of objects. The whole procedure is repeated with recalculated distances until no objects are left.

The distances for anti-k_t are governed by following formulas,

$$d_{ij} = min(k_{ti}^{-2}, k_{tj}^{-2})\frac{\Delta_{ij}^2}{R^2} and d_{ib} = k_{ti}^{-2} \tag{4.2}$$

where k_{ti} and k_{tj} are the transverse momenta of the i and j objects respectively, $\Delta_{ij}^2 = (\phi_i - \phi_j)^2 + (\eta_i - \eta_j)^2$, and R is a cone parameter chosen to be 0.4 in CMS in Run-II, commonly referred as AK4 jets.

The anti$-k_t$ is an infrared and collinear (IRC) safe as well as a fast (requiring less computational time) algorithm. An IRC safe algorithm provide stable set of reconstructed jets even if the given event is modified by a collinear splitting of a hard parton by the addition of a soft emission , and are important in yielding experimental measurements comparable to fixed-order perturabative QCD calculations [99]. Typical jet energy resolutions at the central rapidities are 15-20% at 30 GeV, about 10% at 100 GeV, and 5% at 1 TeV [100].

A number of jet energy corrections are applied to reconstructed jet objects, to ensure uniform response in η and an absolute calibration in p_{T}. The aim of the jet energy calibration is to relate the energy measured for the detector jet to the energy of the corresponding true particle jet. The correction is applied in the form of four multiplicative factor to raw jet four-momentum vector p_{T}. These factors are [101],

- An offset correction, to remove the excess energy (includes contributions from electronics noise and pile-up) not associated with the hard scattering.
- A MC scale factor, corrects for the reconstructed energy to match with simulated MC jet energy.
- Relative Jet Energy Scale, to correct for the resolution bias effect. This correction factor flattens the energy response with respect to pseudorapidity.
- Absolute Jet Energy Scale, to make the energy response uniform with the transverse momentum.

Jets in this analysis are required to have $p_{\mathrm{T}} \geq 30\,\mathrm{GeV}$ and $|\eta| \leq 3.0$ and satisfy quality criteria that remove contributions from pileup. All the above mentioned jet energy corrections are applied in the form of systematic uncertainties and discuss in 6.6.

Neutral weakly interacting particles, such as neutrinos or other hypothetical particles, typically goes undetected by all of the CMS sub-detectors. The presence of such particles is then indirectly accounted by the imbalance of total momentum. The vector momentum imbalance in the plane perpendicular to the beam direction is known as a missing transverse momentum, its magnitude is called as missing transverse energy and

denoted by $p_{\mathrm{T}}^{\mathrm{miss}}$ or $E_{\mathrm{T}}^{\mathrm{miss}}$ or interchangeably. The precise measurement of $p_{\mathrm{T}}^{\mathrm{miss}}$, relies strongly on the reconstruction and correct identification of all other physics objects. Missing transverse energy is one of the most important observable in this analysis, as the dominating backgrounds arises from discriminating leptonic decays of W bosons and top quarks from background events which do not contain neutrinos, such as multijet and Drell-Yan events. Also, the fact that final signal regions are binned in the form of $p_{\mathrm{T}}^{\mathrm{miss}}$.

$p_{\mathrm{T}}^{\mathrm{miss}}$ is calculated using the PF algorithm is the most commonly used type and is inferred from the magnitude of the negative vectorial sum p_{T} of the other PF objects,

$$\vec{p_{\mathrm{T}}}^{\mathrm{miss}} = -\sum_{i} \vec{p_{\mathrm{T}}}_{,i} \tag{4.3}$$

where the magnitude of this vector is the missing transverse energy.

As the reconstruction of $p_{\mathrm{T}}^{\mathrm{miss}}$ depends upon the correct estimation of other objects, it is very sensitive to particle momentum mis-measurements, particle misidentification, detector malfunctions, particles impinging on poorly instrumented regions of the detector, cosmic-ray particles, and beam-halo particles, which may result in artificial excess in $p_{\mathrm{T}}^{\mathrm{miss}}$ [73, 102]. Type 1 corrected PF $p_{\mathrm{T}}^{\mathrm{miss}}$ [103] is used in this analysis. The corrections in the context of other objects are applied on the missing energy measurement and are added as systematic uncertainty in this analysis 6.6.

4.4 Electron: Reconstruction, Identification and Selection

4.4.1 Reconstruction

Electrons are lightest charged leptons which leaves the tracks in tracking system and deposits large fraction of its energy in ECAL. Electrons are reconstructed by associating a track with a cluster of energy in the ECAL, by using a mixture of a a stand-alone approach and PF algorithm [104]. Electron reconstruction is quite challenging owing to the fact that it looses significant (on an average 33% at $\eta = 0$ and up to 86% if in front of budget material) energy before reaching to the ECAL due to photon radiation (Bremsstrahlung) in tracker material. Thus spreads along the ϕ direction because of the bending of the electron trajectory in the magnetic field becomes important.

Due to the different geometries of barrel and endcap, the clustering of the electron energy proceeds with different algorithm in these sub-detectors. In the barrel, the algorithm is designed to take advantage of geometry by collecting energy in small window in η and an extended window in ϕ. It starts with seed crystal that contain the largest energy above

1 GeV. Arrays of 5×1 crystals in $\eta \times \phi$ are added in range of 0.3 rad crystals in both directions of ϕ having minimum energy of 0.1 GeV. The contiguous arrays are grouped into clusters such that each has energy more than 0.35 GeV. A super-cluster(SC) is then formed by these clusters. In the ECAL endcaps where crystals are not arranged in an $\eta \times \phi$, the multi-5×5 algorithm is used. It also starts with a seed crystals, the ones with highest energy relative to their neighbors, satisfying the minimum seed energy criteria of 0.18 GeV. The energy is collected in the form of primary clusters of 5×5 crystals, arranged around seed crystals. Secondary clusters of 5×5 crystals are centered around crystals that are no further than 0.3 in the ϕ-direction and 0.07 in the η-direction from seed crystal. A supercluster is formed with a primary cluster and all the secondary crystals having minimum energy of 1 GeV. The energy collected from the preshower is added to the supercluster. The supercluster's energy is taken as the sum of energy of all its constituent clusters, where as the position is determined by a the energy-weighted mean of the cluster positions. The minimum energy requirements were modified at the start of runs to have a good performance over wider range of p_{T} values.

Electron tracks, like any other charged particle tracks, can be reconstructed by standard Kalman Filter(KF) track reconstruction method. At the same time, the large radiative losses for electrons in the tracker affects the efficiency of the algorithm and leads to a poor estimation of track parameters. Thus, a dedicated tracking procedure is adopted for electrons.The electron track reconstruction in CMS comprises of two steps: the seeding and tracking. The seeding step uses two complementary algorithms, the results of which are combined. The ECAL-based seeding selects electron seeds from reconstructed seeds on the basis of SC energy and position, used to estimate the electron trajectory in the first layers of the tracker. The tracker-based seeding depends upon tracks, reconstructed with general algorithm for charged particles, that are matched to a supercluster after extrapolation towards the ECAL. To account for the energy loss of the electrons in the tracker, the Gaussian Sum Filter (GSF) algorithm is used for track parameter estimation from a hit collection obtained with KF algorithm, by approximating the Bethe-Hetler distribution with a sum of Gaussian distributions. Tracks and superclusters are matched to each other in GSF electron candidates. PF clustering is based on GSF tracks and does not depend upon how these tracks are seeded. An electron PF cluster is comprised of several PF clusters corresponding to the electron at the ECAL surface and the radiated photons emitted along its trajectory, for each GSF track.

The charge is estimated by combining three methods: the sign of GSF track curvature; Second method is based on KF track associated to a GSF track if they share at least one innermost heat; Third method defines the charge sign as the sign of ϕ differences between the vector joining the beam spot to the SC position, and the vector joining the beam spot and the first hit of the electron GSF tracks. The final charge is the one given

by at-least two of the methods. This reduces the charge misidentification rate to 1.5% for reconstructed electrons from Z boson decays.

The electron momentum is estimated from a weighted combination of the measurements from track parameters and from supercluster parameters. The track parameter combination is dominant for low energy candidates whereas the supercluster parameter combination is weighed more for high energy candidates.

4.4.2 Identification

Several variables are employed by CMS to discriminate prompt isolated electron from backgrounds of hadronic activity. They are grouped into following categories,

- The observables that check the agreement between the measurements obtained from the ECAL and the tracker.such as
  - $\Delta\eta_{in}$ and $\Delta\phi_{in}$ which are used to match the electron to the energy deposit in the ECAL in η and ϕ direction, to remove the possibility of track matching to the charged pion.
- The observables based on calorimeter information only. Such as,
  - H/E, the ratio of energy deposited by the electron in the HCAL to ECAL, again used for pions discrimination as pions will have the higher value of this ratio.
- The observables based on tracking measurements. Such as,
  - The compatibility between the KF- and GSF-fitted tracks.

Enhance sensitivity of electron isolation is achieved by combining the several variables by Multi-Variate Analysis (MVA) techniques. The MVA identification combines variable in "boosted decision tree"(BDT) format to obtain a final discriminator on which a cut is applied. The thresholds on the BDT output depends on the electron transverse momentum and pseudorapidity.

Another important discriminator is an isolation parameter for the electron, used for rejection of non-prompt or misidentified leptons. However isolation requirements are separated from electron identification, as they are relative to each other and their interplay depends upon the analysis. The PF isolation which is used in this analysis is defined as

$$Iso_{PF} = \sum p_{\mathrm{T}}^{charged} + max[0, \sum p_{\mathrm{T}}^{neutralhad} + \sum p_{\mathrm{T}}^{\gamma} - p_{\mathrm{T}}^{PU}] \tag{4.4}$$

where the sum runs over charged PF candidates, neutral hadrons and photons originating from primary vertex, within a chosen ΔR cone around the electron direction. p_{T}^{PU} is the correction related to the event pileup. The relative isolation of an electron is the ratio of isolation to its transverse momentum.

4.4.3 Electron Selection for the Multilepton Search

Electrons are selected with the medium working point(average efficiency$\sim$ 80%) of the cut-based electron ID recommended by the EGamma POG and need to satisfy $d_z <$ 0.10(0.20) cm and $d_{xy} <$ 0.05(0.10)cm in EB (EE) [105]. Furthermore, in order to emulate the trigger level isolation cuts, electrons are required to satisfy a relative HCAL isolation of less than 0.15, a relative ECAL isolation of less than 0.15, and a relative tracker isolation of less than 0.2. The relative isolations are defined as the ratio of total transverse energy deposited in the ECAL, HCAL, or the total transverse momentum of the tracks in the tracker within a cone of $\Delta R < 0.3$ around the electron over the electron p_{T}. The ECAL and HCAL isolation quantities are ρ-corrected to mitigate the effects of pileup, whereas the tracker isolation is computed over tracks originating from the same primary vertex as the electron. The trigger level electron quality cuts are emulated by requiring the electrons to also have $H/E <$ 0.0414(0.0641) in EB (EE), and $1/E - 1/p <$ 0.05, where the H/E and $|1/E - 1/p|$ quantities are calculated as recommended by the EGamma POG. A loose selection is also defined for electrons for the matrix method, where the veto working point of the cut-based electron ID without its built-in isolation requirement is used instead of the medium working point.

4.5 Muon: Reconstruction, Identification and Selection

4.5.1 Reconstruction

The muon reconstruction is based upon, the independently reconstructed tracks from inner tracker known as *tracker track* and tracks constructed in the muon system known as *standalone-muon track* [106]. Two reconstruction approach are used based on these objects,

- Outside-in or Global Muon Reconstruction: In this reconstruction, each standalone-muon track is matched to a tracker-track by comparing parameters of the two

tracks propagated onto a common surface. Using the Kalman-filter technique a global muon track is fitted by combining hits from tracker-track and standalone muon track. The global muon fit is particularly useful at large transverse momenta ($p_{\mathrm{T}} \gtrsim 200$ GeV) as compared to the tracker only fit.

- Inside-out or Tracker Muon Reconstruction: Candidate tracker tracks are extrapolated to the muon system taking into account the magnetic field, the average expected energy losses, and multiple Coulomb scattering in the detector material. The extrapolated tracks with $p_{\mathrm{T}} > 0.5$ GeV and total momentum $p > 2.5$ GeV are then matched with at least one muon segment, if matched, it is qualified as Tracker Muon. Tracker muon reconstruction is more efficient than the global muon reconstruction at low momenta.

Due to the their excellent efficiency coverage at low and high momenta, around 99% of muons are reconstructed by one of the approach mentioned above, and more than often muons are reconstructed by both the reconstructions. Candidates found both by the Global Muon and Tracker Muon reconstruction are merged into a single candidate if they share the same tracker track.

For muons, the particle-flow algorithm applies applies a particular selection criteria to the muon candidates reconstructed with the Global and Tracker muon algorithm. The selection criteria are adjusted depending upon the environment (isolation etc.) of the muon making use of information of from other sub-detectors (such as energy deposition in calorimeters etc.). The selection is motivated by the identification of muons within jets with high efficiency, while lowering the misidentification rate of charged hadrons as muons. Further details about particle flow muon selection are described elsewhere [87, 89].

Due to the upgrades in the muon system at the start of the run-II, the muon track reconstruction has improved [81, 107]. New algorithm to recover the small efficiency loss during run-I is added, also the local reconstruction in the barrel muon chamber has been improved. The stand alone muon reconstruction and displaced muons produced within the tracker volume, with the muon leaving hits both in the inner tracker and in the muon chambers are also the cases which has been benefited by the upgrades.

4.5.2 Identification

Different identification variables are combined with MVA techniques to come up with identification working points, on the basis of which the muon quality is judged. Particle flow muons are used exclusively in this analysis and other identifying variables are,

- *Impact Parameter* (IP): The transverse impact parameter is useful to select either prompt muons or, by inverting the requirement, muons from heavy-flavor decays.
- $\chi^2/ndof$ of a tracker-track fit is a discriminant to suppress muons from decays in flight. The $\chi^2/ndof$ determines the quality of muon trajectory.
- *Number of hits in the muon chambers* ensures that muons do not come from hadronic punch-throughs or in flight decays.
- *Number of hits in the tracker* for a good p_{T} measurement.
- *Relative Isolation*: The PF isolation is described in section 4.4.2. The relative isolation of an electron is the ratio of isolation to its transverse momentum. The relative isolation is used to reject the muons from hadronic activity (or the muons which are constituent of jets).

4.5.3 Selection for Multilepton Search

Muons are required to satisfy the medium working point(average efficiency$\sim 95-98\%$ of the Muon POG supported muon ID and the loose working point of the relative, pileup corrected PF-based isolation [108]. In addition, muons have to satisfy $d_z < 0.1$ cm and $d_{xy} < 0.05$ cm, where d_z and d_{xy} are the longitudinal and transverse impact parameters with respect to the primary interaction vertex, respectively. In order to emulate the isolation cuts used for muon candidates at the trigger level, the relative tracker isolation of muons, defined as the sum of all transverse momentum of tracks originating from the same primary vertex as the muon candidate and within a cone of < 0.4 around the muon divided by the muon transverse momentum, is required to be less than 0.4. For the purposes of the matrix method described in Section 6.4, a loose muon selection is defined where the pileup corrected PF-based isolation requirement is dropped and the muon ID is relaxed to the loose working point.

4.6 Hadronic Tau: Identification, Reconstruction and Selection

4.6.1 Reconstruction

In about 33% case tau leptons decays leptonically, where as the remaining decays are hadronic where it decays to to a combination of charged and neutral mesons with a tau neutrino. Muons and electrons from tau leptonic decays are reconstructed same

as any muons and electrons described in section 4.5 and 4.4 respectively. Three light lepton(muons and electrons) channels considers light leptons originating from taus as well, whereas two light lepton plus a tau channels, considers one or more hadronic tau in the multileptonic final state.

Hadronically decaying taus are reconstructed and identified with the hadron plus Strips (HPS) algorithm [109, 110] primarily in run-I. The challenging part in identifying hadronic τ decays is distinguishing them from quark and gluon jet background. The cross section for multijet production from perturbative quantum chromodynamical (QCD) calculations exceeds by many orders of magnitude the rate at which τ leptons are produced at the LHC. The HPS algorithm starts with reconstructed jets as seeds, it looks into the constituent of jets to reconstruct the neutral pions that indicates hadronic tau (τ_h) decays. The photon and electron($p_{\mathrm{T}} > 0.5\,\mathrm{GeV}$) constituents are collected into clusters (*strips*) on account that there is a high probability for photons originating from $\pi^0 \to \gamma\gamma$ decays to convert into e^+ e^- pairs. The size of the strips is set to a fixed value of 0.005×0.20 in the $\eta - \phi$ direction during run-I. If a strip contains more than one or more electron or photon, such that the transverse momentum sum of electron plus photons exceeds 2.5 GeV, is kept as π^0 candidate for further processing. The strips and the charged-particle constituents are then combined to form τ_h candidates. *Decay modes* are assigned on the basis of observed number of strips and charged particles, as follows,

- *Three prongs–*$h^-h^+h^-$: Combination of three charged particles; the charges should not be identical and their invariant mass should lie between 0.8 to 1.5 GeV. This mode aims at reconstructing $\tau^- \to h^-h^+h^-\nu_\tau$ and $\tau^- \to h^-h^+h^-\pi^0\nu_\tau$ decays. The efficiency in later case is low.
- *One prong plus two strips–*$h^-\pi^0\pi^0$: Combination of a single charged particle with two strips; it should satisfy the condition on tau mass $0.4 < m_\tau < 1.2\sqrt{p_{\mathrm{T}}(\,\mathrm{GeV})/100}$ GeV. The p_{T} limit dependence in the upper limit accounts for resolution effects.
- *One prong plus one strip–*$h^-\pi^0$: Combination of one charged particle and one strip; The condition on tau mass $0.3 < m_\tau < 1.3\sqrt{p_{\mathrm{T}}(\,\mathrm{GeV})/100}$ GeV should be satisfied.
- *One prong–*h^-: A single charged particle without any strips. The reconstructed tau mass of is fixed at the mass of a charged pion.

The shrinking cone algorithm takes into account that the decay products of taus with higher p_{T} are more collimated, it requires that all charged hadrons and strips should fall

within a single cone ($\Delta R = 3.0/p_{\mathrm{T}}(\,\mathrm{GeV})$) around the momentum vector of tau candidate. Hadronic taus are said to to pass the decay mode discriminator, if reconstructed by any of the above mentioned mode.

The strip reconstruction of the HPS algorithm is improved for run-II as dynamic strip reconstruction [11], as opposed to a fixed one in run-I in order to optimize the strip size.

4.6.2 Identification

Taus are more collimated and isolated than quark and gluon jets, this fact gives a main handle to distinguish between these two object. Requiring τ_h candidates to pass isolation reduces the jet $\rightarrow \tau_h$ misidentification probability. Two types of isolation discriminators have been designed to achieve the lower misidentification probability against jets, isolation-sum and MVA based.

For isolation-sum discriminator, the transverse momenta of of charged particles and photons of $p_{\mathrm{T}} > 0.5\,\mathrm{GeV}$ reconstructed with PF algorithm, within an isolation cone of $\Delta R = 0.5$(0.3 in busy environments) are summed up to get the isolation of τ_h candidate, centered around its direction. The charged hadrons and the photons which are constituents of τ_h candidate are excluded from the sum of transverse momenta. The contribution from jet pileup is reduced by requiring the tracks associated to charged particles to originate from the production vertex of the τ_h candidate, within $d_Z < 0.2$ cm. The pileup contribution to the photon isolation is calculated as summation of transverse momenta of charged particles within cone of size $\Delta R = 0.8$ centered around τ_h direction and by not considering tracks which originate from near τ_h production vertex, $d_z > 0.2$ cm. This contribution is then subtracted from photon isolation by scaling with factor $\Delta\beta$, all the while considering the different cone size as well as the ratio of neutral to charged hadron production. The tau candidate isolation is then given by,

$$\mathrm{I}_\tau = \sum p_{\mathrm{T}}^{charged}(d_z < 0.2cm) + max(0, \sum p_{\mathrm{T}}^{\gamma} - \Delta\beta \sum p_{\mathrm{T}}^{charged}(d_z < 0.2cm)) \tag{4.5}$$

In Run-I an empirical factor of 0.46 was used to scale the $\Delta\beta$ corrections [109], where as $\Delta\beta = 0.2$ is used, which is obtained by fitting the $\sum p_{\mathrm{T}}^{charged}$ as a function of $\sum p_{\mathrm{T}}^{\gamma}$ to obtain a pileup insensitive τ_h identification efficiency [11].

The Loose, Medium and Tight working points of isolation-sum based discriminators are defined as, 2.5, 1.5 and 0.8 GeV, respectively for run-II. Dynamic strip construction used in the run-II provides further handle to reduce jet$\rightarrow \tau_h$ misidentification rate.

The MVA τ_h identification discriminator takes advantage by combining the isolation shape variables with variables depending upon τ-lifetime to lower jet$\rightarrow \tau_h$ misidentification rate. Following variables are used in BDT which combines them all and provides with discriminator output,

- The charged particle energy in the isolation and signal cone $p_{\mathrm{T}}^{charged}$;
- The neutral particle energy in isolation and signal cone;
- The reconstructed tau decay mode;
- The tau candidate pseudorapidity and momentum;
- The transverse impact parameter d_0 of the leading track of tau candidate and its significance (d_0/σ_{d_0});
- In the case of three prongs taus, the distance between the tau production and decay vertices, $|\vec{r}_{sv} - \vec{r}_{pv}|$ and its significance;
- The $\Delta\beta$ corrections;
- Shape variables: $p_{\mathrm{T}}^{strip,outer}$ and p_{T} weighted $\Delta R, \Delta\eta$ and $\Delta\phi$ of photons and electrons in strips inside or outside of signal cone;
- τ-lifetime information;

The BDT is trained on simulation samples such as $\mathrm{Z}/\gamma^* \rightarrow \tau\tau, \mathrm{W} \rightarrow \tau\nu, \mathrm{H} \rightarrow \tau\tau, \mathrm{Z}' \rightarrow \tau\tau$ and $\mathrm{W}' \rightarrow \tau\nu$. The τ_h candidates are selected with $p_{\mathrm{T}} > 20\,\mathrm{GeV}$ and $|\eta| < 2.3$. The jet$\rightarrow \tau_h$ misidentification rate as a function of expected τ_h identification efficiency for both isolation-sum and MVA-based discriminators are shown in Fig. 4.2, which shows the MVA advantage. Different working points of MVA isolation discriminator, for different efficiencies, are defined by cuts on BDT discriminant.

There is a high probability that muons to be reconstructed as hadronic taus, specially in the h^- decay mode. Again a BDT is designed which is based on the following information to guard against this misidentification rate,

- ECAL and HCAL energy deposits of any charged particle or photon of the tau candidate.

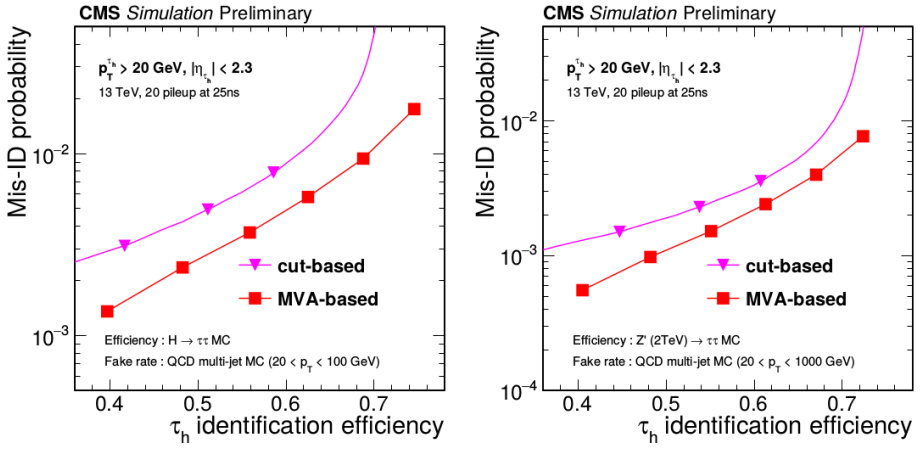

FIGURE 4.2: Misidentification probability as a function of τ_h identification efficiency.The MVA-based discriminators are compared to that of the isolation sum discriminators. The points correspond to working points of the discriminators.The misidentification probability is calculated with respect to jets, which pass minimal τ reconstruction requirements. [11]

– The energy fraction carried by the leading charged particle of a tau candidate.

– The number of track segments in muon system and the number of muon station that at least have a hit within a cone of $\Delta R = 0.5$ around tau direction.

– The pseudo rapidity of the tau candidate.

The BDT is trained on $Z/\gamma^* \rightarrow \tau\tau, Z/\gamma^* \rightarrow \mu\mu, Z^{'} \rightarrow \mu\mu, W \rightarrow \tau\nu, W \rightarrow \mu\nu, t, H \rightarrow \tau\tau, Z^{'} \rightarrow \tau\tau, W^{'} \rightarrow \tau\nu$ and $W^{'} \rightarrow \mu\nu$. Different working points of MVA isolation discriminator, for different efficiencies, are defined by cuts on BDT discriminant.

Electrons crossing the tracker material often radiate photons mimicking πs in the decay mode reconstruction. Such cases and isolated electrons have a high probability to be misidentified as τ_h that decays to either $h^{\pm}$ or $h^{\pm}\pi$. As with the case of muon and jets, a BDT electron discriminator is designed to reduce the $e \rightarrow \tau_h$ misidentification probability. Following variables are used as a input to the BDT in run-II [11, 109],

– The electromagnetic energy fraction $E/(E+H)$ for a tau candidate;

– E/P and H/P where E and H denotes the amount of the energy in the ECAL and HCAL of the leading track of a tau candidate, P denotes the transverse momentum of this track;

– The fraction of the tau candidate energy carried by photons;

- $(P_{in} - P_{out})/P_{in}$ where P_{in} and P_{out} denotes the GSF track momentum measured by the curvature of the track at the innermost and outermost position;
- The ratio between radiated photon energy measured in the ECAL and tracker.
- $(N_{hits}^{GSF} - N_{hits}^{KF})/(N_{hits}^{GSF} + N_{hits}^{KF})$, where N_{hits}^{GSF} is the number of hits in the silicon pixel plus strip tracking detector associated to the track reconstructed by GSF algorithm, similarly N_{hits}^{KF} denotes the same for Kalman Filter algorithm;
- The pseudorapidity, the transverse momentum, and the mass of the tau candidate;
- $\chi^2/ndof$ of the GSF track;
- The transverse momentum along with its significance and the pseudorapidity of the GSF track;
- The distances in η and ϕ directions between the GSF track and the nearest boundary between ECAL modules;
- The number of photons in any of the strips associated with the τ_h candidate;
- the p_{T}-weighted mean distances in η and ϕ between all photons included in any strip and the leading track of τ_h candidate;

The BDT is trained on the various Monte Carlo (MC) samples as mentioned previously. Different working points are defined on the BDT discriminator according to efficiency for real τ_h to be identified.

4.6.3 Selection for Multilepton Search

Tau candidates with $p_{\mathrm{T}} > 20$ GeV, $|\eta| < 2.3$ are selected using hadron-plus-strips (HPS) reconstructed in 1- or 3- prong decay modes with or without additional π^0 particles [11, 109–111]. The tau candidates are required to pass byVTightIsolationMVArun2v1DBoldDMwLT isolation working point of tau POG [112]. Additionally longitudinal impact parameter of candidates from primary vertex if required to be < 0.2. In order to remove misidentified tau candidates originating from electrons or muons we require all candidates to also pass againstElectronTightMVA6, againstMuonTight3 Tau POG recommended discriminators as well. A looser tau selection for the prediction of fake tau background in matrix method is also defined, for this selection the isolation is relaxed to byVLooseIsolationMVArun2v1DBnewDMwLT.

Chapter 5

The Multilepton Search

As introduced in chapter 2, among proposed extensions of the Standard Model (SM) that explain neutrino mass, models based on the seesaw mechanism are an appealing possibility [113–121]. The seesaw mechanism introduces new heavy particles that couple to leptons and to a Higgs boson (H) doublet, and accounts for the smallness of neutrino masses [122–124]. Within the type-III seesaw model [119], the neutrino is considered a Majorana particle whose mass arises from the mediation of new massive fermions that form an SU(2) triplet of heavy Dirac charged leptons $\Sigma^{\pm}$ and a heavy Majorana neutral lepton Σ^{0}. In pp collisions, these massive fermions may be pair-produced through leading order electroweak interactions, in both charged-charged and charged-neutral pairs, as seen in Fig. 5.1 The renewed interest in the type-III seesaw models emphasizes the importance of exploring such signatures at the CERN LHC [53–58].

This analysis searches for new massive fermions by looking into the final states with at least three electrons and muons(including those that come from the decays of tau leptons) [51, 125]. A possible extension is discussed in chapter 8 examines the search region involving 3 leptons, one of which is always a hadronic tau. This extension would be useful where the branching ratios are more in favor of tau leptons.

The final states arise with three or more charged leptons arise from the following decays,

- $\Sigma^{\pm} \to W^{\pm}\nu_{\ell}$
- $\Sigma^{0} \to W^{\pm}\ell^{\mp}$
- $\Sigma^{\pm} \to Z\ell^{\pm}$
- $\Sigma^{0} \to Z\nu_{\ell}$
- $\Sigma^{\pm} \to H\ell^{\pm}$

- $\Sigma^0 \to H\nu_\ell$

Where ℓ represents e, μ or τ, an example Feynman diagram for a complete decay chain is shown in Fig. 5.2

In this search, we consider all 27 different production and decay processes resulting from the decays of each of the $\Sigma^0\Sigma^+$, $\Sigma^0\Sigma^-$ and $\Sigma^+\Sigma^-$ pairs to the nine different pairs of W, Z and H bosons. The branching fractions are mass dependent. Few examples of complete decay chains going to multileptons are,

- $\Sigma^\pm\Sigma^0 \to W^\pm\nu_\ell W^\pm\ell^\mp \to \ell^\pm\nu_\ell\nu_\ell\ell^\pm\nu_\ell\ell^\mp$
- $\Sigma^\pm\Sigma^0 \to W^\pm\nu_\ell Z\nu_\ell \to \ell^\pm\nu_\ell\ell^\pm\ell^\mp\nu_\ell$
- $\Sigma^\pm\Sigma^\mp \to H\ell^\pm W^\mp\nu_\ell \to \tau^+\tau^-\ell^\pm\nu_\ell$;

In the model used in this analysis [126], the $\Sigma^\pm$ and Σ^0 decays are prompt, and gauge invariance ensures that they are degenerate in mass at tree level. The branching fraction (B) of a heavy fermion to a lepton of flavor ℓ is proportional to $\frac{|V_\ell|^2}{(|V_e|^2+|V_\mu|^2+|V_\tau|^2)}$, where V_ℓ is the heavy-light fermion mixing angle. The production cross sections are calculated with NLO + NLL accuracy using the CTEQ6.6 and MSTW2008nlo90cl parton distribution functions (PDFs) [127, 128]. The branching fractions of heavy fermion pairs into the most relevant decay modes contributed by charged leptons are given in Fig 5.3. The signal model is based on the FeynRules Model file of reference [126]. It includes all the possible 27 decay modes for this model. Centrally produced signal MC samples by CMS Collaboration, as listed in Table 5.1 are utilized in this analysis. The events are generated using MadGraph5mc@nlov5.2.2 [129] using the NNPDF30_lo_as_0130_ nf_4 [130] parton density function and bosonic decays are handled through pythia8, which also handles hadronization [131].

A prior search conducted by the CMS Collaboration using 7 TeV data excluded heavy fermions with mass (m_Σ) below 179 GeV [132], probing a scenario where the branching fractions to all lepton flavors are equal (flavor-democratic scenario, $B_e = B_\mu = B_\tau$). Using 8 TeV data, the ATLAS Collaboration excluded m_Σ below 335 GeV probing a similar scenario, but assuming that the Σs decay only to the first two generations of leptons [133]. A most recent similar search in a democratic scenario by CMS collaboration with 2.3 fb^{-1} run-I data excludes heavy fermion pair production for type-III seesaw model of mass 440 GeV each [134].In this analysis, all values of B_ℓ for each flavor of ℓ are probed, subject to the constraint $Be + B\mu + B\tau = 1$ [51, 125].

Going from 8 TeV to 13 TeV, the signal cross section has increased by a factor of 3 for masses at the sensitivity limit between 700 and 900 GeV. Due to various analysis

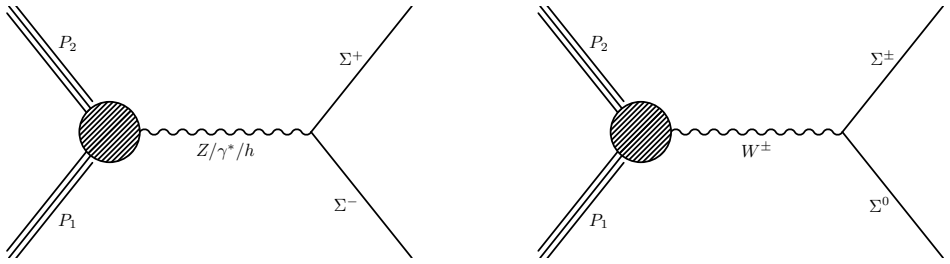

FIGURE 5.1: Examples of Feynman diagrams for heavy fermion production in the Type-III Seesaw model.

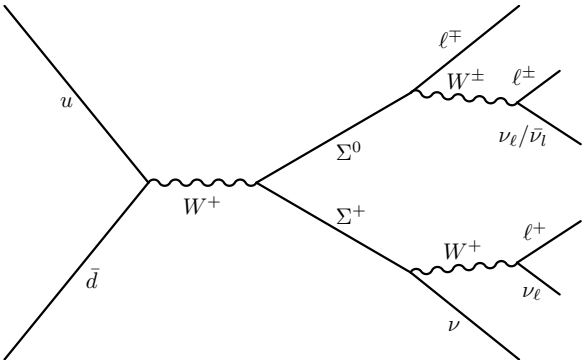

FIGURE 5.2: Feynman diagram example of the fermion production and decay in the Type-III Seesaw model.

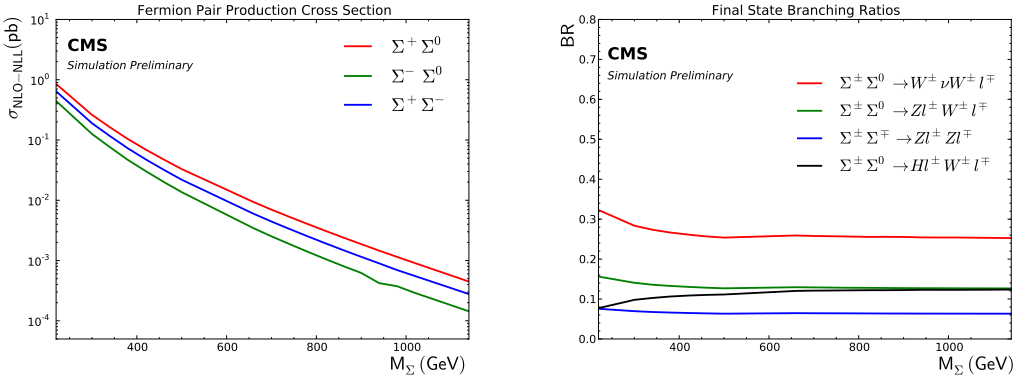

FIGURE 5.3: Production cross-sections in pp collisions at 13 TeV (left) and branching fractions of given pairs into the most relevant decay modes involving charged leptons (right) as a function of the degenerate heavy fermion mass.

TABLE 5.1: Seesaw signal MC samples and branching fractions (BRs). For all decay modes, charged and neutral Σ particles are considered to be mass-degenerate and are produced in 40 GeV steps in the range of 140-1300 GeV. The quoted BRs correspond to the scenario where Σ masses are much larger than those of the SM bosons ($\Sigma \gtrsim 700$ GeV).

Sample Name	BR
/SeesawTypeIII_SIGMAplusSIGMA0_M-*_13TeV-madgraph-pythia8/†	$\Sigma^+\Sigma^0 \to H\ell^+H\nu$: 5.7%
	$\Sigma^+\Sigma^0 \to H\ell^+W^\pm\ell^\mp$: 12.1%
	$\Sigma^+\Sigma^0 \to H\ell^+Z\nu$: 6.0%
	$\Sigma^+\Sigma^0 \to W^+\nu H\nu$: 12.1%
	$\Sigma^+\Sigma^0 \to W^+\nu W^\pm\ell^\mp$: 25.8%
	$\Sigma^+\Sigma^0 \to W^+\nu Z\nu$: 12.9%
	$\Sigma^+\Sigma^0 \to Z\ell^+H\nu$: 6.0%
	$\Sigma^+\Sigma^0 \to Z\ell^+W^\pm\ell^\mp$: 12.9%
	$\Sigma^+\Sigma^0 \to Z\ell^+Z\nu$: 6.4%
/SeesawTypeIII_SIGMAminusSIGMA0_M-*_13TeV-madgraph-pythia8/†	$\Sigma^-\Sigma^0 \to H\ell^-H\nu$: 5.7%
	$\Sigma^-\Sigma^0 \to H\ell^-W^\pm\ell^\mp$: 12.1%
	$\Sigma^-\Sigma^0 \to H\ell^-Z\nu$: 6.0%
	$\Sigma^-\Sigma^0 \to W^-\nu H\nu$: 12.1%
	$\Sigma^-\Sigma^0 \to W^-\nu W^\pm\ell^\mp$: 25.8%
	$\Sigma^-\Sigma^0 \to W^-\nu Z\nu$: 12.9%
	$\Sigma^-\Sigma^0 \to Z\ell^-H\nu$: 6.0%
	$\Sigma^-\Sigma^0 \to Z\ell^-W^\pm\ell^\mp$: 12.9%
	$\Sigma^-\Sigma^0 \to Z\ell^-Z\nu$: 6.4%
/SeesawTypeIII_SIGMAplusSIGMAminus_M-*_13TeV-madgraph-pythia8/†	$\Sigma^+\Sigma^- \to H\ell^+H\ell^-$: 5.7%
	$\Sigma^+\Sigma^- \to H\ell^+W^-\nu$: 12.1%
	$\Sigma^+\Sigma^- \to H\ell^+Z\ell^-$: 6.0%
	$\Sigma^+\Sigma^- \to W^+\nu H\ell^-$: 12.1%
	$\Sigma^+\Sigma^- \to W^+\nu W^-\nu$: 25.8%
	$\Sigma^+\Sigma^- \to W^+\nu Z\ell^-$: 12.9%
	$\Sigma^+\Sigma^- \to Z\ell^+H\ell^-$: 6.0%
	$\Sigma^+\Sigma^- \to Z\ell^+W^-\nu$: 12.9%
	$\Sigma^+\Sigma^- \to Z\ell^+Z\ell^-$: 6.4%

† RunIISummer16MiniAODv2-PUMoriond17_80X_mcRun2_asymptotic_2016_TrancheIV_v6-v1/MINIAODSIM

improvements which include all the decay modes, 4-lepton channels, an improved kinematic binning, and refined background methods, the sensitivity with the current 35.9 fb^{-1} data-set at 13 TeV is expected to exceed all the previous results.

The backgrounds for this search are the processes which produces final states with at least three charged leptons. Such backgrounds can be classified as the irreducible ones due to the production and decay of dibosons (WZ and ZZ production), and the reducible ones due to the leptonic decay of Z+jets or $\text{t}\bar{\text{t}}$+jets accompanied by leptons originating from heavy quark decay, or from misidentification of jets as leptons. In addition, small irreducible contributions to the background arise from other SM processes such as $\text{t}\bar{\text{t}}\text{W}$, $\text{t}\bar{\text{t}}\text{Z}$, triboson (ZZZ, WWZ etc.), and Higgs boson production.

The 2016 data collected by CMS with a combination of the unprescaled dilepton triggers are used for this analysis. The data samples and the dilepton triggers are listed in appendix A. The efficiency plots of dilepton triggers are given in appendix B. Other than triggers, data events are required to satisfy the filters recommended by the Jet-MET physics object group [135]. The data events collected during sub-optimal detector conditions are vetoed using the recommended Golden JSON file [62]. This

yields a final luminosity value of 35.9 fb^{-1}. All data samples have been processed in CMSSW_8_0_26_patch1. The global tag used is 80X_dataRun2_2016SeptRepro_v7 for eras 2016B-to-G, and 80X_dataRun2_Prompt_v16 for era 2016H.

5.1 Search Strategy

The general search strategy is based upon a multi-binned counting experiment. There are two primary search region(channels)that are considered. They are,

- Exactly 3 and 4 or more light lepton channels, light lepton denote an electron or muon here.
- 4 or more light lepton channels

The primary search regions are then further divided into non-overlapping regions based on invariant mass of dileptons representing Z-boson candidates, missing transverse momenta, jet momenta etc. The discriminators used are kinematic quantities such as sum of lepton pt (L_{T}), missing transverse momenta($p_{\text{T}}^{\text{miss}}$), and transverse mass ($M_{\text{T}}$). The background trimming so as to minimize other SM contribution and search regions for each primary channels are discussed further.

5.1.1 3 or more Light Lepton Channels

Candidate events in this search channel must have a total of at least three leptons, each of which can be either an electron or a muon. Multilepton events are further classified into non-overlapping search channels on the basis of the number of leptons, lepton flavor, lepton relative charges, charge and flavor combinations, and other kinematic quantities described below.

We classify each event in terms of the maximum number of opposite-sign same-flavor (OSSF) dilepton pairs that can be made by using each lepton only once. For example, both $\mu^+\mu^-\mu^-$ and $\mu^+\mu^-e^-$ are OSSF1, $\mu^+\mu^+e^-$ is OSSF0, and $\mu^+\mu^-e^+e^-$ is OSSF2. We denote a lepton pair of different flavors as $\ell\ell'$.

We classify events as containing a leptonically-decaying Z if at least one OSSF pair has a reconstructed invariant mass, $m_{\ell^+\ell^-}$ inside the Z mass window ($91 \pm 10\,\text{GeV}$), referred to as "on-Z". In this context ℓ represents either an electron or muon. For $m_{\ell^+\ell^-}$ outside the Z boson mass window, events are separated into bins below and above the Z mass window. In cases of ambiguity (such as $\mu^+\mu^-\mu^-$), the pair below the Z mass window

takes precedence (thus shifting events from high mass to low mass, for a more separative background categorization). We refer to these three mass ranges "as on-Z", "below-Z", and "above-Z".

The important multilepton background processes are WZ, ZZ production and Z or $t\bar{t}$ events in which there is an additional fake lepton. The term "fake" refers both to real leptons that arise from non-prompt decays (for instance: of hadrons) and to non-leptonic objects that are reconstructed as leptons, such as hadrons that reach the muon detectors, or hadronic showers with large electromagnetic energy fractions. It is intended to denote all objects reconstructed as leptons that arise neither from leptonic boson decays nor from the tau-decay. At times, the term misidentified is used synonymously. In addition, there are various rare background processes like WWZ or $t\bar{t}W$. However, the level of SM background varies considerably across channels; for example, channels containing OSSF pairs suffer from larger backgrounds than do channels with OSSF0. Hence, all these charge combinations are considered as different channels.

In order to enhance sensitivity to the new physics signal, it is important to reduce background contributions from the SM by applying basic object and event selection criteria. SM processes that are similar to the "signal" of interest contribute to the "background" of the search. These backgrounds can be reduced by binning in appropriate quantities. Given the relatively high signal lepton momenta due to the large masses of the parent particles, cutting on L_{T}, the scalar lepton p_{T} sum, may be a good idea. This is especially true for decay modes like $\Sigma^{\pm} \to \ell^{\pm}\mathrm{Z} \to \ell^{\pm}\ell'^{\pm}\ell'^{\mp}$ where the heavy fermion mass is transformed into the lepton momenta. To also obtain robust sensitivity across modes such as $\Sigma^0 \to \mathrm{H}\nu \to \mathrm{WW}\nu$, where neutrinos contribute to $p_{\mathrm{T}}^{\mathrm{miss}}$, the better choice is $L_{\mathrm{T}} + p_{\mathrm{T}}^{\mathrm{miss}}$.

For events with OSSF1 and on-Z, the sensitivity is improved by considering the transverse mass, $M_{\mathrm{T}} = (2p_{\mathrm{T}}^{\mathrm{miss}}p_{\mathrm{T}}^{\ell}(1 - \cos(\vec{p}_{\mathrm{T}}^{\mathrm{miss}}, \vec{p}_{\mathrm{T}}^{\ell})))^{1/2}$, using the lepton that is not part of the OSSF pair.

The optimum requirement on $L_{\mathrm{T}} + p_{\mathrm{T}}^{\mathrm{miss}}$ or M_{T} depends on the masses of the heavy fermions. To maximize the sensitivity across the expected mass range (700–900 GeV), we categorize the events in eight bins of $L_{\mathrm{T}} + p_{\mathrm{T}}^{\mathrm{miss}}$ or M_{T}, regardless the mass of the particles. A bin of width 150 (100) GeV for $L_{\mathrm{T}} + p_{\mathrm{T}}^{\mathrm{miss}}$ (M_{T}) is used, and in each case the highest bin includes overflow events.

To achieve accurate SM backgrounds, a very small amount of data has to be unblinded. This is typically a region where there are very less signal events and referred to as control region(CR). Any overlap with background CR's are removed explicitly vetoing the control region selections. Furthermore, we discard the below-Z trilepton region

TABLE 5.2: The signal regions used in the 3 light lepton search region, summarized in terms of the number of leptons, the presence of an OSSF pair, and the kinematic variable used for signal discrimination. Each selection described here is further divided into eight bins in the kinematic variable, giving a total of 48 statistically independent signal regions. Additional criteria based on $p_{\mathrm{T}}^{\mathrm{miss}}$ are used to ensure that signal regions are non overlapping with control regions.

N_{leptons}	Number of OSSF & mass	Kinematic variable	$p_{\mathrm{T}}^{\mathrm{miss}}$ requirement
3	on-Z	M_T	$p_{\mathrm{T}}^{\mathrm{miss}} > 100\,\mathrm{GeV}$
3	1 pair, above-Z	$L_{\mathrm{T}} + p_{\mathrm{T}}^{\mathrm{miss}}$	-
	1 pair, below-Z	$L_{\mathrm{T}} + p_{\mathrm{T}}^{\mathrm{miss}}$	$p_{\mathrm{T}}^{\mathrm{miss}} > 50\,\mathrm{GeV}$
	none	$L_{\mathrm{T}} + p_{\mathrm{T}}^{\mathrm{miss}}$	-
≥ 4	1 pair	$L_{\mathrm{T}} + p_{\mathrm{T}}^{\mathrm{miss}}$	-
	≥ 2 pairs	$L_{\mathrm{T}} + p_{\mathrm{T}}^{\mathrm{miss}}$	$p_{\mathrm{T}}^{\mathrm{miss}} > 50\,\mathrm{GeV}$ if on-Z

and the four-lepton region without an OSSF pair because, with the given amount of luminosity, they contain a negligible amount of signal and thus do not contribute to the sensitivity.

As a result for 3 or more light lepton search region, we have five $L_{\mathrm{T}} + p_{\mathrm{T}}^{\mathrm{miss}}$ and one M_{T} distribution, depending upon the lepton properties:

- 3 lepton without an OSSF pair (Distribution:$L_{\mathrm{T}} + p_{\mathrm{T}}^{\mathrm{miss}}$).
- 3 lepton with an OSSF pair "Above-Z" (Distribution:$L_{\mathrm{T}} + p_{\mathrm{T}}^{\mathrm{miss}}$).
- 3 lepton with an OSSF pair "Below-Z" (Distribution:$L_{\mathrm{T}} + p_{\mathrm{T}}^{\mathrm{miss}}$).
- 3 lepton with an OSSF pair "On-Z" (Distribution:M_{T}).
- 4 or more lepton with an OSSF pair "On-Z" (Distribution:$L_{\mathrm{T}} + p_{\mathrm{T}}^{\mathrm{miss}}$).
- 4 or more lepton with two OSSF pair "On-Z" (Distribution:$L_{\mathrm{T}} + p_{\mathrm{T}}^{\mathrm{miss}}$).

The resulting set of 48 exclusive bins for this search region is described in table 5.2.

5.2 Event Selection

The events are selected mainly in two categories, they are,

- Exactly three light leptons. Events with exactly three light leptons are selected. The offline p_{T} threshold for the three leading leptons is 25, 15, 10 GeV respectively. The events are then further divided into search regions mentioned in the previous section.

- Four or more light leptons. Events with at-least four leptons are selected, if the event has more than four leptons, the four leading one are considered for all the kinematic quantity calculations. The offline p_{T} threshold for the three leading leptons is 25, 15, 10, 10 GeV respectively.The events are then further divided into search regions mentioned in the previous section.

Other than above criteria, events with an opposite-sign lepton pair with mass below 12 GeV are vetoed to reduce back- ground from low-mass resonances. Furthermore, we reject trilepton events with an OSSF pair below the Z boson mass window when the trilepton mass is within the Z mass window. This cuts away background from asymmetric photon conversions in $\mathrm{Z} \to \ell\ell^* \to \ell\ell\gamma$, where the photon converts into two additional leptons, one of which is lost.

Chapter 6

Background Estimates

Multileptons search benefits from lesser backgrounds from SM. Nonetheless, there are processes which mimic multilepton signature, and some dilepton backgrounds also play upon the detector inadequacies to act as multilepton backgrounds. In this chapter, I will introduce and describe all the backgrounds that were estimated to compare with the data.

Within the framework of this search, leptons that directly come from W or Z boson decays (or from Σ particles in the context of the Seesaw signal) are considered as prompt leptons, whereas those originating from semi-leptonic heavy quark decays within jets or from other Misidentified detector signatures are labeled as misidentified (fake) leptons. Additionally, a smaller fraction of non-prompt leptons is due to internal or external asymmetric conversions of photons and such leptons are labeled as conversion leptons.

SM processes yielding three or more prompt leptons such as WZ and ZZ events, or those with two prompt and additional fake leptons such as Z + jets and $t\bar{t} + jets$ events constitute the primary backgrounds for this analysis. Various other processes such as triboson, $t\bar{t}V$, and top or vector boson associated Higgs production can also yield multilepton signatures. These contributions are suppressed due to lower production cross-sections and are collectively labeled as rare backgrounds.

The irreducible diboson backgrounds, WZ $\rightarrow 3\ell\nu$ and ZZ $\rightarrow 4\ell$, are estimated using MC samples that are normalized and validated in dedicated control regions in data, as mentioned in the previous chapter. The other irreducible rare or Higgs backgrounds are also obtained from MC samples but are normalized to the appropriate theoretical cross-sections. For all other backgrounds that contain misidentified or conversion leptons, data-driven methods are utilized. Although not targeted as a signal region within this analysis, dilepton event selections enriched in DY+jets and $t\bar{t} + jets$ processes are

used to verify the performance of simulated events with respect to data using the same lepton selection and trigger requirements. An overview of the control regions utilized in the background studies is provided in Table 6.2 and these background components are addressed below. Also, a comprehensive summary of all the backgrounds is provided in the Table 6.3.

6.0.1 Background MC samples

The MC samples listed in Table 6.1 are used for this analysis. These have been processed in CMSSW_8_0_26_patch1 with global tag 80X_mcRun2_asymptotic_2016_TrancheIV_v8. The diboson background samples (WZ, ZZ) are generated using POWHEG v2 [136, 137]. The triboson are generated using MADGRAPH 5 aMC@NLO v5.2.2 whereas Higgs backgrounds are generated using POWHEG v2 and JHU Generator v6.2.8 [138–141]. Bosonic decays, along with parton showering, fragmentation and hadronization for all samples is performed using PYTHIA 8.2 [142, 143]. For systematic studies, we also use simulation samples for Z and $t\bar{t}$ production generated using MADGRAPH 5 aMC@NLO v5.2.2.

The simulated events are re-weighted to match the distribution of in-time pileup interactions per bunch crossing to that of data following the recommendations of the Physics Validation Group [65]. However, the optimal minimum bias cross-section is observed to be 5% lower than the recommended value of 69.2 mb, and hence is assumed as the input to the pileup weight generator tool *pileupCalc.py*. Electron and muon ID and isolation efficiency scale factors are also applied to the MC events following the recommendations of the Muon and EGamma POGs. Although the dilepton trigger decisions are used in the event selections in MC, trigger efficiency scale factors are only applied to the MC samples in the dilepton control region in Section 6.2 as they make a negligible impact in the overall event yields in the relevant selections with 3 or more leptons.

6.1 A Note on the Uncertainties in the Backgrounds

No measurement or estimate is complete without an analysis of the various uncertainties through various sources. Concerning this analysis, the uncertainties can be broadly divided into two categories, statistical and systematic. Since most of the signal regions are limited by statistics and also due to the nature of the processes involved statistical uncertainty plays an essential role in the estimates of the background. Statistical uncertainties follows a Poisson distribution with mean λ and a standard deviation σ defined by

TABLE 6.1: Background MC samples.

Sample Name	Cross-section [pb]
/DYJetsToLL_M-50_TuneCUETP8M1_13TeV-madgraphMLM-pythia8/†_ext1-v2/‡	5765.4
/DY1JetsToLL_M-50_TuneCUETP8M1_13TeV-madgraphMLM-pythia8/†-v1/‡	1016×1.54527
/DY2JetsToLL_M-50_TuneCUETP8M1_13TeV-madgraphMLM-pythia8/†-v1/‡	331.4×1.54527
/DY3JetsToLL_M-50_TuneCUETP8M1_13TeV-madgraphMLM-pythia8/†-v1/‡	96.36×1.54527
/DY4JetsToLL_M-50_TuneCUETP8M1_13TeV-madgraphMLM-pythia8/†-v1/‡	51.40×1.54527
/TTJets_DiLept_TuneCUETP8M1_13TeV-madgraphMLM-pythia8/†-v1/‡	87.31
/TTJets_DiLept_TuneCUETP8M1_13TeV-madgraphMLM-pythia8/†_ext1-v1/‡	87.31
/WWTo2L2Nu_13TeV-powheg/†-v1/‡	12.178
/WZTo3LNu_TuneCUETP8M1_13TeV-powheg-pythia8/†-v1/‡	4.42965
/WZTo3LNu_TuneCUETP8M1_13TeV-amcatnloFXFX-pythia8/†-v1/‡ (cross-check)	4.712
/ZZTo4L_13TeV_powheg_pythia8/†-v1/‡	1.256
/WWW_4F_TuneCUETP8M1_13TeV-amcatnlo-pythia8/†-v1/‡	0.2086
/WWZ_TuneCUETP8M1_13TeV-amcatnlo-pythia8/†-v1/‡	0.1651
/WZZ_TuneCUETP8M1_13TeV-amcatnlo-pythia8/†-v1/‡	0.05565
/ZZZ_TuneCUETP8M1_13TeV-amcatnlo-pythia8/†-v1/‡	0.01398
/TTZToLLNuNu_M-10_TuneCUETP8M1_13TeV-amcatnlo-pythia8/†_ext1-v1/‡	0.2529
/TTWJetsToLNu_TuneCUETP8M1_13TeV-amcatnloFXFX-madspin-pythia8/†_ext1-v3/‡	0.2043
/TTTT_TuneCUETP8M2T4_13TeV-amcatnlo-pythia8/†-v1/‡	0.009103
/ttH_HToZZ_4LFilter_M125_13TeV_powheg2_JHUgenV6_pythia8/†-v1/‡	0.000337
/GluGluHToZZTo4L_M125_13TeV_powheg2_JHUgenV6_pythia8/†-v1/‡	0.01212
/VBF_HToZZTo4L_M125_13TeV_powheg2_JHUgenV6_pythia8/†-v1/‡	0.001034
/WminusH_HToZZTo4L_M125_13TeV_powheg2-minlo-HWJ_JHUgenV6_pythia8/†-v1/‡	0.0001471
/WplusH_HToZZTo4L_M125_13TeV_powheg2-minlo-HWJ_JHUgenV6_pythia8/†-v1/‡	0.0002339
/ZH_HToZZ_4LFilter_M125_13TeV_powheg2-minlo-HZJ_JHUgenV6_pythia8/†-v1/‡	0.000652

† RunIISummer16MiniAODv2-PUMoriond17_80X_mcRun2_asymptotic_2016_TrancheIV_v6
‡ MINIAODSIM

TABLE 6.2: Background control regions and the corresponding selection criteria. S_{T} is the scalar sum of the lepton transverse momenta(L_{T}), the transverse momenta of jets(H_{T}), and $p_{\mathrm{T}}^{\mathrm{miss}}$

	N_{leptons}	Lepton Pair condition	Kinematic cuts
DY+jets	2	On-Z	$p_{\mathrm{T}}^{\mathrm{miss}} < 50\,\mathrm{GeV}$
$\mathrm{t\bar{t}}$+jets	2	OSOF	$S_{\mathrm{T}} > 300\,\mathrm{GeV}$
Fake leptons	3(Light Leptons)	On-Z	$p_{\mathrm{T}}^{\mathrm{miss}} < 50\,\mathrm{GeV}$
Fake leptons	3(L2T1)	OS/SS	$p_{\mathrm{T}}^{\mathrm{miss}} < 50\,\mathrm{GeV}$
Conversions leptons	3	below-Z, trilepton on-Z	$p_{\mathrm{T}}^{\mathrm{miss}} < 50\,\mathrm{GeV}$
WZ	3	On-Z	$50 < p_{\mathrm{T}}^{\mathrm{miss}} < 100\,\mathrm{GeV}$, $M_{\mathrm{T}} > 30\,\mathrm{GeV}$
ZZ	4	2 pairs, both on-Z	$p_{\mathrm{T}}^{\mathrm{miss}} < 50\,\mathrm{GeV}$

$$\sigma = \sqrt{N} \tag{6.1}$$

where N is the number of events in a counting experiment.

Background estimates are also affected by systematic uncertainties which arise independently through imperfect modeling of the observable's and unavoidable biases on the measurements. The systematic uncertainties through various sources are described in detail in the subsequent section. Both the uncertainties(statistical and systematic) are added quadratically to find the total uncertainty on different background estimates.

TABLE 6.3: A rough classification of the multilepton backgrounds sources, the contributing leading SM processes and their estimation methods.

Background Source	Leading processes	Estimation Method	Notes
Irreducible	WZ, ZZ	MC	Normalized in 3L/4L CRs
Misidentified (from jets etc.)	$t\bar{t}$, DY, WW	Data driven (Matrix method)	Developed in low $p_T^{miss}(< 50)$ 2L/3L CRs for light leptons and low $p_T^{miss}(< 50)$ OS/SS region for L2T1 with i/p from MC
Photon Conversion	$t\bar{t}$, DY, WW	Data Driven (Photon Proxy Method)	Developed in low $p_T^{miss}(< 50)$ 2L/3L CRs, Not estimated for L2T1 search region

6.2 Dilepton Control Regions

Although the corresponding MC samples are not used in the signal regions, dileptonic DY + jets and $t\bar{t}$+jets processes have been studied as a cross-check to commission and verify the object selections used in the analysis. A set of dilepton events enriched in DY($\rightarrow$ ee)+jets and DY($\rightarrow$ $\mu\mu$)+jets processes are created using the DoubleEG and DoubleMuon datasets respectively, where the dilepton opposite sign same flavor mass(MOSSF) is required to be on-Z, and $p_T^{miss} < 50\,GeV$. For a selection enriched in $t\bar{t}$+jets, the MuonEG data-set is used where events are required to have an opposite-sign eμ pair and $S_T > 300\,GeV$. In each of these three selections, the dominant DY + jets or $t\bar{t}$+jets contribution is normalized to the overall data yield, and jet multiplicity dependent weights are derived to account for possible higher order effects as LO MadGraph+Pythia8 samples are used. The normalization scale factors are calculated to be 1.05, 1.02, and 0.96 for the $DY \rightarrow$ ee, $DY \rightarrow \mu\mu$, and $t\bar{t} \rightarrow e\mu$ selections, respectively, concerning the NNLO cross-sections of these processes. Figures 6.1, 6.2 and 6.3 show the lepton p_T, H_T, and L_T distributions for the DY + jets enriched selections, and the lepton p_T, S_T, and p_T^{miss} distributions for the $t\bar{t}$+jets enriched selection, where a good overall data-MC agreement is observed in all these kinematic quantities.

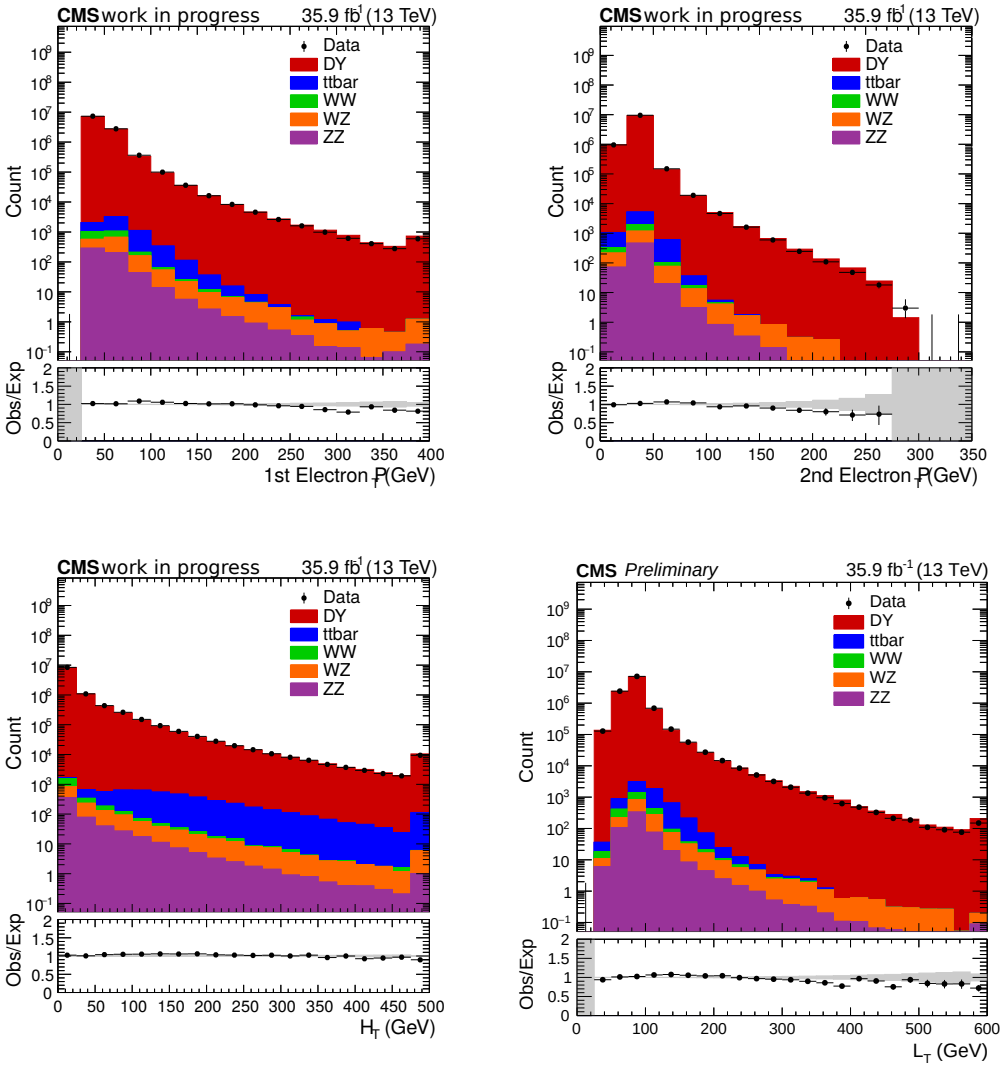

FIGURE 6.1: Leading (upper left) and sub-leading (upper right) electron p_{T}, H_{T} (lower left) and L_{T} (lower right) distributions in the DY→ee enriched dilepton selection (last bin includes overflow). Uncertainty bands in the ratio plot in the lower panel include statistical uncertainties only.

6.3 Irreducible Backgrounds

The irreducible backgrounds are those which are estimated directly from dedicated simulation samples. As described in chapter 3, we rely on POWHEG or MADGRAPH 5 aMC@NLO generators to obtain MC simulation for these processes, the further details can be found in that chapter.The prompt diboson backgrounds(WZ, ZZ) which are estimated from simulation are normalized and validated in data control regions, as described in Table 6.2. The background due to rare processes like $t\bar{t}Z$, $t\bar{t}W$ and some Higgs processes are directly obtained from simulation. No normalization or validation is done on the "Rare" backgrounds, as they contribute very less in comparison to overall

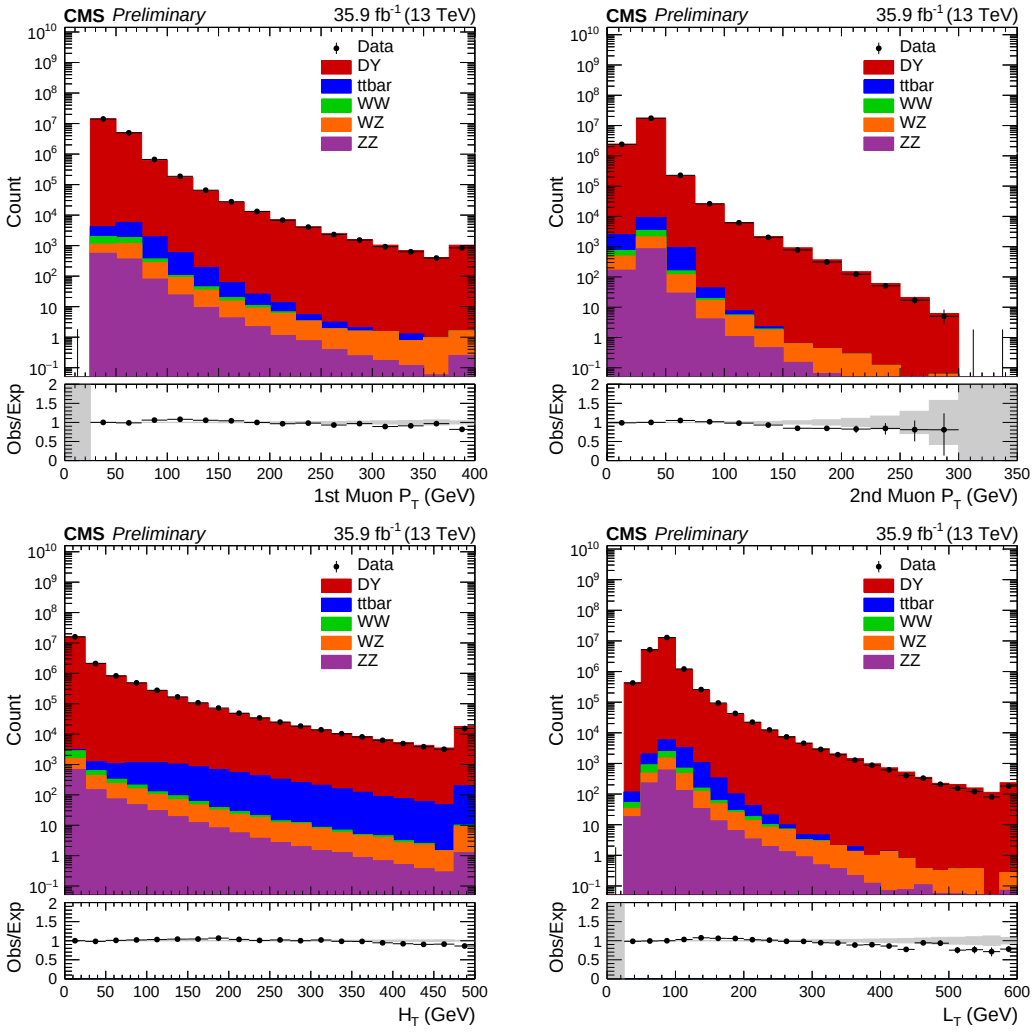

FIGURE 6.2: Leading (upper left) and sub-leading (upper right) muon p_{T}, H_{T} (lower left) and L_{T} (lower right) distributions in the DY$\rightarrow \mu\mu$ enriched dilepton selection (last bin includes overflow). Uncertainty bands in the ratio plot in the lower panel include statistical uncertainties only.

backgrounds. Instead a systematic uncertainty (50%) is put on their overall crossection. These processes are collectively referred as "Rare" in the figures. I shall now describe the irreducible backgrounds in detail.

6.3.1 WZ Background

The WZ$\rightarrow 3\ell\nu$ process constitutes one of the major backgrounds in this analysis, and a Powheg generated NLO MC sample is used to estimate these contributions. A WZ$\rightarrow 3\ell\nu$ enriched ($\gtrsim$ 70%) selection of events is created by requiring exactly 3 leptons with an on-Z OSSF pair, $50\,\mathrm{GeV} < E_{\mathrm{T}}^{\mathrm{miss}} < 100\,\mathrm{GeV}$, and $M_{\mathrm{T}} > 30$ GeV. The WZ MC normalization scale factor over the NLO cross-section is then calculated as the ratio of

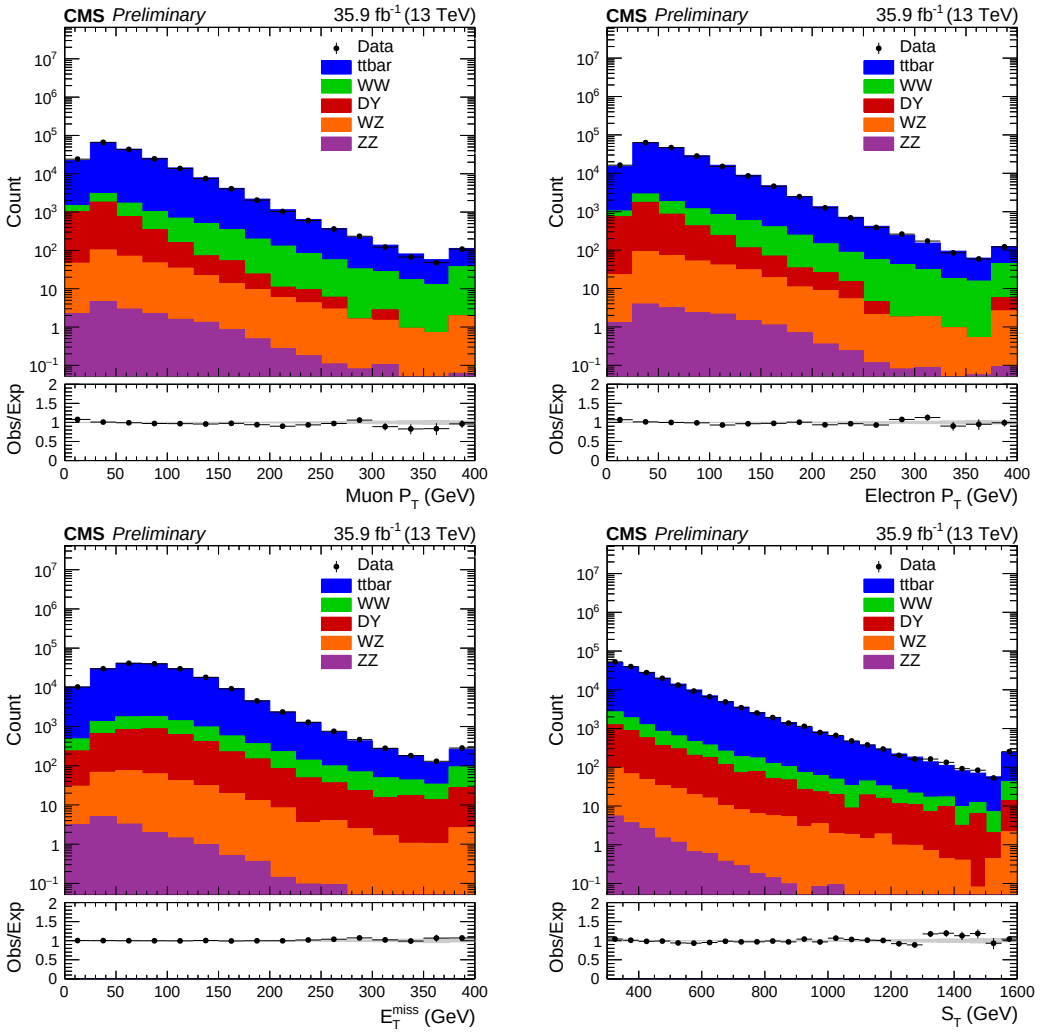

FIGURE 6.3: Muon p_{T} (upper left), electron p_{T} (upper right), $E_{\mathrm{T}}^{\mathrm{miss}}$ (lower left) and S_{T} (lower right) distributions in the $t\bar{t} \to \mathrm{e}\mu$ enriched dilepton selection (last bin includes overflow). Uncertainty bands in the ratio plot in the lower panel include statistical uncertainties only.

non-WZ subtracted data events over WZ MC events, yielding a value of 1.15 ± 0.08 (statistical and systematic), and this normalization correction factor is applied to all WZ MC events. This leads to a relative normalization uncertainty of 7%.

The corresponding M_{T}, L_{T}, H_{T}, $E_{\mathrm{T}}^{\mathrm{miss}}$, primary vertex multiplicity, and muon multiplicity distributions are provided in Figure 6.4, where good data-MC agreement is observed. Background contributions due to misidentified or conversion leptons are estimated via the data driven processes discussed in Sections 6.4 and 6.5.

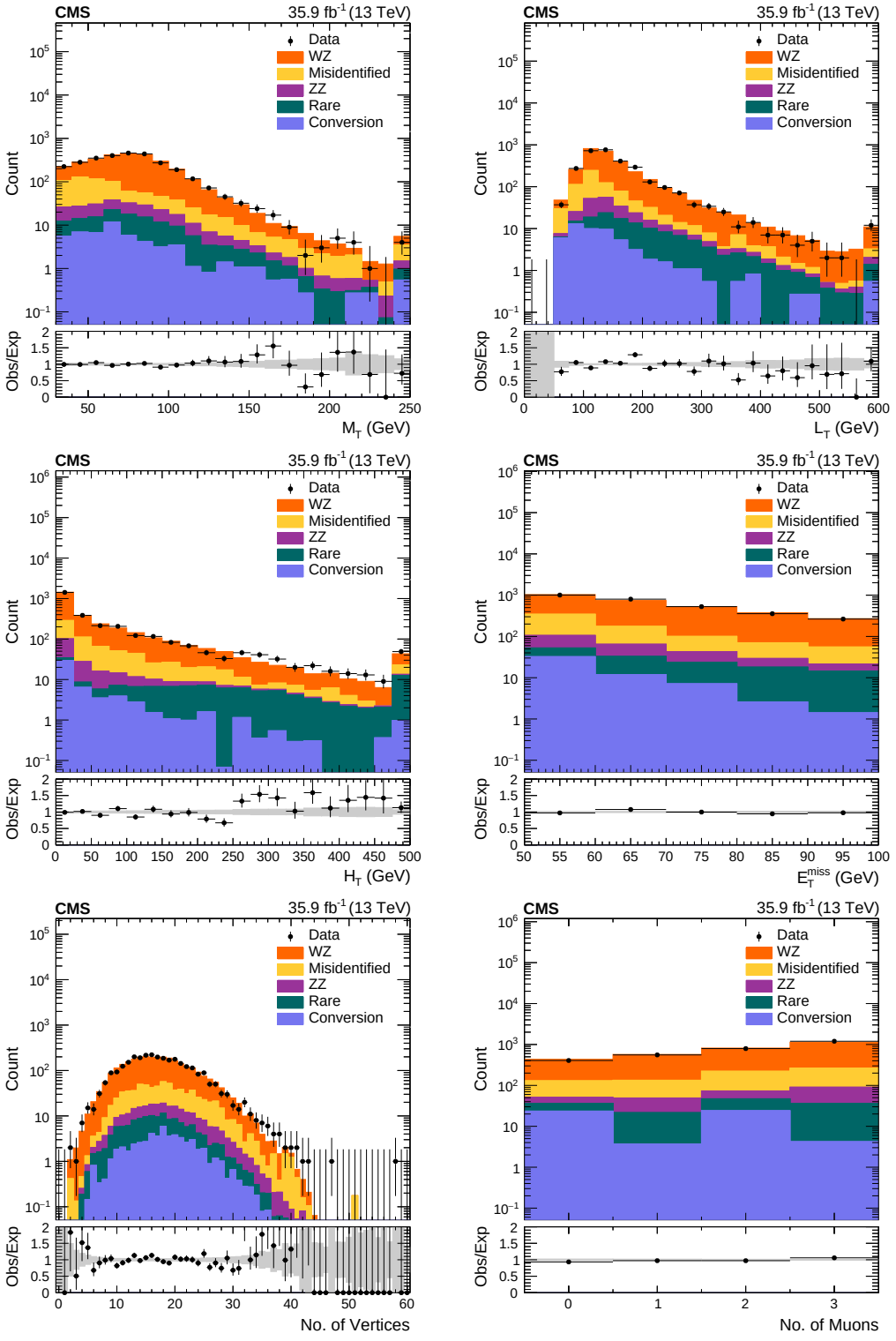

FIGURE 6.4: M_{T} (upper left), L_{T} (upper right), H_{T} (center left), $E_{\mathrm{T}}^{\mathrm{miss}}$ (center right), primary vertex multiplicity (lower left), and muon multiplicity (lower right) distributions in the WZ-dominated selection of events (last bin includes overflow). Uncertainty bands in the ratio plots in the lower panel include statistical uncertainties only.

6.3.2 ZZ Background

While the ZZ background is responsible for only 5% of the background in the ten channels with highest overall sensitivity, its contribution is more than 95% in the 4-lepton regions. The ZZ $\rightarrow 4\ell$ background dominates ≥ 4 lepton signal regions with an at least one on-Z OSSF pair. Similar to the WZ background, ZZ contributions are also estimated using a Powheg generated NLO MC sample that is normalized to data in a dedicated ZZ-enriched selection of events. This selection is defined by requiring exactly 4 leptons that form 2 distinct on-Z OSSF pairs and $E_{\mathrm{T}}^{\mathrm{miss}} < 50\,\mathrm{GeV}$, and yields a set of events $\gtrsim 99\%$ pure in ZZ $\rightarrow 4\ell$. The ZZ MC normalization scale factor over the NLO cross-section is calculated as the ratio of non-ZZ subtracted data events over ZZ MC events, yielding a value of 1.25 ± 0.06 (statistical and systematic) and 5% relative uncertainty.

For the ZZ enriched selection, H_{T}, L_{T}, $E_{\mathrm{T}}^{\mathrm{miss}}$, primary vertex multiplicity, M(4ℓ), and muon multiplicity distributions are provided in Fig. 6.5. A good data-MC agreement is observed in all distributions.

6.3.3 Rare Backgrounds

Contributions due to rare (triboson, $\mathrm{t\bar{t}V}$) and Higgs (e.g. VH, $\mathrm{t\bar{t}H}$) processes comes under this category. These processes are estimated using Powheg or aMC@NLO generated NLO MC samples and are normalized by the appropriate NLO theoretical cross-sections.

6.4 Misidentified Lepton Backgrounds

Multilepton background contributions due to fake leptons, such as in DY+jets and tt +jets events, are estimated via data-driven techniques. A data-driven technique uses non-over-lapping part of the data from search regions, to provide estimates in search regions. The data-driven method used here is known as the matrix method [144] and it estimates misidentified lepton backgrounds.

The matrix method is implemented differently for three or more light lepton regions(Hereafter termed as 3LL) and L2T1 region, but the underlying principle for both region is same. I will discuss the method and both the implementation in detail in the subsequent sections.

6.4.1 Matrix Method

In its simplest form, matrix method is a data-driven background estimation technique which relies on the assumption that the probabilities with which prompt and fake leptons

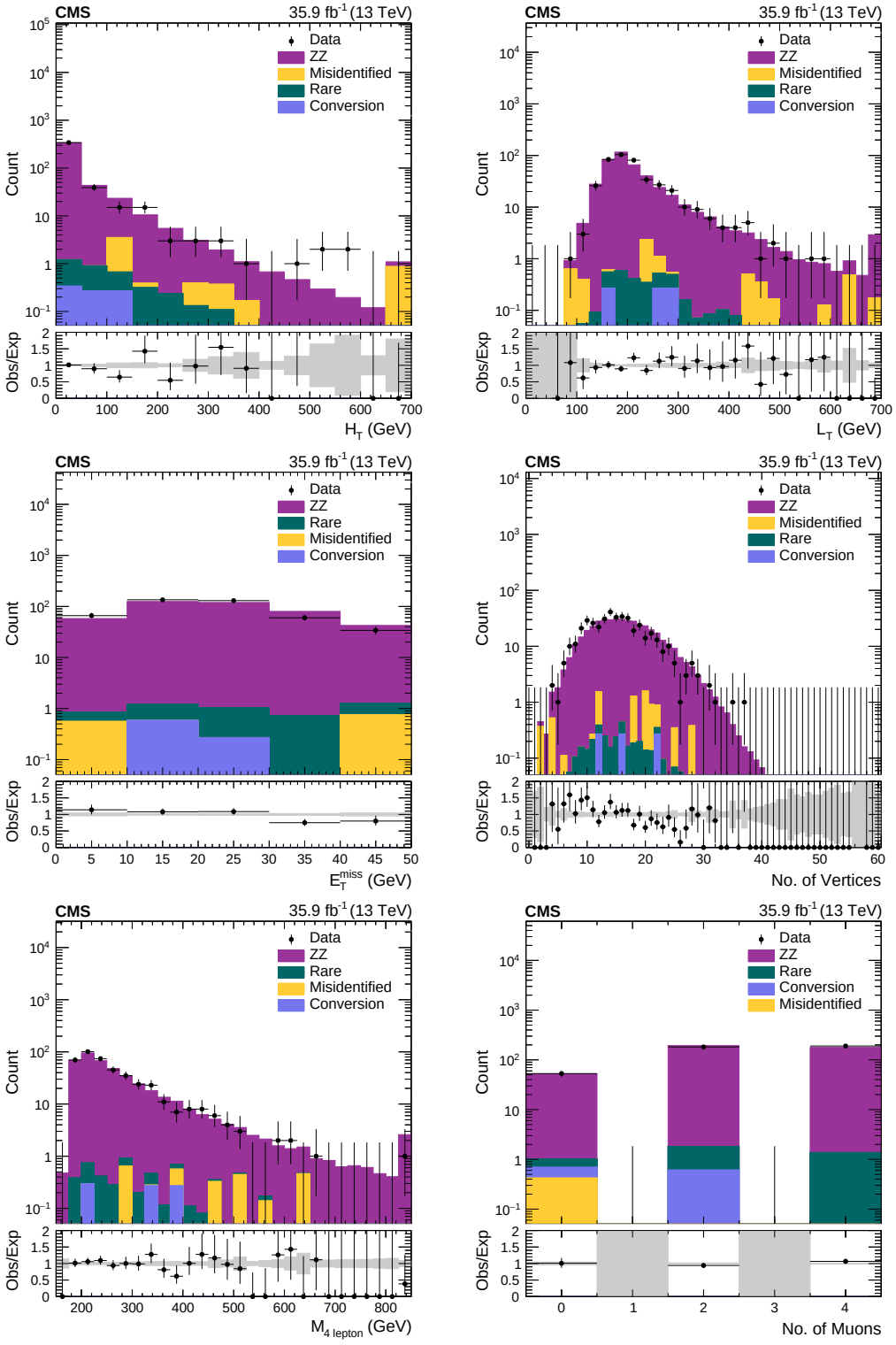

FIGURE 6.5: The H_{T} (upper left), L_{T} (upper right), $E_{\mathrm{T}}^{\mathrm{miss}}$ (center left), primary vertex multiplicity (center right), M(4ℓ) (lower left), and muon multiplicity (lower right) distributions in the ZZ enriched selection of events. All plots include the ZZ cross-section normalization correction. The last bins include overflow events. The uncertainty bands in the ratio plots include statistical uncertainties only.

pass a tight lepton selection given that they satisfy a loose lepton selection, prompt(p) and fake(f) rates respectively, are universal. The prompt(p) and fake(f) can be described as a function of the lepton and event dependent parameters. This assumption allows the measurement of these rates in signal-depleted control regions and then their application to a signal region.

This description of the 2D matrix method is based on the Ref. [145], which estimates fakes given a single tight lepton. This method can be trivially expanded for the 3-lepton case. In its 3-dimensional form, the matrix method can predict background contributions due to events with up to 3 simultaneous misidentified leptons. In signal regions with 4 or more leptons, the 3D matrix method is applied on the 2^{nd}, 3^{rd}, and 4^{th} leading p_{T} leptons, and the leading p_{T} lepton is assumed to be prompt. For a given set of selection requirements(such as 3LL but here with a single tight lepton), four combinations are defined based on the selection quality of the chosen same-sign dilepton pair. Events in which both leptons satisfy the tight selection requirements are classified as TT events, whereas those with both leptons failing the tight selection while satisfying the loose selection requirements are classified as LL events. Similarly, events with only one lepton candidate satisfying the tight selection and with the other lepton satisfying the loose selection but failing the tight selection requirements are labeled as TL or LT events. The TT combination constitute the signal region, whereas TL, LT, and TT combinations are used for the estimation of backgrounds.

These events can also be categorized on the basis of true lepton origins, forming the double-fake, double-prompt and single-fake combinations, denoted as FF, PP, PF and FP, respectively. These two categorizations are represented in Fig. 6.6 with the corresponding number of events in each combination, such that $N_{\text{LL}} + N_{\text{LT}} + N_{\text{TL}} + N_{\text{TT}} = N_{\text{FF}} + N_{\text{FP}} + N_{\text{PF}} + N_{\text{PP}}$. The matrix method provides a handle in estimating the sizes of these origin-based subsets that are of actual interest to the analysis, by using the selection- based subsets that can be measured.

The selection based combination(loose-tight) can be related to the origin-based subsets(prompt-fake) with the multiplication by transformation matrix represented by Eq 6.2 where $\widehat{f}_i = 1 - f_i$ and $\widehat{p}_i = 1 - p_i$. The subscripts refer to lepton-1 and lepton-2 as used in Fig 6.6.

$$\begin{pmatrix} N_{\text{LL}} \\ N_{\text{LT}} \\ N_{\text{TL}} \\ N_{\text{TT}} \end{pmatrix} = \begin{pmatrix} \widehat{f}_1.\widehat{f}_2 & \widehat{f}_1.\widehat{p}_2 & \widehat{p}_1.\widehat{f}_2 & \widehat{p}_1.\widehat{p}_2 \\ \widehat{f}_1.f_2 & \widehat{f}_1.p_2 & \widehat{p}_1.f_2 & \widehat{p}_1.p_2 \\ f_1.\widehat{f}_2 & f_1.\widehat{p}_2 & p_1.\widehat{f}_2 & p_1.\widehat{p}_2 \\ f_1.f_2 & f_1.p_2 & p_1.f_2 & p_1.p_2 \end{pmatrix} \begin{pmatrix} N_{\text{FF}} \\ N_{\text{FP}} \\ N_{\text{PF}} \\ N_{\text{PP}} \end{pmatrix} \tag{6.2}$$

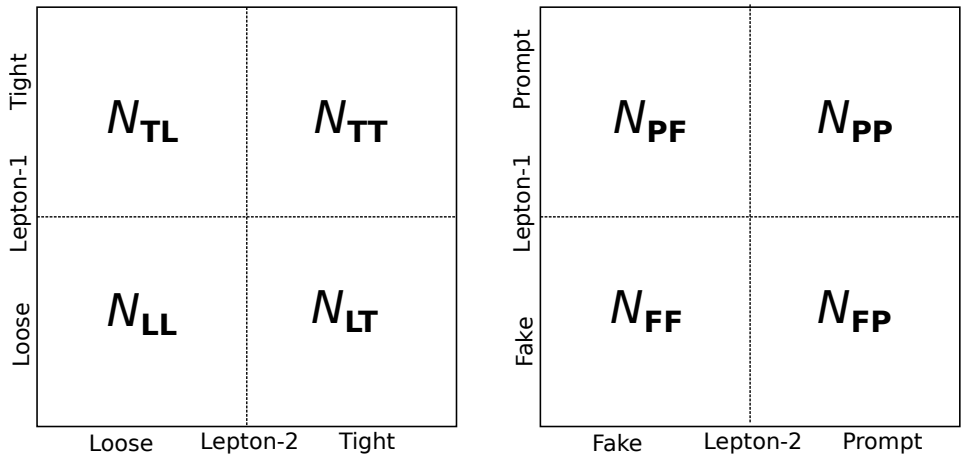

FIGURE 6.6: The selection based combination (left) and origin-based subsets (right) of the dilepton pair.

Assuming $f_i \neq p_i$, this transformation matrix can be inverted for the calculation of origin-based contributions solely based on the experimentally measurable quantities as presented in Eq. 6.3 The total number of events with fake leptons in the TT combination is the sum of single- and double-fake contributions, and can be expressed as in Eq. 6.4 where $N_{\mathrm{FF}}, N_{\mathrm{FP}}$, and N_{PF} are derived quantities.

$$\begin{pmatrix} N_{\mathrm{FF}} \\ N_{\mathrm{FP}} \\ N_{\mathrm{PF}} \\ N_{\mathrm{PP}} \end{pmatrix} = \frac{1}{(p1-f1)(p2-f2)} \begin{pmatrix} p_1.p_2 & -p_1\widehat{p_2} & -\widehat{p_1}.P_2 & \widehat{p_1}.\widehat{p_2} \\ -p_1.f_2 & p_1.\widehat{f_2} & \widehat{p_1}.f_2 & -\widehat{p_1}.\widehat{f_2} \\ -f_1.p_2 & f_1.\widehat{p_2} & \widehat{f_1}.p_2 & -\widehat{f_1}.\widehat{p_2} \\ f_1.f_2 & -f_1.\widehat{f_2} & -\widehat{f_1}.f_2 & \widehat{f_1}.\widehat{f_2} \end{pmatrix} \begin{pmatrix} N_{\mathrm{LL}} \\ N_{\mathrm{LT}} \\ N_{\mathrm{TL}} \\ N_{\mathrm{TT}} \end{pmatrix} \tag{6.3}$$

$$N_{TT}^{\mathrm{FakeBkg.}} = f_1 f_2 N_{\mathrm{FF}} + f_1 p_2 N_{\mathrm{FP}} + p_1 f_2 N_{\mathrm{PF}} \tag{6.4}$$

If the prompt and fake probabilities assume constant values, Eqs. 6.3 and 6.4 can be used in their present form for the estimation of fake lepton containing backgrounds given the $p_i$and f_i measurements as well as the distribution of events in the selection- based categorization. Equivalently, these can be read as a recipe for applying individual weights to each selected event based on its selection-based classification and as a function of the properties of the dilepton pair (such as p_{T} and η) chosen for the matrix method in order to calculate the event's contribution to single- and double-fake lepton categories. Since

the prompt and fake probabilities for the leptons of interest are found to be variables, the latter approach is adopted in this analysis.

6.4.2 Determination of Prompt and Fake Rates for Leptons

Prompt rates for leptons are measured using a tag-and-probe(T&P) method. A set of events enriched in prompt leptons from $Z \to \ell\ell$ decays is created by requiring an on-Z, OSSF dilepton pair satisfying the loose lepton selections with no additional loose leptons and $E_{\mathrm{T}}^{\mathrm{miss}} < 50$ GeV. The leading p_{T} lepton is chosen as the tag and is required to also satisfy the tight lepton selection. The sub-leading p_{T} lepton is chosen as the probe. This T&P method for measuring lepton prompt rates is only applied in the data. In simulated samples, generator level information is used where the reconstructed leptons are required to be kinematically matched to a generator level prompt lepton ($\Delta\mathrm{R} < 0.2$) in order to be labeled as probe objects.

Lepton fake rates are also measured in on-Z events but in a subset of those where a third lepton is present that is assumed to originate from a jet or other hadronic activity. These events are required to have an on-Z, OSSF pair satisfying the tight lepton selection, $E_{\mathrm{T}}^{\mathrm{miss}} < 50$ GeV, and a single additional probe lepton satisfying the loose lepton selection. In order to suppress contamination due to events with conversion leptons, the on-Z mass selection is tightened such that MOSSF is required to be within 3 GeV of the Z boson mass and M(3ℓ) is required to be above-Z (following the usual 10 GeV window around the Z boson mass). A fake probe lepton enriched selection of events is created in simulated samples by imposing an inverted ΔR requirement among the probe lepton and the prompt generator level leptons in the event ($\Delta\mathrm{R} > 0.2$). Additionally, fake probe leptons matching to a generator level photon are also vetoed.

The prompt (fake) rate is then defined as the ratio of prompt (fake) probe lepton enriched events as described above where the probe lepton further satisfies the tight lepton selection over those it satisfies the loose lepton selection, such that events in the numerator constitute a subset of those in the denominator. In all rate measurements conducted in data, contributions due to leptons of the undesired origin (prompt leptons for fake rate measurements and vice verse) are estimated and subtracted using MC methods, whereas a simple binomial ratio of tight over loose leptons is taken in MC. These quantities are calculated as given in Eq. 6.5.

$$
\begin{aligned}
p^{\text{data}} &= \frac{\text{N}^{\text{data}}_{\text{tight}} - \text{N}^{\text{MC}}_{\text{tight non-prompts}}}{\text{N}^{\text{data}}_{\text{loose}} - \text{N}^{\text{MC}}_{\text{loose non-prompts}}}, \qquad p^{\text{MC}} = \frac{\text{N}^{\text{MC}}_{\text{tight prompts}}}{\text{N}^{\text{MC}}_{\text{loose prompts}}}, \\
f^{\text{data}} &= \frac{\text{N}^{\text{data}}_{\text{tight}} - \text{N}^{\text{MC}}_{\text{tight non-fakes}}}{\text{N}^{\text{data}}_{\text{loose}} - \text{N}^{\text{MC}}_{\text{loose non-fakes}}}, \qquad f^{\text{MC}} = \frac{\text{N}^{\text{MC}}_{\text{tight fakes}}}{\text{N}^{\text{MC}}_{\text{loose fakes}}}.
\end{aligned}
\tag{6.5}
$$

The prompt rates are parametrized in bins of the lepton p_{T} (5 bins), whereas fake rates are parametrized in bins of lepton p_{T} (3 bins), lepton $|\eta|$ (4 bins), particle multiplicity of the AK4 PF jet of which the lepton is a constituent (2 bins), and the leading lepton p_{T} in the event (2 bins). The leading lepton p_{T} binning is found to be relevant only for the muon fake rate measurements. For electrons binning in leading lepton p_{T} is not observed to significantly change the fake rates with respect to the inclusive measurements due to the tighter ID and isolation requirements. A pile-up dependent correction factor, k_{pu}, defined as the relative change in the inclusive fake rate as a function of primary vertices, is separately measured for and applied to the fake rates of both lepton flavors.

All electron and muon prompt and fake rate measurements performed in DY enriched data, in simulated DY+jets and $\text{t}\bar{\text{t}}$ +jets events, the corresponding data-MC prompt and fake rate correction factors, and the pile-up dependent correction factors for fake rates are presented in Fig. 6.7, 6.8, 6.9, and 6.10. The electron and muon prompt rates are measured to be $\gtrsim 75\%$ ($\gtrsim 85\%$ for electrons with $p_{\text{T}} > 20$ GeV) and $\gtrsim 90\%$, respectively, whereas the fake rates vary in the range of 10-35% for both lepton flavors. In bins with sufficient data events, the MC based prompt and fake rates are generally observed to be consistent with the data measurements within 1% and 20%, respectively, and the data-MC correction factor relative uncertainties are $\lesssim 15\%$.

Taking into account the comparison of the rates measured in DY enriched data events and the simulated DY events as well as the variation of the rates in simulated DY and $\text{t}\bar{\text{t}}$ events, a single prompt and fake rate is defined for each bin as given in Eq. 6.6.

$$
\begin{aligned}
p &= \frac{p^{\text{DY Data}}}{p^{\text{DY MC}}} \cdot \frac{p^{\text{DY MC}} + p^{\text{t}\bar{\text{t}}\text{ MC}}}{2} \\
f &= \frac{f^{\text{DY Data}}}{f^{\text{DY MC}}} \cdot \frac{f^{\text{DY MC}} + f^{\text{t}\bar{\text{t}}\text{ MC}}}{2} \cdot k_{pu}.
\end{aligned}
\tag{6.6}
$$

The DY and $\text{t}\bar{\text{t}}$ samples are specifically chosen as they constitute the major background processes with fake leptons in this analysis, and yet differ significantly in terms of event hadronicity and kinematics. The loose and tight lepton selections as well as the fake rate parametrizations (such as the lepton-jet particle multiplicity and the leading lepton p_{T})

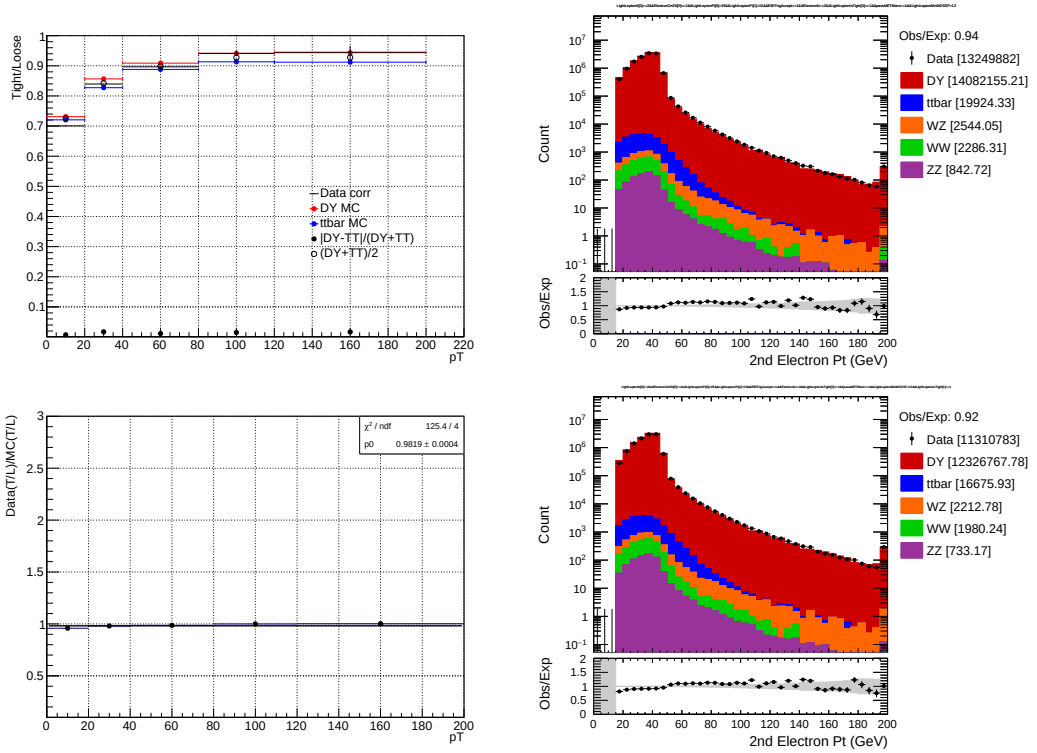

FIGURE 6.7: Electron prompt rates (upper left) in DY enriched data, and in simulated DY+jets and $t\bar{t}$ +jets events, as well as the data-MC correction factors (lower left) measured as a function of the electron p_T. A linear fit (pol-0) is used to extract the overall data-MC prompt rate correction factor, and this value is used to modify the MC based electron prompt rates. The electron prompt rate measurement in the DY enriched data selection is carried out using the ratio of the tight (lower right) over loose (upper right) electron p_T distributions, where non-prompt contributions are subtracted but are found to be negligible.

are chosen to minimize the process dependent (DY vs $t\bar{t}$) variations of the lepton fake rates, and the observed residual process dependence, 5-20% for fake rates and $< 5\%$ for prompt rates in both flavors, is then considered as a source of systematic uncertainty.

In addition, the fake rate measurements in each of the DY and $t\bar{t}$ MC samples are observed to also depend on the flavor-p_T order of the trilepton event from which the fake lepton comes (for example eee vs $\mu\mu e$ events where the fake electron can be the leading, sub-leading or sub-subleading p_T object), as given in Fig. 6.12. These internal variations can be primarily understood as correlations between the fake lepton and the neighboring prompt lepton quantities such as p_T and isolation, and are observed to be mostly contained within 15-20% of the mean rates. For each given bin, the larger of these internal and inter-process (DY vs $t\bar{t}$) uncertainties is assigned as the MC-based systematic uncertainty(statistical uncertainties in MC based measurements are negligible in comparison), and these are in the range of 15-25%. Combined with the data-MC rate

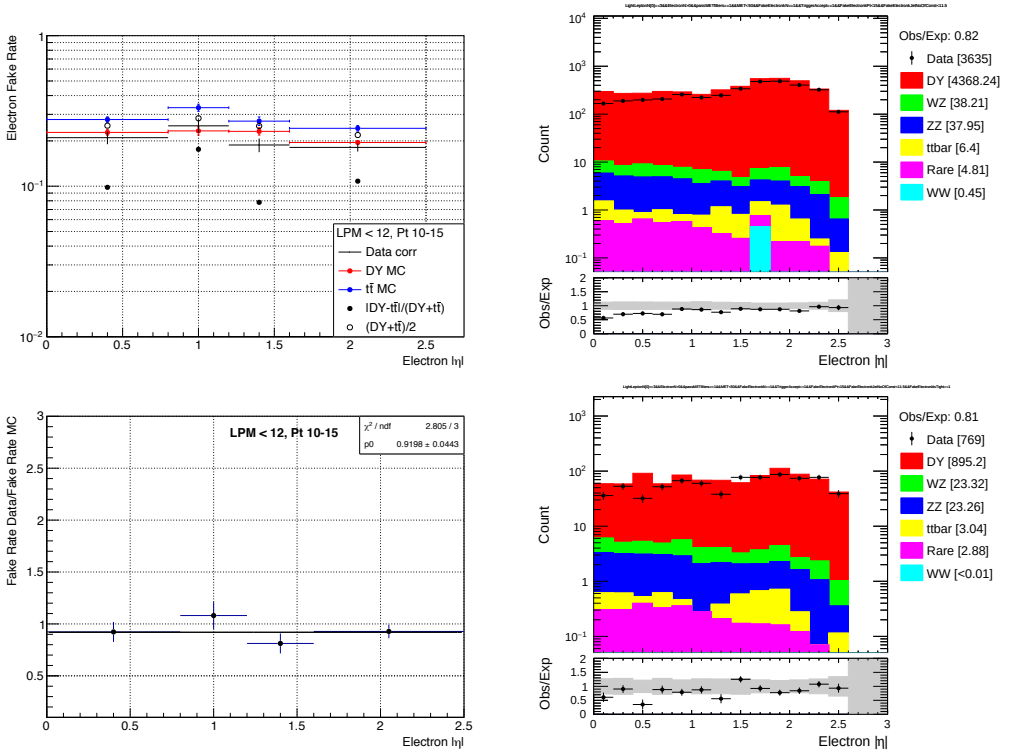

FIGURE 6.8: Electron fake rates (upper left) in DY enriched data, and in simulated DY+jets and $t\bar{t}$ +jets events, as well as the data-MC correction factors (lower left) measured as a function of the electron $|\eta|$, for electrons with $10 < p_T < 15$ GeV and electron-jet particle multiplicity < 12. A linear fit (pol-0) is used to extract the overall data-MC fake rate correction factor, and this value is used to modify the MC based electron fake rates in these $|\eta|$ bins. The electron fake rate measurement in the DY enriched data selection is carried out using the ratio of the tight (lower right) over loose (upper right) electron $|\eta|$ distributions, where non-fake contributions are subtracted. Conservative 30% and 50% uncertainties are assigned to the normalization of WZ/ZZ and rare background components, respectively.

correction factor uncertainties, the overall relative uncertainties on the prompt and fake rates are then calculated to be $< 5\%$ and 20-25%, respectively, for both lepton flavors.

The individual simulation based prompt and fake rates are verified in closure tests performed in the simulated DY+jets and $t\bar{t}$ +jets samples where at least one fake lepton is required as a part of event selection. Figure 6.13 shows that the observed and the estimated number of events are in good agreement across all bins within the uncertainty bands, which are estimated by independently varying the muon and electron fake rates within their respective uncertainties solely due to the internal, flavor-p_T order dependent variations as discussed above (15-20% in magnitude). It is observed that only one of the electron or muon fake rate variations substantially affect ($> 5\%$) the mean value of the expected misidentified backgrounds in any given flavor combination due to the likely scenario that only a single fake lepton of a single flavor dominates at any one given bin, and these variations are calculated to be approximately 20% flat in all bins.

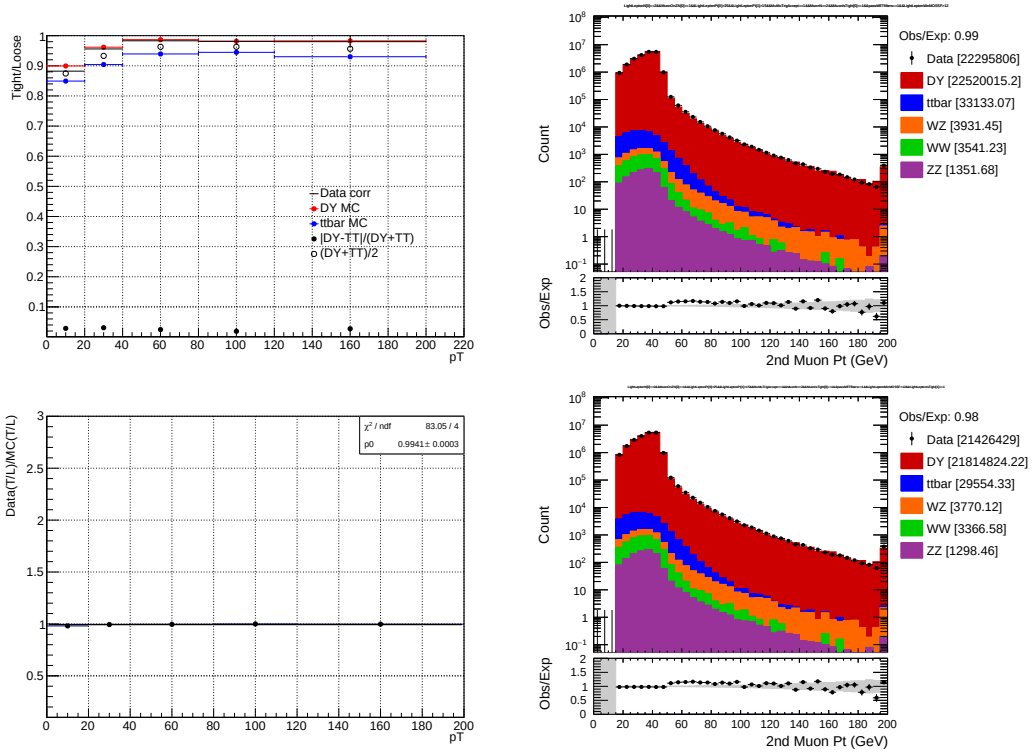

FIGURE 6.9: Muon prompt rates (upper left) in DY enriched data, and in simulated DY+jets and $t\bar{t}$ +jets events, as well as the data-MC correction factors (lower left) measured as a function of the muon p_{T}. A linear fit (pol-0) is used to extract the overall data-MC prompt rate correction factor, and this value is used to modify the MC based muon prompt rates. The muon prompt rate measurement in the DY enriched data selection is carried out using the ratio of the tight (lower right) over loose (upper right) muon p_{T} distributions, where non-prompt contributions are subtracted but are found to be negligible.

Similarly, the uncertainties on misidentified lepton backgrounds in the signal regions in data are estimated by independently varying the muon and electron prompt and fake rates taking into account all systematic and statistical uncertainties discussed above. The up and down variations on the prompt rates are observed to have a negligible ($< 1\%$) impact on the total background yields. The fake rate variations of 20-25% in magnitude result in qualitatively similar behavior as the above discussed MC closure plots, such that either the electron or muon fake rate variation dominates in a given bin. The relative variations of the matrix method estimate in each of the trilepton signal regions as a function of L_{T} $+E_{\mathrm{T}}^{\mathrm{miss}}$ or M_{T} are presented in Figures 6.14 and 6.15, and are found to be $\lesssim 30\%$ in magnitude across all bins considered in the signal regions. Hence, a flat 30% uncertainty is assigned on the misidentified lepton backgrounds.

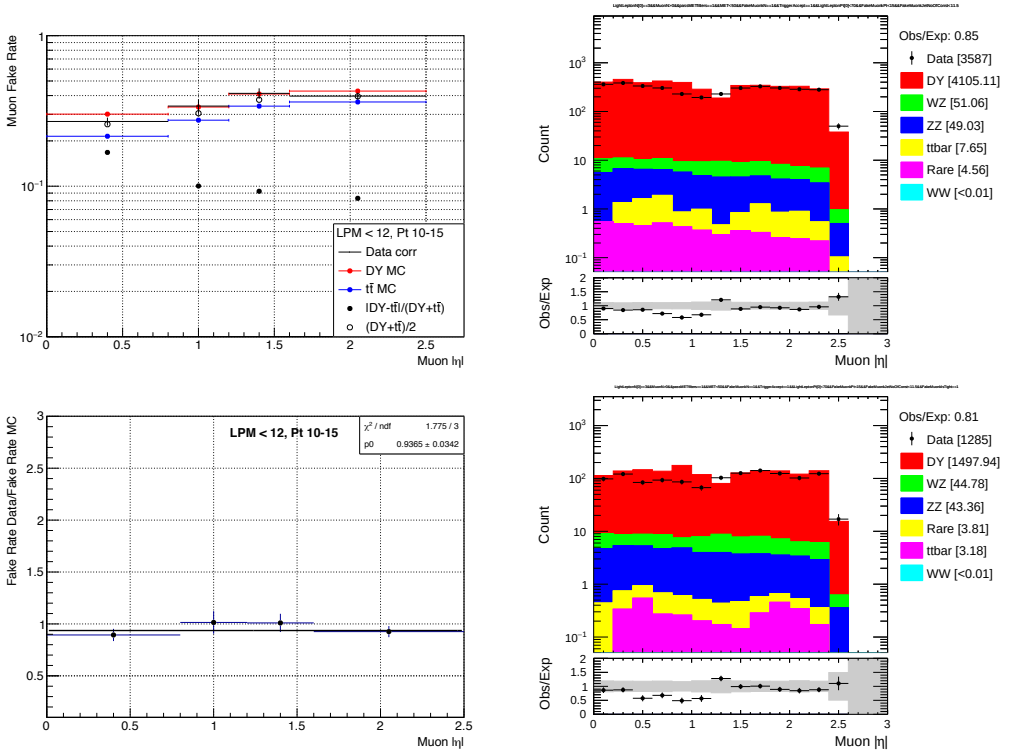

FIGURE 6.10: Muon fake rates (upper left) in DY enriched data, and in simulated DY+jets and $t\bar{t}$ +jets events, as well as the data-MC correction factors (lower left) measured as a function of the muon $|\eta|$, for muons with $10 < p_T < 15$ GeV and muon-jet particle multiplicity < 12 in events with leading lepton $p_T < 70$ GeV. A linear fit (pol-0) is used to extract the overall data-MC fake rate correction factor, and this value is used to modify the MC based muon fake rates in these $|\eta|$ bins. The muon fake rate measurement in the DY enriched data selection is carried out using the ratio of the tight (lower right) over loose (upper right) muon $|\eta|$ distributions, where non-fake contributions are subtracted. Conservative 30% and 50% uncertainties are assigned to the normalization of WZ/ZZ and rare background components, respectively.

6.5 Photon Conversion Backgrounds

As leptons from internal and external photon conversions may not be accurately modeled in simulated samples, we employ a data-driven method to estimate backgrounds due to processes where a conversion lepton assists an otherwise 2 (or 3) prompt lepton event to satisfy the 3 (or 4) lepton selection requirements. It must be noted that these type of background contributions constitute $\lesssim 5\%$ of the total expected backgrounds in the signal regions.

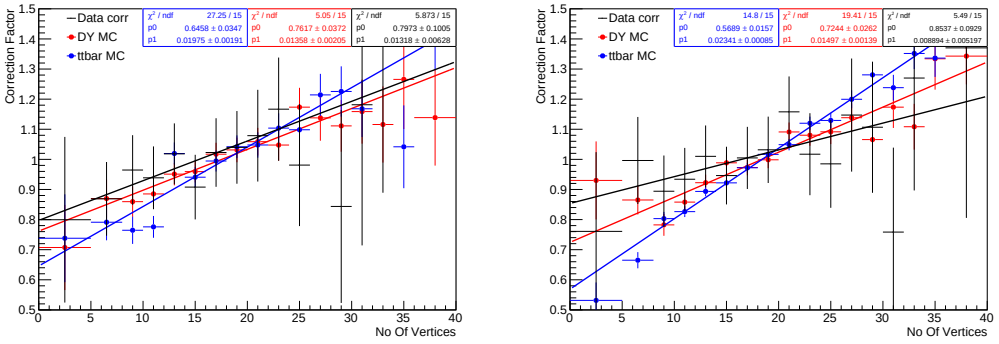

FIGURE 6.11: Electron and Muon fake rate correction factors as measured in DY enriched data (black), and in simulated DY+jets (red) and $t\bar{t}$ +jets (blue) events as a function of the primary vertex multiplicity (pile-up) in the event. This correction factor, k_{pu}, is defined as the relative change in the inclusive fake rate as a function of primary vertices, and it is applied via a first order polynomial fit to each of these selection of events. Since the data based measurement is found to be consistent with the DY MC based measurement within the fit uncertainties ($\sim 10\%$), the data based measurement with no MC corrections is used in the matrix method.

6.5.1 Photon Proxy Method

On-shell photons that are emitted similarly in the decay chain (by vector bosons, leptons, and quarks) but are detected and identified as photons (without undergoing any conversion process) by the CMS detector are used to determine the backgrounds due to conversions of photons into electrons or muons.

The internal conversion process favors off-shell photon masses at very low values, and the resulting kinematic distribution in this region of phase space is hence very similar to the emission of an on-shell photon [146]. Similarly, external conversions yielding a pair of distinct electrons are also likely to be detected and labeled as such by the electron reconstruction and identification algorithms except when the conversion process is highly asymmetric and one of the electrons is lost. Therefore, in both of these internal and external conversions, a significant fraction of the mother photon momentum is expected to be carried away by a single conversion lepton.

As photons that do not yield conversion leptons are expected to be kinematically similar to those that do, they can be treated as proxy objects and are used to estimate the conversion lepton background via a transfer factor, the so-called photon conversion rate. The internal asymmetric conversions can produce all lepton flavors in roughly equal proportions, whereas external conversions are expected to yield mostly electron candidates.

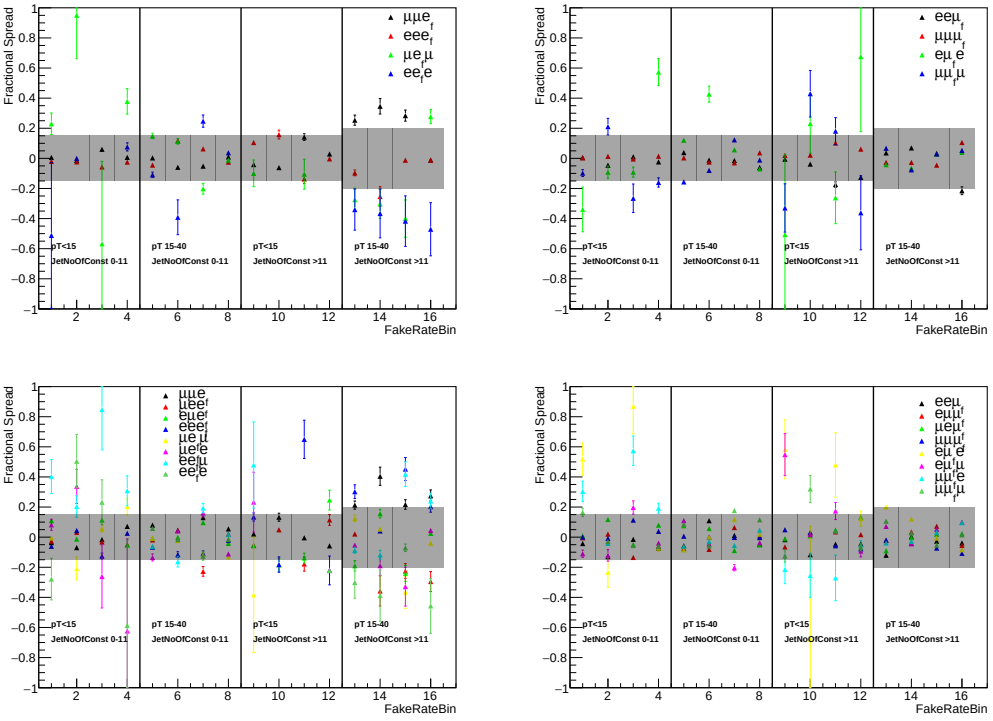

FIGURE 6.12: Flavor-p_{T} order dependent systematics on the electron (left) and muon (right) fake rates as measured in simulated DY+jets (upper) and $\mathrm{t\bar{t}}$ +jets (lower) events. In each plot, the enumerated labels on the x-axis represent different bins used in the parametrization of fake rates (such that each set of 4 consecutive bins correspond to a set of 4 $|\eta|$ bins as presented in Appendix D) and the y-axis is the fractional change of the fake rate at a given flavor-p_{T} order scenario (as indicated in the legend, subscript f indicated the fake lepton) with respect to the inclusive fake rate in that bin. The gray bands represent the uncertainties assigned to the inclusive fake rates to account for these variations in each region (15-20%). These internal uncertainties mostly become relevant for the matrix method in the limit that process dependent (DY vs $\mathrm{t\bar{t}}$) variations on the fake rates become negligible, and therefore are utilized as minimum lower bounds on the MC based fake rate systematic uncertainties.

Each proxy photon object is randomly assigned a lepton flavor and an electric charge such that each such event is counted only once for the purposes of the photon proxy method. The assignment of positive or negative charges is done with equal proportions, but the flavor assignment is set to yield twice as many electrons as muons to produce a higher statistical precision for the more dominant electron conversion backgrounds.

Conversion leptons can be best observed in the leptonic decays of Z bosons where an on- or off-shell photon emitted by one of the outgoing lepton daughters further converts asymmetrically into muon or electron pairs. In a significant fraction of such events, the softer p_{T} partner of the conversion lepton pair is lost, and the process yields a trilepton signature whose invariant mass is consistent with that of the Z boson. Hence, assuming universality of photon asymmetric conversions, the photon conversion rate

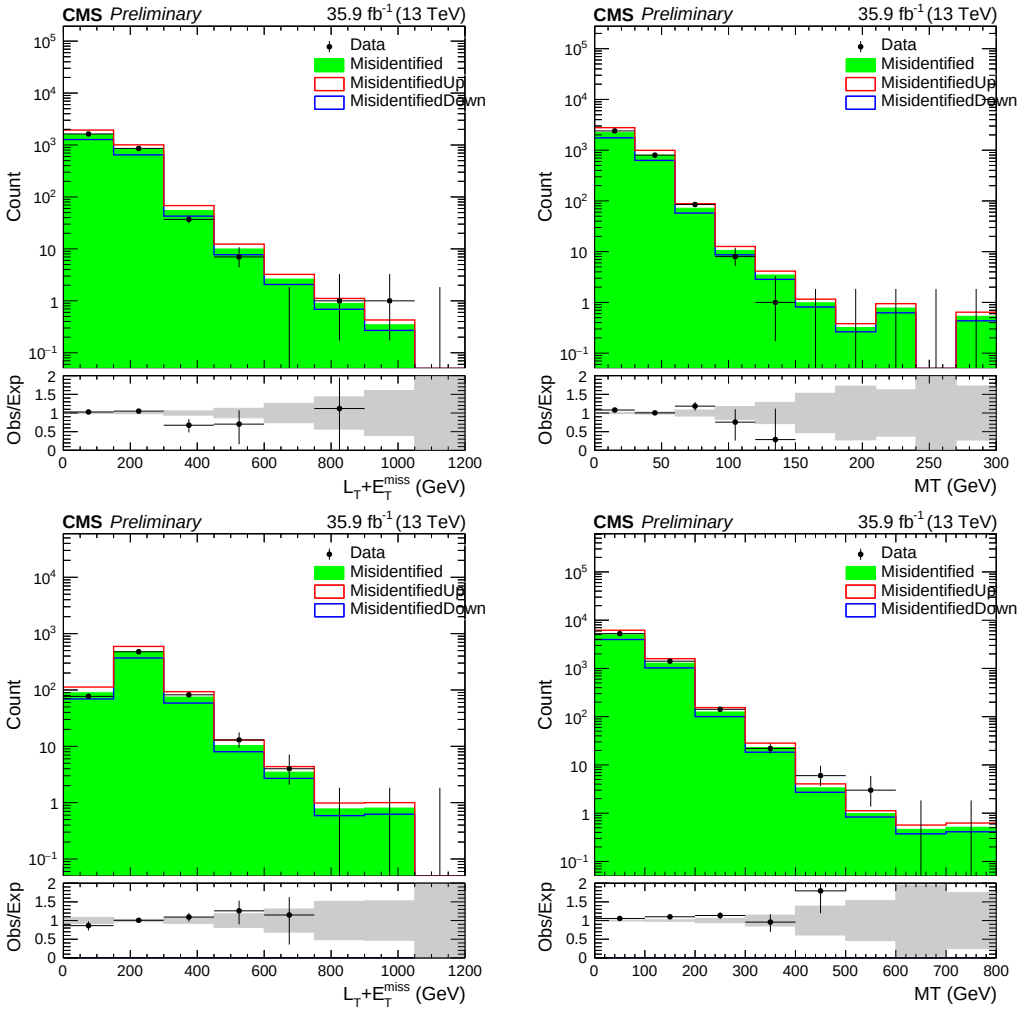

FIGURE 6.13: MC closure tests in simulated DY+jets and $t\bar{t}$ +jets where at least one fake lepton is required as a part of event selection and DY or $t\bar{t}$ MC based prompt and fake rates are used accordingly. L_T $+E_T^{miss}$ distributions in simulated DY+jets events in $\mu\mu e$ (upper left) and in simulated $t\bar{t}$ +jets events in eee (lower left) selections, and M_T distributions in simulated DY+jets events in eeμ (upper right) and in simulated $t\bar{t}$ +jets events in $\mu\mu\mu$ (lower right) selections, where "Data" entries represent the observed MC events in all plots. The up-down bands on the mean misidentified background estimate in each bin correspond to the variations of the electron (left) and muon (right) fake rates within their respective uncertainties solely due to the internal, flavor-p_T order dependent variations, and are found to be $\sim 20\%$ in magnitude. A good agreement is observed in all distributions between the expected and observed number of events within the uncertainties.

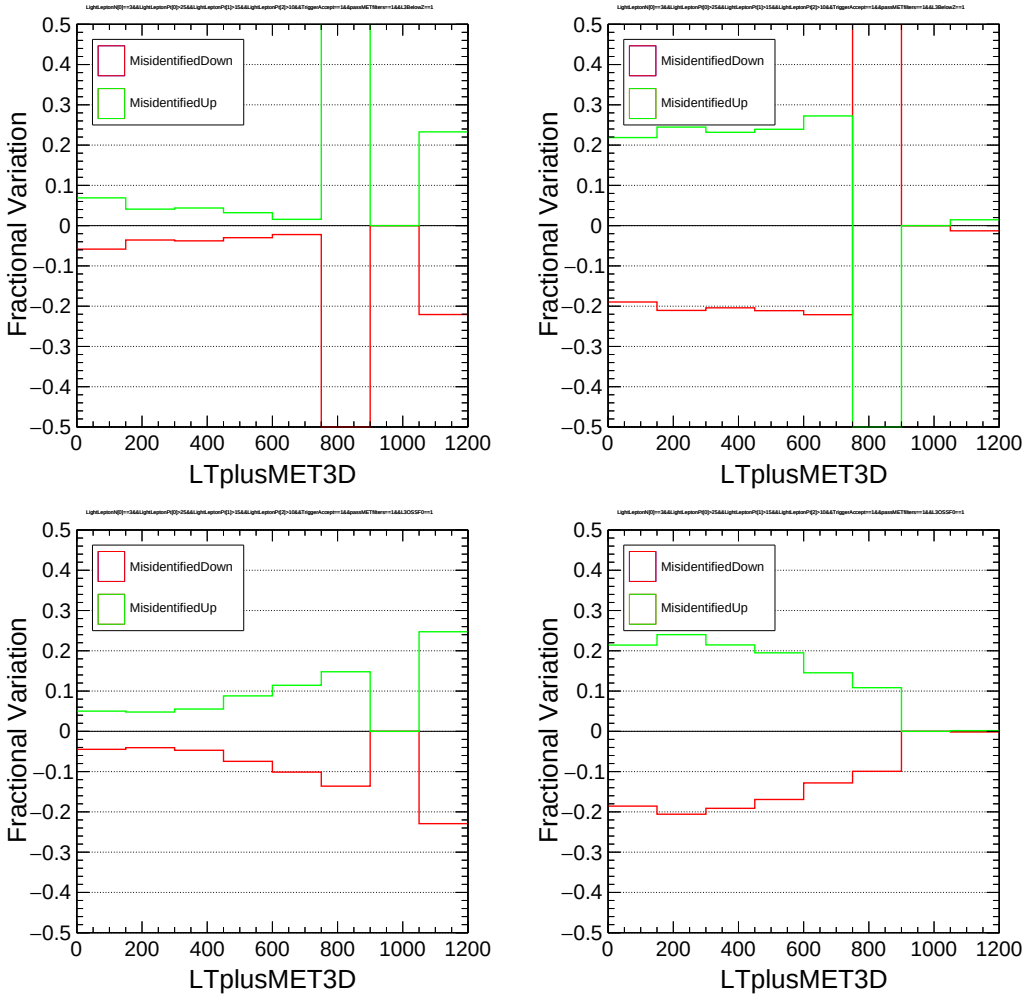

FIGURE 6.14: The relative variations of the misidentified lepton background estimate in data events in below-Z (upper) and OSSF0 (lower) trilepton signal regions as a function of $L_{\mathrm{T}} + E_{\mathrm{T}}^{\mathrm{miss}}$. The up-down bands on the mean misidentified lepton background correspond to the independent variations of the electron (left) and muon (right) fake rates within their total respective uncertainties. Bins with variations greater than 30% correspond to those where the misidentified lepton background estimate is less than 0.1 event.

can be measured as the ratio of 3ℓ events with M(3ℓ) within a defined Z mass window over $2\ell + \gamma$ events with M($2\ell + \gamma$) within the Z mass window and M(2ℓ) below the Z mass window. These quantities need to be corrected for non-Z contributions both in the numerator and the denominator, and the photon conversion rate can then be expressed as given in Eq. 6.7.

$$r_{\mathrm{conversion}} = \frac{\mathrm{N}_{3\ell} - \mathrm{N}_{\mathrm{MC\ prompt}} - \mathrm{N}_{\mathrm{Misidentified}}}{\mathrm{N}_{2\ell+\gamma}} \tag{6.7}$$

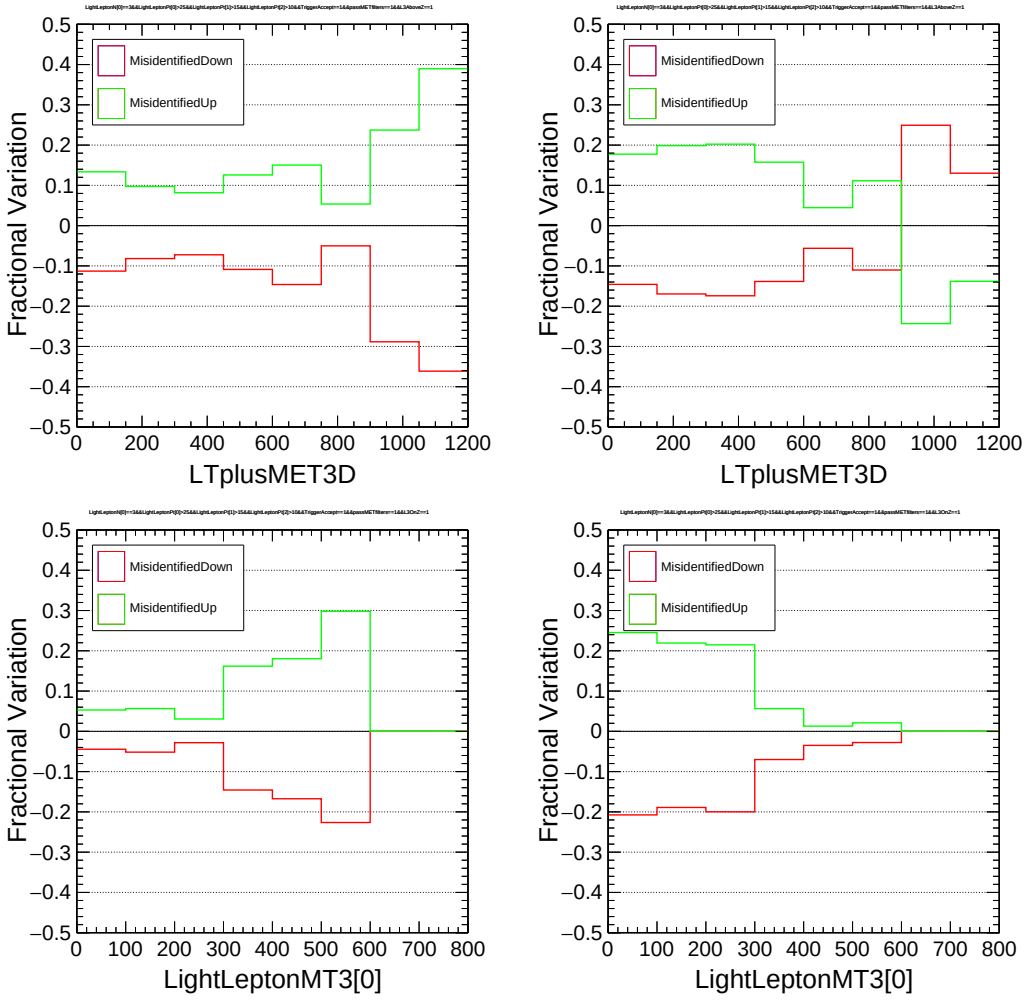

FIGURE 6.15: The relative variations of the misidentified lepton background estimate in data events in above-Z (upper) and on-Z (lower) trilepton signal regions as a function of L_{T} $+E_{\mathrm{T}}^{\mathrm{miss}}$, and and M_{T}, respectively. The up-down bands on the mean misidentified lepton background correspond to the independent variations of the electron (left) and muon (right) fake rates within their total respective uncertainties. Bins with variations greater than 30% correspond to those where the mean misidentified lepton background estimate is less than 0.1 event.

6.5.2 Measurement and Closure Tests of Photon to Electron/Muon Conversion Rates

Events that have an OSSF pair below-Z ($\mathrm{M}(2\ell) < 81\,\mathrm{GeV}$) with $E_{\mathrm{T}}^{\mathrm{miss}} < 50\,\mathrm{GeV}$, and either a third electron or muon (or a photon) such that the invariant mass of the three-object system, $\mathrm{M}(3\ell)$ or $\mathrm{M}(2\ell + \gamma)$, is on-$Z$, are considered for this test. In order to disambiguate the conversion object for the measurement purposes, the OSSF pair is required to be of opposite flavor to that of the third lepton in the event. As photons that are at a large distance away from the nearest lepton are found to be largely contaminated by non-radiation photons such as those originating from π^0 decays in jets, the photon

TABLE 6.4: Photon-to-electron and muon conversion rates in bins of photon p_{T}.

Photon → muon conversion rate		$(2.5 \pm 0.6)\%$		
		$10 < p_{\mathrm{T}} < 20$ GeV	$20 < p_{\mathrm{T}} < 30$ GeV	$p_{\mathrm{T}} > 30$ GeV
Photon → electron conversion rate	$L_{\mathrm{T}} < 80$ GeV	$(3.5 \pm 0.6)\%$	$(4.0 \pm 0.5)\%$	$(35 \pm 7)\%$
	$L_{\mathrm{T}} > 80$ GeV	$(14 \pm 2)\%$	$(4.4 \pm 0.5)\%$	$(27 \pm 2)\%$

candidates are required to be within $0.3 < \Delta\mathrm{R} < 2.7$ of the nearest lepton and $\Delta\mathrm{R} > 0.4$ away from the nearest identified jet.

Furthermore, the trailing p_{T} photons (approximately 90% of the events) are required to satisfy $R_{p_{\mathrm{T}}} < 3$ where $R_{p_{\mathrm{T}}} = (p_{\mathrm{T}\ell_1} p_{\mathrm{T}\ell_2})/(p_{\mathrm{T}\gamma})^2$, and $p_{\mathrm{T}\ell_1}$ and $p_{\mathrm{T}\ell_2}$ are the other two lowest p_{T} leptons in the event. This $R_{p_{\mathrm{T}}}$ requirement acts as an effective minimum p_{T} cut on the photon as a function of the other leptons p_{T}s which set the energy scale of the event, and is empirically derived observing the 2D distribution of $R_{p_{\mathrm{T}}}$ vs MOSSF as shown in Figure 6.16.

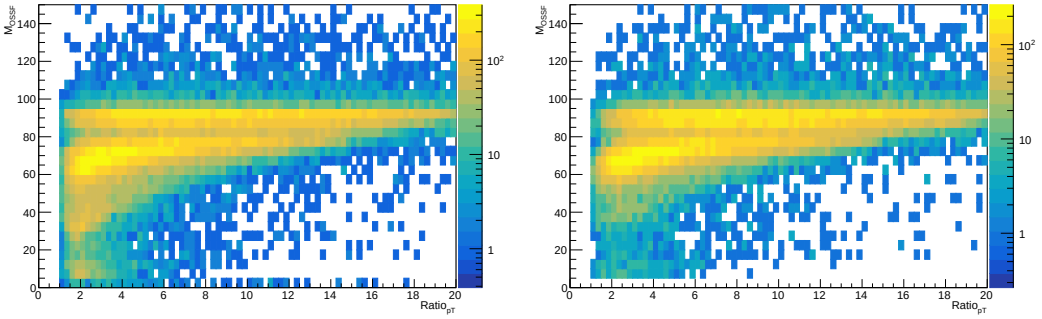

FIGURE 6.16: 2-dimensional $R_{p_{\mathrm{T}}}$ vs MOSSF (GeV) distributions in a selection of data events in $\mu^{\pm}\mu^{\mp}\gamma$ (left) and $e^{\pm}e^{\mp}\gamma$ (right) final states where the photon object is required to be within $0.4 < \Delta\mathrm{R} < 2.7$ of the nearest lepton and $\Delta\mathrm{R} > 0.4$ away from the nearest identified jet.

The photon conversion rate measurement is then conducted for electrons and muons separately, and is parametrized as a function of the p_{T} of the photon candidate and the L_{T} (including the photon p_{T}) of the event. These measurements are summarized in Table 6.4, and all measurement plots are provided in Appendix C. The statistical and systematic uncertainties of the subtracted non-conversion contributions are propagated to the conversion rate calculations, yielding relative uncertainties in the range of 10-20% on the photon conversion rates.

The MOSSF distributions in $\mu^{\pm}\mu^{\mp}e$ (photon-to-electron conversion rate measurement), $e^{\pm}e^{\mp}e$ (photon-to-electron conversion rate closure), $e^{\pm}e^{\mp}\mu$ (photon-to-muon conversion rate closure), and $\mu^{\pm}\mu^{\mp}\mu$ (photon-to-muon conversion rate closure) are shown in Figures 6.17 and 6.18, respectively. A flat systematic uncertainty of 30% is conservatively assigned (larger than the uncertainties on the rates themselves) to the photon conversion

rates in all bins (or equivalently to the conversion background estimate) in order to account for the fluctuations in the expected vs observed ratios in the MOSSF distributions (there is also a 30% systematic uncertainty on the misidentified lepton backgrounds not shown in the ratio panels).

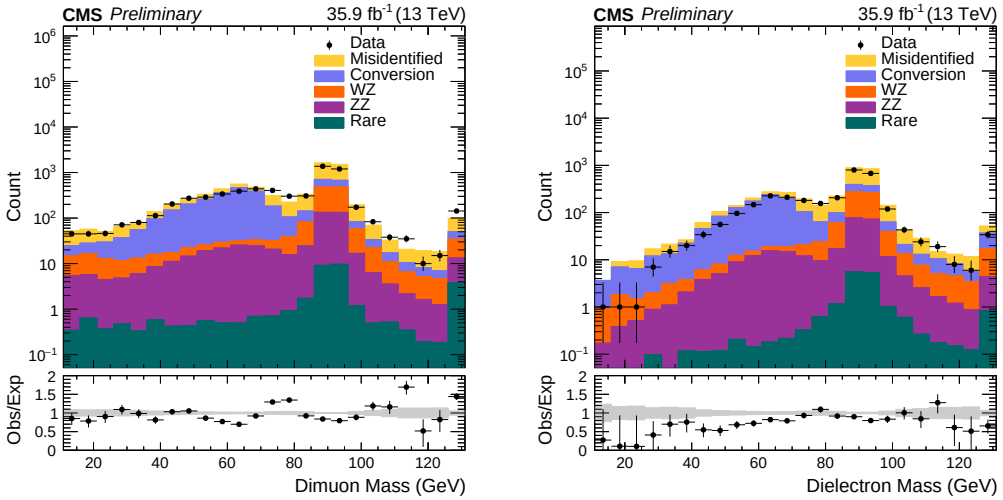

FIGURE 6.17: MOSSF distributions in the conversion electron dominated selection of events in $\mu^{\pm}\mu^{\mp}e$ (left) and $e^{\pm}e^{\mp}e$ (right) final states. Events in the $\mu^{\pm}\mu^{\mp}e$ selection where M(2μ) is below-Z (< 81 GeV) is used to measure the photon-to-electron conversion rates, and those in the $e^{\pm}e^{\mp}e$ selection is used to demonstrate the closure of the method in an orthogonal selection. All selections require $E_{\mathrm{T}}^{\mathrm{miss}} < 50\,\mathrm{GeV}$. Uncertainty bands in the ratio plots in the lower panel include statistical uncertainties only.

The conversion background in 4 lepton events is similarly estimated by applying the rates in Table 6.4 on photons in $3\ell + \gamma$ events. However, the application of the data driven conversion background method in 4 lepton events differ in one aspect from that of the 3 lepton case where $2\ell + \gamma$ events are used. While the fraction of misidentified leptons in $2\ell+\gamma$ events is negligible, this is no longer true for the $3\ell+\gamma$ events. Thus, in order to suppress the double counting of 4 lepton background events where one lepton is a conversion lepton and at least one of the other 3 leptons is a misidentified lepton, the $3\ell + \gamma$ events are therefore corrected by an application of the matrix method on the 3 leptons before obtaining the final conversion background estimate. The bin-by-bin fractions of misidentified lepton contamination in $3\ell + \gamma$ events used in the 4 lepton signal regions in this analysis is provided in Appendix D.

6.6 Systematic Uncertainties

The systematic uncertainties in the context of their sources has been discussed already. In this section I will summarize all the significant uncertainties of this analysis. Table 6.5

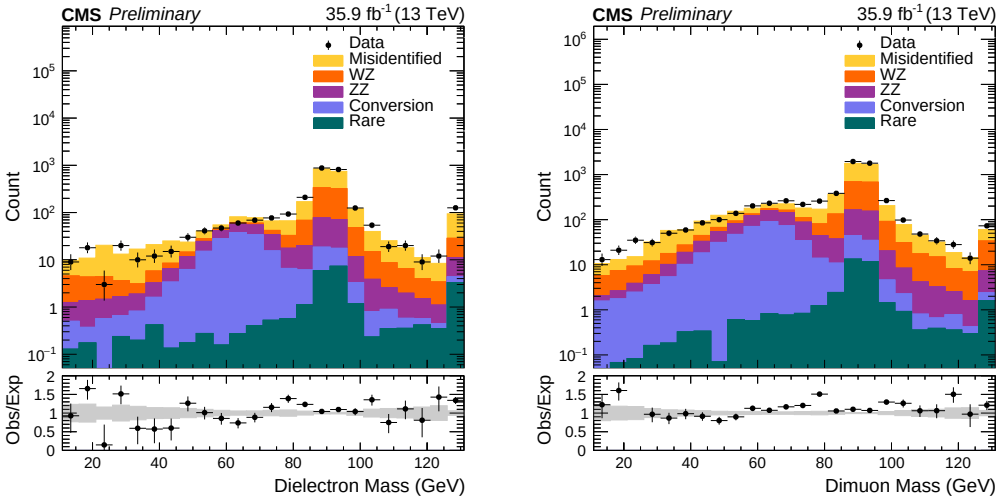

FIGURE 6.18: MOSSF distributions in the conversion muon dominated selection of events in $e^{\pm}e^{\mp}\mu$ (left) and $\mu^{\pm}\mu^{\mp}\mu$ (right) final states. Events in the $e^{\pm}e^{\mp}\mu$ selection where M(2e) is below-Z (< 81 GeV) is used to measure the photon-to-muon conversion rates, and those in the $\mu^{\pm}\mu^{\mp}\mu$ selection is used to demonstrate the closure of the method in an orthogonal selection. All selections require $E_{\mathrm{T}}^{\mathrm{miss}} < 50$ GeV. Uncertainty bands in the ratio plots in the lower panel include statistical uncertainties only.

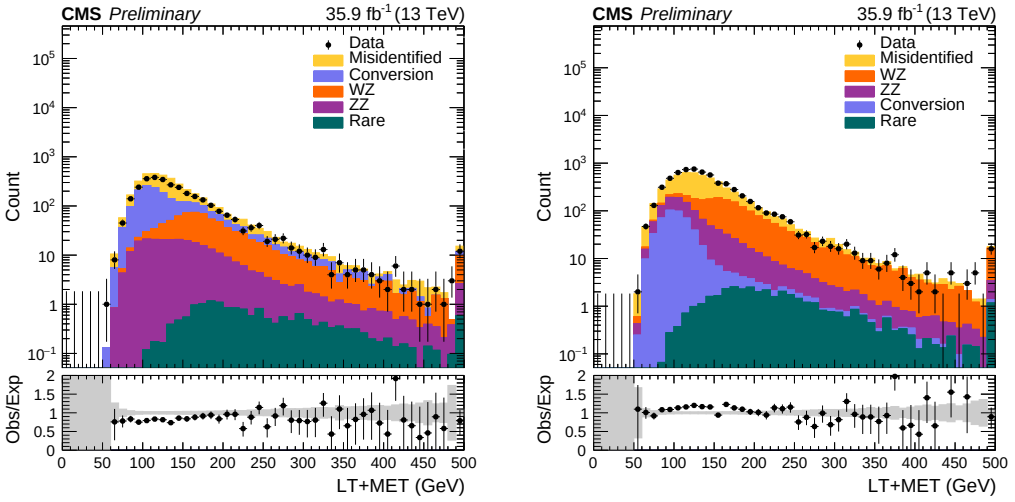

FIGURE 6.19: $L_{\mathrm{T}} + E_{\mathrm{T}}^{\mathrm{miss}}$ distributions in $e^{\pm}e^{\mp}e$ (left) and $\mu^{\pm}\mu^{\mp}\mu$ (right) events with $E_{\mathrm{T}}^{\mathrm{miss}} < 50$ GeV. These selections are orthogonal to the selection of events where photon-to-electron/muon conversion rates are measured, and hence are used to demonstrate the closure of the method. The last bin also includes overflow events, and the uncertainty bands in the ratio plots in the lower panel include statistical uncertainties only.

lists and describe the effect of these uncertainties on the final background estimates as well as the concerned source processes.

Background contributions estimated via the data-driven matrix and photon proxy methods have associated systematic uncertainties that arise due to the uncertainties of the respective prompt, fake, or conversion rates used in these methods. For the matrix method, the process dependent uncertainties assigned due to the DY-$t\bar{t}$ spread discussed in Section 6.4, and the uncertainties on the pile-up and data-MC rate correction factors are propagated to the final prompt and fake rates. The systematic uncertainty on the final background estimate (misidentified lepton backgrounds) in each signal bin is then estimated by varying the muon and electron prompt and fake rates up and down within their respective uncertainties. This calculation is dominated by the uncertainties on the muon and electron fake rates, and is observed to be $\lesssim 30\%$ for most of the signal bins; hence a flat value of 30% is assigned for all regions. Similarly, the total uncertainties on the photon-to-lepton conversion rates directly propagate to the total conversion background, and are estimated to be 30%.

Since background contributions due to all-prompt lepton events are estimated via simulated samples, a number of different sources of systematic uncertainty is considered to account for differences between MC and data events.

The relative WZ and ZZ normalization uncertainties are measured to be 7% and 5%, respectively, in the WZ $\rightarrow 3\ell\nu$ and ZZ $\rightarrow 4\ell$ enriched selections discussed in Sections 6.3.1 and 6.3.2 where the WZ and ZZ samples are normalized to match the total number of data events. The corresponding uncertainties are due to the combination of statistical uncertainties in the data and MC yields, and the propagation of systematic uncertainties on the non-WZ or non-ZZ contributions that are subtracted from the data yield in the normalization calculation. For the sub-dominant, rare background processes such as $t\bar{t}V$, triboson, or associated Higgs production, a 50% systematic uncertainty is applied on the theoretical normalization cross-sections to cover both PDF as well as renormalization and factorization scale uncertainties. Additionally, a luminosity uncertainty of 2.6% is applied to the MC based rare background estimates as well as the signal yields since these are not normalized to data but to the theoretical cross-sections. The impact of PDF uncertainties on signal acceptance has been assessed using the NNPDF replica weights available in signal MC samples, and has been observed to be less than 3% in all signal regions.

The following Physics Object Group recommended per-object and per-event systematic uncertainties are also considered to account for the differences in the modeling of in-time pile-up, trigger, lepton/jet energy and resolution between data and MC events.

TABLE 6.5: Systematic uncertainty sources and typical variations observed in the affected background and signal yields.

Source of uncertainty	Typical Variation (%)	Type	Processes
MisID lepton backgrounds (matrix method)	30	per event	Misidentified
Photon conversion backgrounds (photon proxy method)	30	per event	Conversion
Rare MC backgrounds normalization	50	per event	Rare
Electron charge misidentification	50	per event	WZ/ZZ/Rare (with charge flip)
WZ normalization	7	per event	WZ
ZZ normalization	5	per event	ZZ
Dilepton trigger	2	per event	WZ/ZZ/Rare/Signal
Electron ID & isolation	2	per electron	WZ/ZZ/Rare/Signal
Muon ID & isolation	2	per muon	WZ/ZZ/Rare/Signal
Electron energy scale and resolution	1-5	per event	WZ/ZZ/Rare/Signal
Muon momentum scale and resolution	2-10	per event	WZ/ZZ/Rare/Signal
Jet energy scale	2-8	per event	WZ/ZZ/Rare/Signal
Jet energy resolution	1-8	per event	WZ/ZZ/Rare/Signal
Unclustered energy scale	2-5	per event	WZ/ZZ/Rare/Signal
Integrated luminosity	2.6	per event	Rare/Signal
Pileup	4	per event	WZ/ZZ/Rare/Signal
PDF (on signal acceptance)	3	per event	Signal

The pileup re-weighting uncertainty is evaluated by varying the minimum bias cross-section used in the re-weighting procedure up and down by 5% [65], and is applied to all MC based backgrounds. The changes in the yields of WZ and ZZ backgrounds are observed to be within 4% in the L_{T} $+E_{\mathrm{T}}^{\mathrm{miss}}$, and M_{T} variables. The uncertainties on the muon and electron identification, isolation efficiency scale factors are $\sim$ 2%, and applied per-lepton in each event,whereas the trigger efficiency scale factors have an overall 2-3% impact per event. The jet [147], unclustered energy, and lepton energy (or momentum) scale uncertainties [148] as well as jet [149] and lepton [150, 151] resolution uncertainties are applied at the per-object level, where the corresponding object p_{T}s are varied up and down within the recommended uncertainty range. These variations are then propagated to the kinematic quantities such as $E_{\mathrm{T}}^{\mathrm{miss}}$, L_{T} and M_{T}. A conservative 50% uncertainty is assigned to the simulation based background events due to electron charge misidentification [152] as these type of contributions constitute less than one-third of the total MC based background contributions in 3 lepton OSSF0 and 4 lepton OSSF1 signal regions and are negligible in all other signal regions.

A summary of the uncertainty sources considered in this analysis and the corresponding typical variations in the affected processes is provided in Table 6.5.

Chapter 7

Results and Interpretation

In this chapter I will discuss the results of the multilepton analysis and their statistical interpretation in the context of type-III seesaw model. All the processes which can provide similar signature (in this case "Multileptonic") as that of signal, referred to as backgrounds, are estimated with MC simulation and data driven methods as described in the previous Chapter 6. The backgrounds are then verified in so called "control regions", where the data is partially un-blinded, this does not have affect on the search regions, where the contributions from control region are removed. The control regions are designed in such a way that very small amount of data is used, and majority of the observed events are available in search regions. The final step of the analysis is to put the observed data (un-blinding the data) in the previously defined search regions. The un-blinded data in the search region is compared to the estimated background, to find out the search result. The search result is interpreted using special statistical techniques which are discussed in detail. The results of various search regions are independent and uncorrelated, they would later be combined to obtain a unique exclusion limit on the model in various lepton branching ratio scenarios.

7.1 Observation of the data in 3 or more light lepton channels

The $L_{\mathrm{T}} + p_{\mathrm{T}}^{\mathrm{miss}}(M_{\mathrm{T}})$ variable is optimized in the various search regions to distinguish signal and backgrounds, as described in Chapter 5-6, the search regions for this channel are listed in Table 5.2. The $L_{\mathrm{T}} + p_{\mathrm{T}}^{\mathrm{miss}}$ distribution in the 3 lepton, below-Z signal region is presented in Fig 7.1, where a good agreement is observed between the expected and observed number of events. Although not used for signal discrimination, L_{T}, $p_{\mathrm{T}}^{\mathrm{miss}}$, primary vertex multiplicity, and jet multiplicity distributions for this same selection of

TABLE 7.1: Observed and expected number of events with 3 and 4 or more leptons in the 48 signal regions, classified by the number of leptons, the presence and the mass of an OSSF pair, and $L_{\mathrm{T}} + p_{\mathrm{T}}^{\mathrm{miss}}$ or M_T . The uncertainties quoted on the expected number of background events include statistical and systematic uncertainties.

Signal Region	Discriminating variable							
	$L_{\mathrm{T}} + p_{\mathrm{T}}^{\mathrm{miss}}$ (0-150 GeV)		$L_{\mathrm{T}} + p_{\mathrm{T}}^{\mathrm{miss}}$ (150-300 GeV)		$L_{\mathrm{T}} + p_{\mathrm{T}}^{\mathrm{miss}}$ (300-450 GeV)		$L_{\mathrm{T}} + p_{\mathrm{T}}^{\mathrm{miss}}$ (450-600 GeV)	
	Obs.	Exp.	Obs.	Exp.	Obs.	Exp.	Obs.	Exp.
L3BelowZ	183	177±32	1022	990±210	163	148±28	25	29.4±4.9
L3AboveZ	313	260±56	1038	930±160	246	235±34	59	60.8±8.1
L3OSSF0	228	232±56	654	710±180	107	93±22	16	18.1±4.4
L4OSSF1	2	6.2±1.8	18	28.2±5.5	14	10.5±3.5	6	4.3±1.6
L4OSSF2	21	28.2±6.1	57	54±11	25	21.1±4.6	6	5.9±1.5
	$L_{\mathrm{T}} + p_{\mathrm{T}}^{\mathrm{miss}}$ (600-750 GeV)		$L_{\mathrm{T}} + p_{\mathrm{T}}^{\mathrm{miss}}$ (750-900 GeV)		$L_{\mathrm{T}} + p_{\mathrm{T}}^{\mathrm{miss}}$ (900-1050 GeV)		$L_{\mathrm{T}} + p_{\mathrm{T}}^{\mathrm{miss}}$ ($>$ 1050 GeV)	
	Obs.	Exp.	Obs.	Exp.	Obs.	Exp.	Obs.	Exp.
L3BelowZ	5	6.9±1.6	4	1.57±0.50	0	0.38±0.17	0	0.61±0.34
L3AboveZ	16	20.9±2.7	6	6.88±1.17	3	2.78±0.65	3	3.58±0.73
L3OSSF0	7	4.3±1.2	3	1.97±0.65	0	0.34±0.18	0	0.71±0.36
L4OSSF1	1	1.39±0.55	1	0.41±0.24	0	0.78±0.65	0	0.08±0.05
L4OSSF2	2	2.09±0.56	0	0.99±0.27	0	0.48±0.18	1	0.32±0.10
	M_T (0-100 GeV)		M_T (100-200 GeV)		M_T (200-300 GeV)		M_T (300-400 GeV)	
	Obs.	Exp.	Obs.	Exp.	Obs.	Exp.	Obs.	Exp.
L3OnZ	816	840±150	137	115±20	22	19.1±3.4	5	7.2±1.5
	M_T (400-500 GeV)		M_T (500-600 GeV)		M_T (600-700 GeV)		M_T ($>$ 700 GeV)	
	Obs.	Exp.	Obs.	Exp.	Obs.	Exp.	Obs.	Exp.
L3OnZ	2	1.67±0.51	1	1.24±0.44	1	0.77±0.28	0	0.63±0.27

events are provided in Fig 7.2. Centrally produced 380 GeV and 700 GeV seesaw signal mass point is used to demonstrate the expected signal yield. The$L_{\mathrm{T}} + p_{\mathrm{T}}^{\mathrm{miss}}(M_{\mathrm{T}})$ distributions in the remaining 3 lepton (on-Z, above-Z, and OSSF0) and 4 lepton (OSSF1, OSSF2) signal regions are provided in Fig 7.3-7.5.

Search results are consolidated in Table 7.1, where expected, observed and signal events for each search bin are listed.

The distributions reveal no statistically significant deviations from the SM expectations and as evident from the Table 7.1, observed number of events is in an overall agreement with the standard model (background only) prediction.

7.2 Limits Calculation

The observation of the events in both the main search regions is consistent with the standard model expectations. Although this indicates no possibility of seesaw mechanism with this amount of data(35.9 fb^{-1}), center-of-mass energy(13 TeV) and current

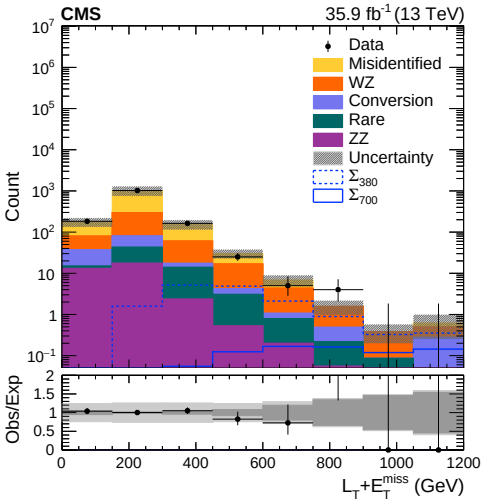

FIGURE 7.1: $L_{\mathrm{T}} + E_{\mathrm{T}}^{\mathrm{miss}}$ distribution for the 3 lepton, below-Z signal region as defined in Table 5.2. The expected yields of the Seesaw signal model with $\mathrm{M}_{\Sigma} = 380$ GeV and $\mathrm{M}_{\Sigma} = 700$ GeV are overlaid. The last bin includes overflow events. The uncertainty band includes systematic uncertainties listed in Table 6.5.

experimental setup, this result can be quantified to constrain the type-III seesaw mechanism. A limit is set in each of the two channels as well as by combining them, on the production cross-section of seesaw particles using the $\mathrm{CL_s}$ modified frequentist approach [12, 153–155]. The method is discussed briefly in subsequent section following closely the reference [153].

$\mathrm{CL_s}$ Method

To derive exclusion limits, the comparison is done between the background-only(b) and signal plus background($s + b$) hypotheses. The potentially new physics signal is constrained by quantifying the incompatibility of the observed data with the signal plus background hypothesis. The $\mathrm{CL_s}$ technique, a combination of frequentist and Bayesian features, is useful in searches with small signal on top of a large background. This method modifies certain features, apparent in searches like this analysis, where overestimating the background can yield small upper limits on the signal cross-section. It avoids false exclusion when the experiment has little sensitivity signal. This effect is reduced by consideration of compatibility of observed data with the background only hypotheses, in the $\mathrm{CL_s}$ construction. The $\mathrm{CL_s}$ also provides with the upper limits on cross-sections and masses derived from theoretical models where the possible range of the model parameters is constrained.

A test statistics is defined which discriminates signal-like outcomes from background-like scenarios, in the form of likelihood ratio [155]. If the estimated signal in the i^{th} channel

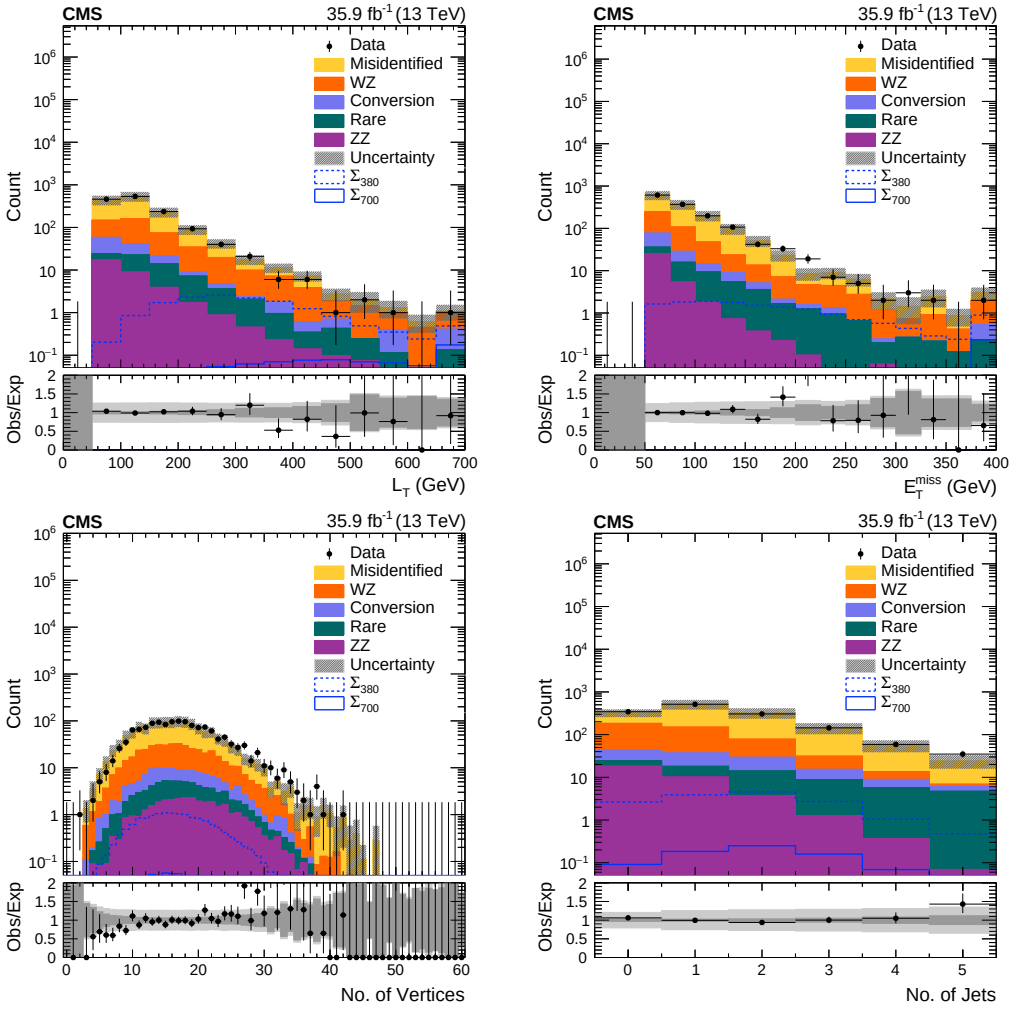

FIGURE 7.2: L_{T} (upper left), $E_{\mathrm{T}}^{\mathrm{miss}}$ (upper right), primary vertex multiplicity (lower left), and jet multiplicity (lower right) distributions for the 3 lepton, below-Z signal region as defined in Table 5.2. The expected yields of the Seesaw signal model with $\mathrm{M}_{\Sigma} = 380$ GeV and $\mathrm{M}_{\Sigma} = 700$ GeV are overlaid. The last bins include overflow events, and the uncertainty bands in the ratio plots include statistical (dark) and systematic (light) uncertainties.

is s_i, the estimated background is b_i, and the number of observed candidates is d_i, then Q can be written as,

$$Q = \prod_{i=1}^{n} Q_i \tag{7.1}$$

where,

$$Q_i = \frac{e^{-(s_i+b_i)}(s_i+b_i)^{d_i}}{d_i!} \Bigg/ \frac{e^{-b_i} b_i^{d_i}}{d_i!} \tag{7.2}$$

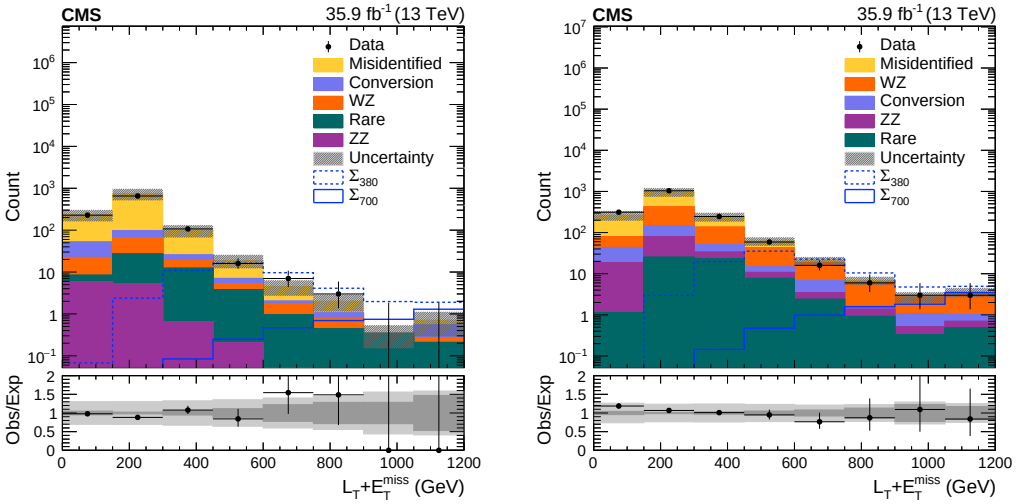

FIGURE 7.3: $L_{\mathrm{T}} + E_{\mathrm{T}}^{\mathrm{miss}}$ distributions in the 3 lepton OSSF0 (left) and above-Z (right) signal regions as defined in Table 5.2. The expected yields of the Seesaw signal model with $\mathrm{M}_{\Sigma} = 380$ GeV and $\mathrm{M}_{\Sigma} = 700$ GeV are overlaid. The last bins include overflow events, and the uncertainty bands in the ratio plots include statistical (dark) and systematic (light) uncertainties.

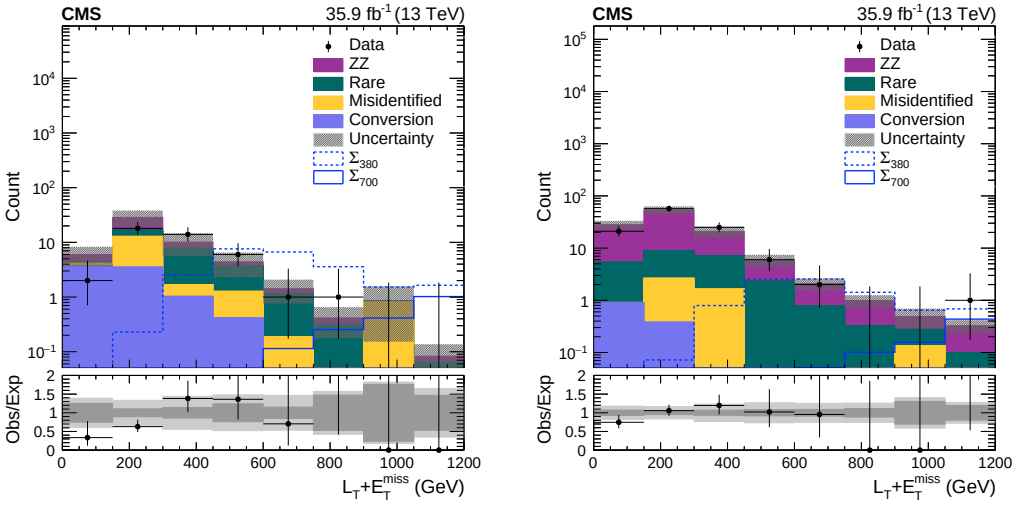

FIGURE 7.4: $L_{\mathrm{T}} + E_{\mathrm{T}}^{\mathrm{miss}}$ distributions in the 4 lepton OSSF1 (left) and OSSF2 (right) signal regions as defined in Table 5.2. The expected yields of the Seesaw signal model with $\mathrm{M}_{\Sigma} = 380$ GeV and $\mathrm{M}_{\Sigma} = 700$ GeV are overlaid. The last bins include overflow events, and the uncertainty bands in the ratio plots include statistical (dark) and systematic (light) uncertainties.

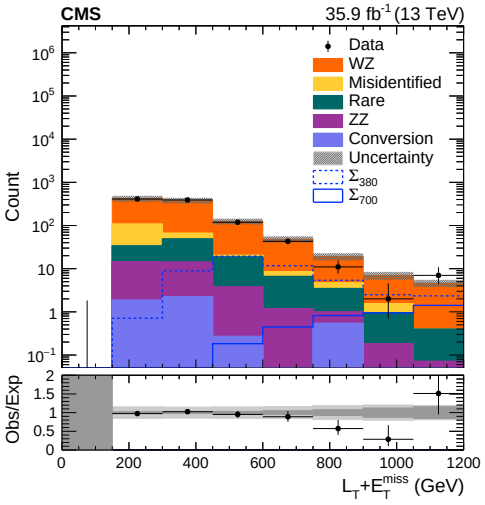

FIGURE 7.5: M_{T} distribution in the 3 lepton on-Z signal region as defined in Table 5.2. The expected yields of the Seesaw signal model with $\mathrm{M}_{\Sigma} = 380$ GeV and $\mathrm{M}_{\Sigma} = 700$ GeV are overlaid. The last bin includes overflow events, and the uncertainty bands in the ratio plot include statistical (dark) and systematic (light) uncertainties.

For the $s+b$ hypothesis, the confidence level is expressed in the form of the probability, which is calculated assuming the presence of both signal and background at their hypothesized levels, such that the test statistic would be less than or equal to that observed in the data.

$$CL_{s+b} = P_{s+b}(Q \leq Q_{observed}) \tag{7.3}$$

The probability is the sum of Poisson probabilities

$$P_{s+b}(Q \leq Q_{observed}) = \sum_{Q(d'_i) \leq Q(d_i)} \prod_{i=1}^{n} \frac{e^{-(s_i+b_i)}(s_i+b_i)^{d_i}}{d'_i!} \tag{7.4}$$

where $Q(d_i)$ is the test statistic computed for observed events in each channel d_i, and the sum runs over all possible outcomes (d'_i) with test statistics less than or equal to the observed one. The confidence level $(1 - CL_{s+b})$ is used to quote the exclusion limits. This exclusion limit has an important draw-back that if too few candidates are observed to account for the estimated background, then any signal, and even the background itself, may be excluded at a high confidence level. To overcome this draw back a typical limit computation ($\mathrm{CL_s}$), involves also computing the confidence level for the background alone,

$$CL_b = P_b(Q \leq Q_{observed}) \tag{7.5}$$

where the probability sum assumes the presence only of the background. This confidence level has been suggested to quantify the confidence of a potential discovery, as it expresses

the probability that background processes would give fewer than or equal to the number of candidates observed. (re-frame sentence)

The modified frequentist confidence level $\mathrm{CL_s}$ is then defined as,

$$\mathrm{CL_s} = \frac{CL_{s+b}}{CL_b} \tag{7.6}$$

Eq. 7.3 and Eq. 7.5 are carried out by computing the probability distribution function (PDF) for the test statistics for set of channels and convoluting with the PDF's of the test statistic of additional channels, and then summing over as in Eq. 7.4. Adopting the procedure for $\mathrm{CL_s}$ prescribed by CMS experiment, for "Observed" and "expected" exclusion limit are calculated for this analysis, a brief discussion about the procedure follows.

Observed limit

The LHC-style prescription based on the $\mathrm{CL_s}$ method [12] is used to derive exclusion limit for this analysis. This method uses the profile likelihood test statistics, q_u. With the signal strength μ, following procedure is adopted for the observed limit calculation,

- A likelihood function is constructed with observed data, signal strength μ, and with full suite of nuisance parameters represented by θ

$$\mathcal{L}(\mathrm{data}|\mu,\theta) = \mathrm{Poisson}(\mathrm{data}|\mu.s(\theta)+b(\theta)).p(\tilde{\theta}|\theta) \tag{7.7}$$

  Poisson(data|μs+b) stands for product of Poisson probabilities as described earlier, s and b stands for usual signal and background rate.

- To compare the compatibility of the data with the background-only (H_b) and signal+background (H_{s+b}) hypotheses, the test statistic $\tilde{q_\mu}$ based on the profile likelihood ratio,

$$\tilde{q_\mu} = -2ln\frac{\mathcal{L}(data|\mu,\hat{\theta_\mu})}{\mathcal{L}(data|\hat{\mu},\hat{\theta})}, \qquad \text{with a constraint } \; 0 \leq \hat{\mu} \leq \mu \tag{7.8}$$

  where $\hat{\theta}_\mu$ stands for the conditional maximum likelihood estimators of θ, the pair $\hat{\theta}$ and $\hat{\mu}$ refers to the global maximum of the likelihood.

  The constraint is derived from physics which makes signal rate positive, whereas the upper constraint is imposed to ensure a one-sided confidence. A physics meaning imparted from this is upward fluctuations of the data such that $\hat{\mu} > \mu$ are not considered as evidence against the signal hypothesis.

– Determine the observed value of the test statistics q_μ^{obs}, for the given signal strength μ under test.

– Find estimator values for the nuisance parameters $\hat{\theta}_0^{obs}(\mu = 0)$, and $\hat{\theta}_\mu^{obs}$, which maximizes the likelihood for the H_b and H_{s+b} hypotheses, respectively.

– Generate toy MC pseudo-data to construct PDF's $f(\tilde{q}_\mu|\mu, \hat{\theta}_\mu^{obs})$ and $f(\tilde{q}_\mu|0, \hat{\theta}_0^{obs})$ for H_{s+b} with signal strength μ and for H_b hypotheses. All these distributions are shown in Fig. 7.6. It is important to note that for the purposes of generating a pseudo-dataset, the nuisance parameters are fixed to the values $\hat{\theta}_\mu^{obs}$ or $\hat{\theta}_0^{obs}$ obtained by fitting the observed data, but are allowed to float in fits needed to evaluate the test statistic. This ensures that nuisance parameters which are fixed to their maximum likelihood estimates, shows good coverage properties [].

– From the above constructed $f(\tilde{q}_\mu|\mu, \hat{\theta}_\mu^{obs}$ and $f(\tilde{q}_\mu|0, \hat{\theta}_0^{obs})$ distributions, define two p-value integrals, p_μ and p_b for H_{s+b} and H_b hypotheses,

$$p_\mu = P(\tilde{q}_\mu \geq \tilde{q}_\mu^{obs}|\mathrm{H}_{s+b}) = \int_{\tilde{q}_\mu^{obs}}^{\infty} f(\tilde{q}_\mu|\mu, \hat{\theta}_\mu^{obs})\mathrm{d}\tilde{q}_\mu \tag{7.9}$$

$$1 - p_b = P(\tilde{q}_\mu \geq \tilde{q}_\mu^{obs}|\mathrm{H}_b) = \int_{\tilde{q}_0^{obs}}^{\infty} f(\tilde{q}_\mu|0, \hat{\theta}_0^{obs})\mathrm{d}\tilde{q}_\mu \tag{7.10}$$

$\mathrm{CL_s}(\mu)$ upper limit, is the ratio of these two probabilities,

$$\mathrm{CL_s}(\mu) = \frac{p_\mu}{1 - p_b} = \frac{\mathrm{CL}_{s+b}(\mu, q_\mu^{obs})}{\mathrm{CL}_b(q_\mu^{obs})} \leq \alpha \tag{7.11}$$

The CL_{s+b} value represents the probability to observe a data set with true signal strength μ, with the test statistic value equal to or larger than q_μ, and CL_b represents probability without signal ($\mu = 0$). The denominator CL_b prevents exclusion when there is a very low sensitivity to the signal.

– The signal model is excluded at the $(1-\alpha)\%$ confidence level, if $\mu = 1$ and $\mathrm{CL_s} \leq \alpha$. α is typically selected to be 0.05, *i.e* 95% confidence level upper limit. In this analysis 95% limit is quoted in democratic scenario (branching ratio $B_\mathrm{e} = B_\mu = B_\tau$) as well as a 2D plot where 95% upper limits are given in varying branching fraction scenarios to all the leptons.

When the signal strength μ equals to zero, it is expected that $\mathrm{CL}_{s+b} \leq 0.05$, which implies that 5% of all the search bins will result in excluding a signal strength of zero. The $\mathrm{CL_s}$ method accounts for the fact that what is observed is a downward fluctuation in the background that causes a deficit in the observed number of events, that is inconsistent

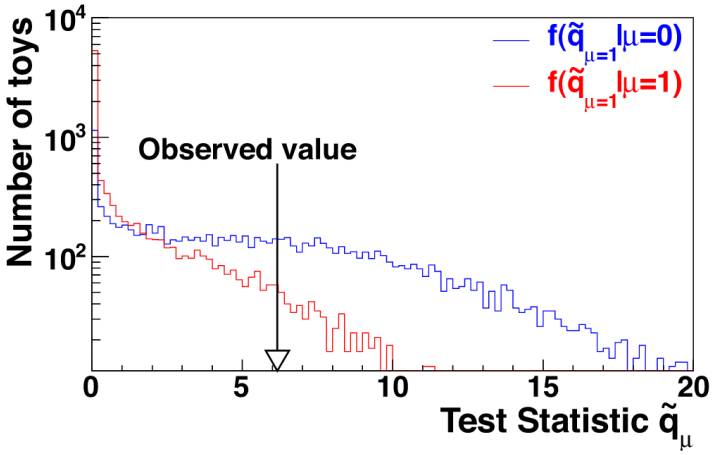

FIGURE 7.6: Test statistic distributions for ensembles of pseudo-data generated using signal+background and background-only hypotheses. [12]

with the expected background. This can cause H_{s+b} being excluded in scenarios when there is no real experimental sensitivity or expected signal is quite small. The CL_s confidence level has a built in protection against this behaviour of CL_{s+b}, in the form of denominator CL_b which regulates it.

Expected limit

An expected limit for a new physics model is calculated by considering background only hypothesis, confidence level for which is given by,

$$CL_b = P_b(Q \leq Q_{obs}) \tag{7.12}$$

where the probability sum is calculated assuming the presence of the background alone. A large set of generated pseudo-datasets assuming background only hypothesis (including nuisance parameters), treated as if it were real data, is used to calculate the signal strength (for each of the data-sets) for which $textCL_s = 0.05(\mu^{95\%})$. A cumulative probability distribution is then formed from $\mu^{95\%}$ values, from which the median expected value (50% quantile), $\pm 1\sigma$(16% and 84% quantiles) bands, and $\pm 2\sigma$(2.5% and 97.5% quantiles) bands can be extracted, as shown in Fig. 7.7.

This fairly straight-forward calculation, involves generating thousands of toy MC simulations, which can become cumbersome and computationally heavy. Asymptotic limits, which do not require the use of toy MC samples, can be used as an excellent approximation of full CL_slimits, when expected number of events are large enough [155]. The set of simulated pseudo-data can be replaced by a single dataset with specific properties,

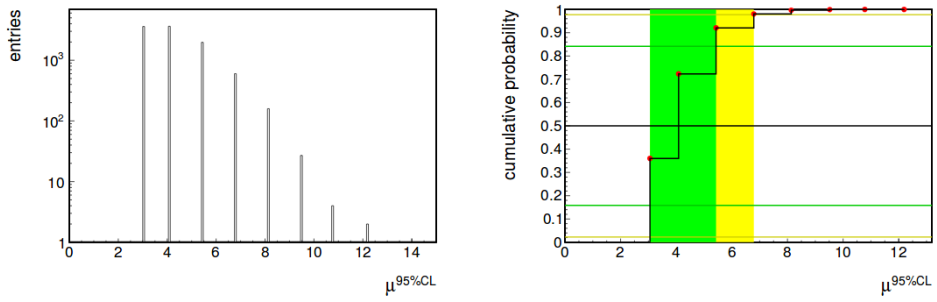

FIGURE 7.7: For the background only(s = 1, b = 1, no systematic errors) hypothesis, an example of differential distribution of possible limits on μ(Left). Cumulative probability distribution of the plot on the left with 2.5%, 16%, 50%, 84%, and 97.5% quantiles (horizontal lines) defining the median expected limit as well as the $\pm 1\sigma$ (68%) and $\pm 2\sigma$ (95%) bands for the expected value of μ for the background-only hypothesis(Right). [12]

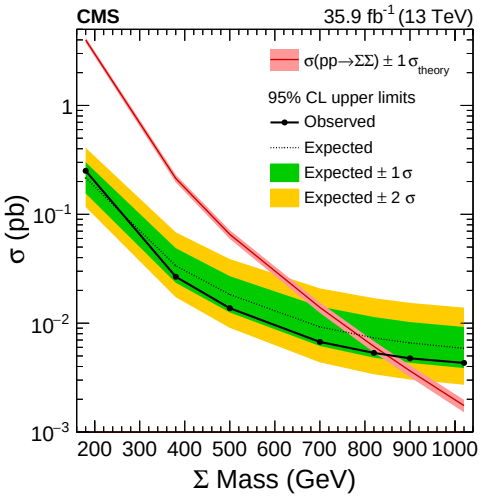

FIGURE 7.8: Observed exclusion limit at 95% CL on the production cross-section of Σ pairs, as calculated with the asymptotic CLs mode of the Higgs Combination Tool. All systematic uncertainties listed in Table 6.5 are included.

called as Asimov dataset, in honour of author Isaac Asimov. Use of the Asimov dataset permits the computation of median expected limit as well as the uncertainty bands.

7.3 Results

An expected and observed upper limit is calculated on the production cross-section Σ pairs using the asymptotic CL_S method at 95% CL, where a counting experiment is performed in each signal bin for the statistical analysis. The uncertainties on the mean values of expected signal and background yields are treated as nuisance parameters modeled by log-normal and gamma distributions for systematic and statistical uncertainties,

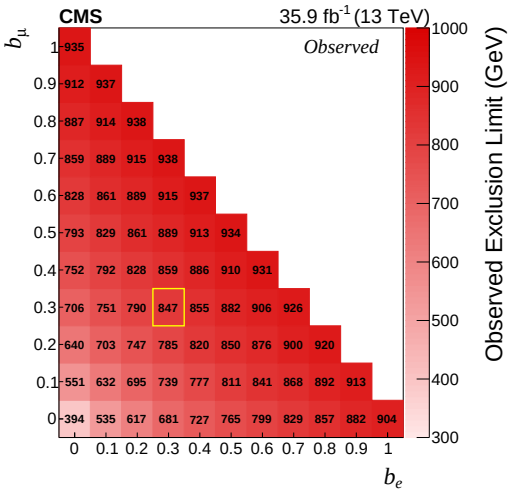

FIGURE 7.9: 2D EleMu branching ratio dependent Observed exclusion limits at 95% CL on the production cross-section of Σ pairs, as calculated with the asymptotic CLs mode of the Higgs Combination Tool.

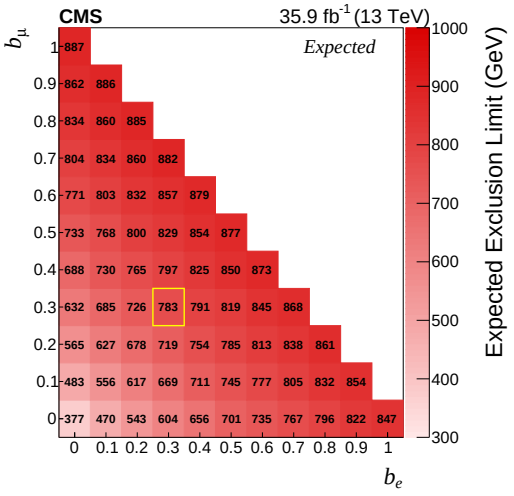

FIGURE 7.10: 2D EleMu branching ratio dependent Expected exclusion limits at 95% CL on the production cross-section of Σ pairs, as calculated with the asymptotic CLs mode of the Higgs Combination Tool.

respectively. Statistical uncertainties on the signal and background yields are assumed to be fully uncorrelated, whereas all other systematic uncertainties are assumed to be fully correlated among the 48 signal channels. No statistically significant excess was observed in the various signal regions that has been probed.

A 95% confidence level upper limit on the cross section sum for the production of heavy fermion pairs ($\Sigma\Sigma^+$, $\Sigma^0\Sigma^-$, or $\Sigma^+\Sigma^-$) is calculated using the CLs method [12, 153–155, 157]. Figure 7.8 shows the upper limit on the cross section in the flavor-democratic scenario. In this scenario, we rule out the production of heavy fermion pairs for masses less than

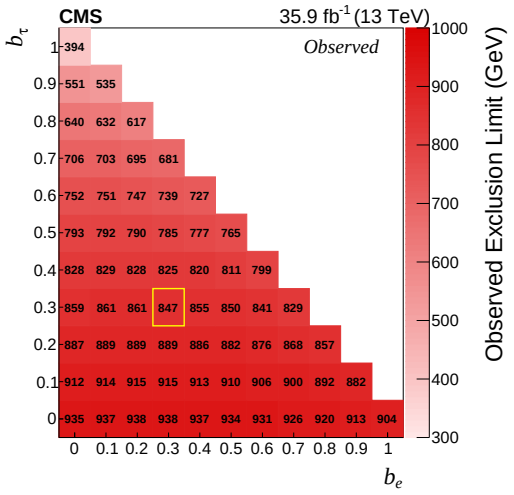

FIGURE 7.11: 2D EleTau branching ratio dependent Observed exclusion limits at 95% CL on the production cross-section of Σ pairs, as calculated with the asymptotic CLs mode of the Higgs Combination Tool.

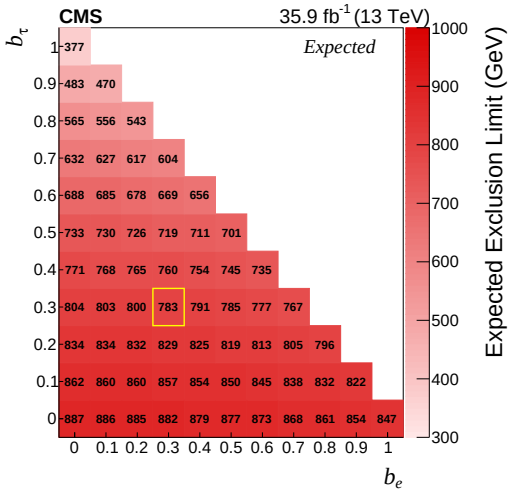

FIGURE 7.12: 2D EleTau branching ratio dependent Expected exclusion limits at 95% CL on the production cross-section of Σ pairs, as calculated with the asymptotic CLs mode of the Higgs Combination Tool.

847 GeV. The expected limit in this case is 783 GeV. The signal cross section has an uncertainty of approximately 5-15% due to choices of scale and PDF in the mass range we consider and this uncertainty is shown in Fig. 7.8. Figure 7.9 to 7.12 shows the expected and observed excluded mass limits in the b_e-b_μ plane and b_e-b_τ respectively (note that $b_\mu = 1 - [b_e + b_\tau]$). The limits are the most restrictive when the Σ branching fraction to electrons and muons is maximal, and decrease as the branching fraction to taus increases. The overall expected signal selection efficiencies and the expected signal significance's as a function of the Σ mass are provided in Figure 7.13.

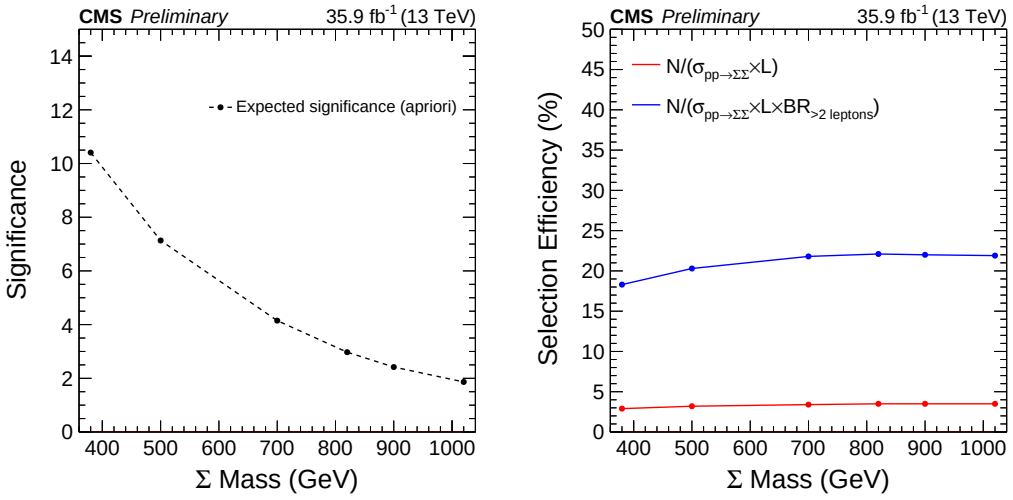

FIGURE 7.13: Expected (apriori) significance of the signal model (left) as a function of the Σ mass, as calculated with the profile-Likelihood mode of the Higgs Combination Tool. All systematic uncertainties listed in Table 6.5 are included. Expected signal efficiency as a function of the Σ mass (right), where N is the total number of expected signal events summed over all signal regions, L is the total luminosity of the dataset and $BR_{>2\ leptons}$ is the total branching fraction of the Σ pairs into 3 or more leptons (including taus, and calculated at a Σ mass of 660 GeV for simplicity) in the flavor democratic mixing scenario considered for this analysis.

The expected exclusion limit in the 2015 version of this analysis [134] with the 2.3 fb^{-1} of data was at a Σ mass of 430 GeV and a signal cross-section of 130 fb, whereas the current expected exclusion limit is at 783 GeV and 7 fb. This represents a factor of ∼18.6 improvement in the excluded signal cross-section, which corresponds to an approximately linear increase with luminosity.

Chapter 8

Possible extension with hadronic taus

The search presented in this thesis uses light leptons i.e. electron and muon for all the channels, taus are considered through their decays to light leptons. A possible extension to this search can be an inclusion of search region with hadronic taus. There are various ways to include more mutually exclusive search regions with hadronic taus such as 2 light leptons plus one or more tau, 3 light leptons plus one or more hadronic tau and so on. In this chapter I will describe the possible improvement in the limits if such a channel were to be included in this search.

I will specifically consider a channel with exactly two light leptons plus one or more hadronic tau. This channel is mutually independent of other channels described in earlier chapters 5 and 6. Candidate events in this search channel must have at least three leptons, one of them must always be a hadronic tau. The other two can be a electron or muon. In case of more than one τ, only the one leading in p_{T} is considered. The events in which there are more than 2 light leptons are vetoed. This channel is referred to as L2T1, where L2 stands for a pair of light leptons and T1 for a always present tau.

The backgrounds to this extension are similar as that of light lepton channels and consist of prompt leptons arising from boson decay, as well as non-prompt leptons. Non-prompt leptons include leptons arising from heavy-flavor quark decays, or from leptons occurring inside or near jets, as well as misidentified leptons from hadrons that punch through into the muon system, or from hadronic showers with large electromagnetic fractions. Non-prompt leptons are here also referred to as misidentified leptons, as they were in case of light lepton channels.

The data for this extension are collected using single electron and single muon triggers. The single electron trigger requires an electron with a p_{T} threshold of 27 GeV. The single muon trigger requires a muons with a p_{T} threshold of 24 GeV. The off-line selection criteria for light leptons is similar to light lepton channels, as described in chapter6. Tau candidates with $p_{\mathrm{T}} > 20$ GeV, $|\eta| < 2.3$ are selected using hadron-plus-strips (HPS) algorithm reconstructed in 1- or 3- prong decay modes with or without additional π^0 particles [11, 109–111]. Longitudinal impact parameter of tau candidates from primary vertex is required to be < 0.2 cm. The tau candidates are also required to pass an isolation requirement. All isolation quantities are corrected for contributions of particles originating from pileup vertices. All the other quantities such as $p_{\mathrm{T}}^{\mathrm{miss}}$ and jets are reconstructed similarly as in case of light lepton channels and are described in chapters 5 and 6.

In a similar way to light lepton event selection, events with lepton pair with mass below 12 GeV are vetoed to reduce background from low-mass resonances. Tri-lepton events with an OSSF pair with mass below 76 GeV, when the trilepton mass is within a Z-mass window (91 15 GeV) are also rejected. This reduces background from asymmetric photon conversions in $\mathrm{Z} \to \ell\ell^* \to \ell\ell\gamma$, where the photon converts into two additional leptons, one of which is lost.

The L2T1 events are classified further into non-overlapping search channels on the basis of the number of lepton relative charges, charge and flavor combinations, and other kinematic variables. The classification strategy is adapted from light lepton channels, where events are classified depending upon light lepton pair forming a Z-mass or near to it. The leading electron(muon) is required to satisfy $p_{\mathrm{T}} > 30(25)$ GeV in order for the single lepton triggers to be fully efficient. The trailing light leptons are required to satisfy a threshold of 10 GeV, in case of a tau off-line p_{T} threshold for selection is 20 GeV. The events are further divided in eight bins of $L_{\mathrm{T}} + p_{\mathrm{T}}^{\mathrm{miss}}$, given the relatively high signal lepton momenta due to the large masses of the parent particles (Heavy fermions) and accompanying neutrinos. The kinematic quantity L_{T} is now defined as a scalar p_{T} sum of the light lepton pair and the leading tau. A bin of width 150 GeV for $L_{\mathrm{T}} + p_{\mathrm{T}}^{\mathrm{miss}}$ is used, and in each case the highest bin includes overflow events.

As a result, for L2T1 search region, we have four $L_{\mathrm{T}} + p_{\mathrm{T}}^{\mathrm{miss}}$ distributions, depending upon the light lepton pair properties:

- 2 light lepton plus a leading tau without an OSSF pair (Distribution:$L_{\mathrm{T}} + p_{\mathrm{T}}^{\mathrm{miss}}$).
- 2 light lepton plus a leading tau with an OSSF pair "Above-Z" (Distribution:$L_{\mathrm{T}} + p_{\mathrm{T}}^{\mathrm{miss}}$).

TABLE 8.1: The signal regions used in the L2T1 search region, summarized in terms of the number of leptons, the presence of an OSSF pair, and the kinematic variable used for signal discrimination. Each selection described here is further divided into eight bins in the kinematic variable, giving a total of 32 statistically independent signal regions. Additional criteria based on $p_{\mathrm{T}}^{\mathrm{miss}}$ are used to ensure that signal regions are non-overlapping with control regions.

N_{leptons}	Number of OSSF & mass	Kinematic variable	$p_{\mathrm{T}}^{\mathrm{miss}}$ requirement
3	on-Z	$L_{\mathrm{T}} + p_{\mathrm{T}}^{\mathrm{miss}}$	$p_{\mathrm{T}}^{\mathrm{miss}} > 100\,\mathrm{GeV}$
3	1 pair, above-Z	$L_{\mathrm{T}} + p_{\mathrm{T}}^{\mathrm{miss}}$	-
	1 pair, below-Z	$L_{\mathrm{T}} + p_{\mathrm{T}}^{\mathrm{miss}}$	$p_{\mathrm{T}}^{\mathrm{miss}} > 50\,\mathrm{GeV}$
	none	$L_{\mathrm{T}} + p_{\mathrm{T}}^{\mathrm{miss}}$	-

- 2 light lepton plus a leading tau with an OSSF pair "Below-Z" (Distribution:$L_{\mathrm{T}} + p_{\mathrm{T}}^{\mathrm{miss}}$).
- 2 light lepton plus a leading tau with an OSSF pair "On-Z" (Distribution:$L_{\mathrm{T}} + p_{\mathrm{T}}^{\mathrm{miss}}$).

The resulting set of 32 exclusive bins for this search region is described in table 8.1.

Background estimation follow similar strategies that are used in light lepton channels and described in detail in previous chapters 5 and 6. The irreducible backgrounds are estimated using dedicated simulation samples, and are dominated by the WZ and ZZ processes. These processes are normalized to data using dedicated control selections. The ratio of WZ prediction to data (after corrections of non-WZ events) is found to be 1.17 ± 0.07, where the uncertainty includes both statistical and systematic contributions. Similarly, for ZZ, the ratio of ZZ prediction to data is found to be 0.96 ± 0.05. These normalization factors are then used for the WZ and ZZ background estimates. The normalization factors were changed due to the use of single lepton triggered data and the improved MC samples at the time. An additional tau scale factor correction of 0.93 applied to all the MC events including signal.

The backgrounds from misidentified leptons arise from processes such as Z+jets, and $t\bar{t}$. These are estimated using a 3-dimensional implementation of a matrix method, described in detail in chapter 6. The matrix method is a data-driven method that assumes that the probabilities of prompt and misidentified leptons to pass a tight lepton selection, given that they pass a loose lepton selection, are universal. These probabilities, called prompt and misidentification rates, are functions of lepton- and event-dependent parameters. The rates are measured using dedicated selections; a dilepton selection for prompt rates, and a trilepton signal depleted selection (OSSF1 on-Z, $p_{\mathrm{T}}^{\mathrm{miss}} < 50\,\mathrm{GeV}$) for misidentification rates. The rates are parametrized as a function of lepton p_{T}, η, and the p_{T} of AK4 PF jet matched to lepton. The rates measured in data are dominated by

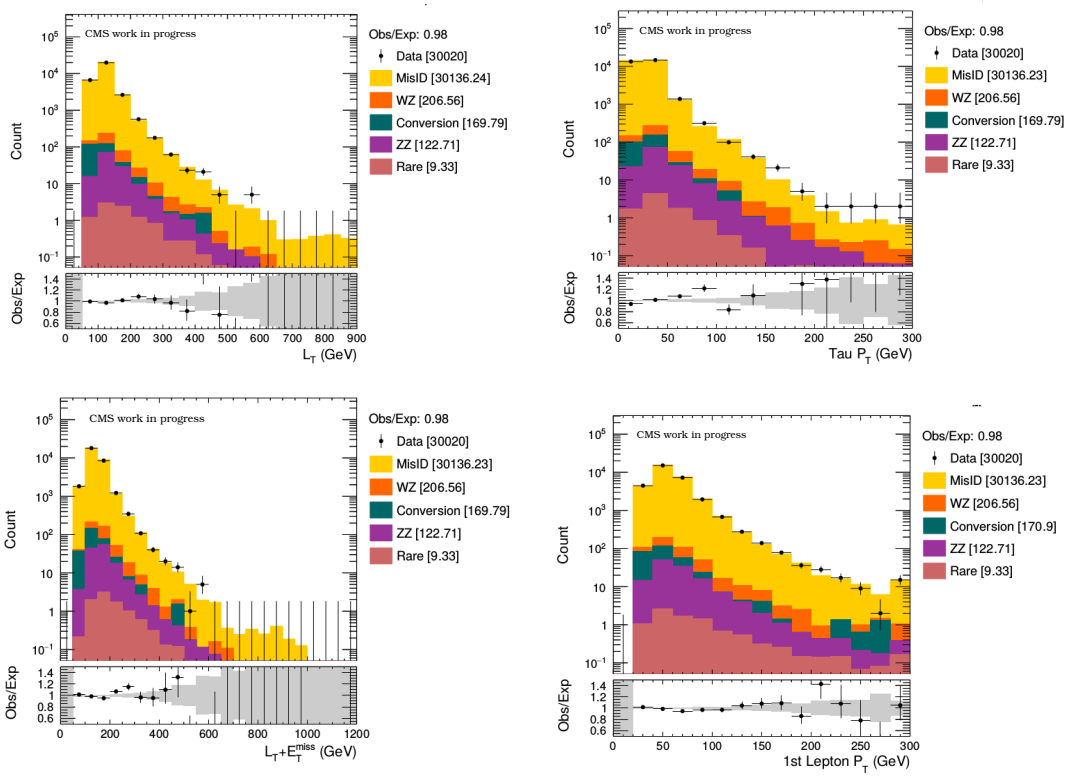

FIGURE 8.1: L_{T} (upper left), Tau p_{T} (upper right), $L_{\mathrm{T}} + p_{\mathrm{T}}^{\mathrm{miss}}$ (lower left), and first lepton p_{T} (lower right) distributions in L2T1 with $p_{\mathrm{T}}^{\mathrm{miss}} < 50\,\mathrm{GeV}$ CR (last bin includes overflow). Uncertainty bands in the ratio plots in the lower panel include statistical uncertainties only.

Z+jets events, and are corrected using simulation to an average of Z+jets and tt+jets events (In case of tau fake rate only track correction factor is applied).

A residual background from photon conversions is treated differently here than light lepton channels. It is estimated using simulation samples normalized in dedicated data control sample. This background, referred to as "conversion" background, is dominated by final-state photon radiation from an existing lepton, where the photon then converts asymmetrically to two additional leptons, only one of which is reconstructed in the detector. A selection of events with invariant mass of the the two leading leptons ($M_{2\ell} < 76\,\mathrm{GeV}$), the invariant trilepton mass ($76 < M_{3\ell} < 106$) and missing transverse energy ($p_{\mathrm{T}}^{\mathrm{miss}} < 50$ GeV) results in a conversion dominant control sample.

To achieve accurate SM backgrounds, a very small amount of data has to be unblinded. This is typically a region where there is very little signal contamination and referred to as control region(CR). Any overlap with background CR's are explicitly vetoed out from final search selection. Following CR's are defined and verified with the data to check the background estimation.

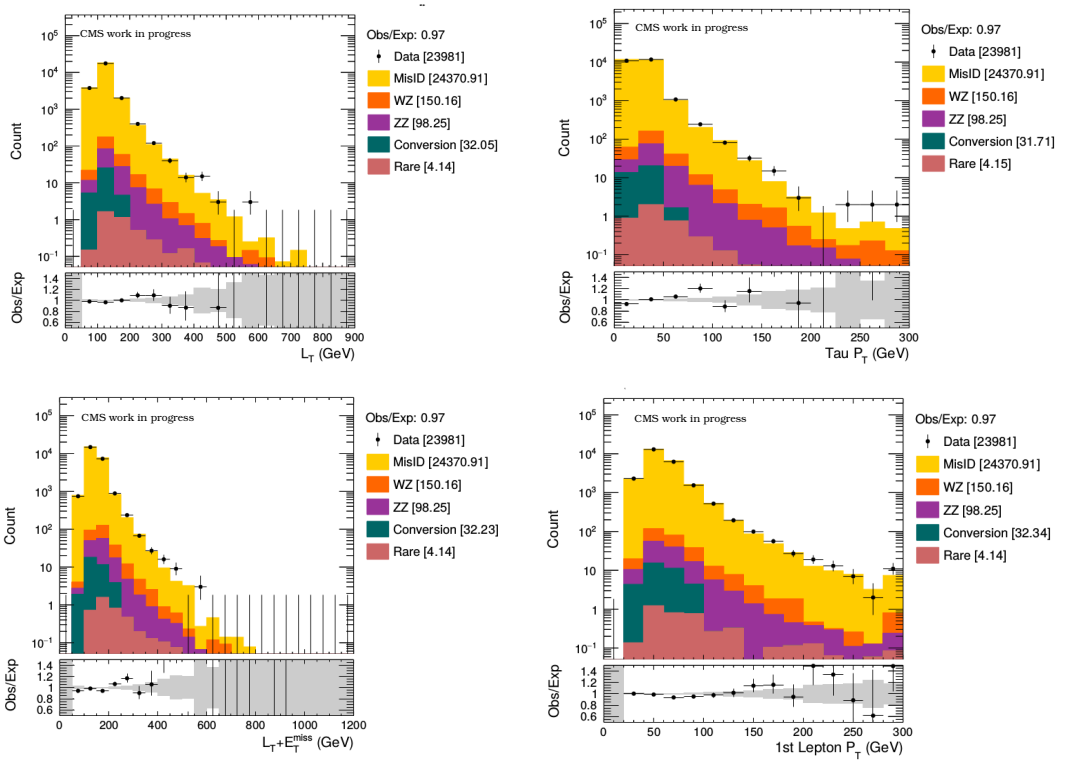

FIGURE 8.2: L_{T} (upper left), Tau p_{T} (upper right), $L_{\mathrm{T}} + p_{\mathrm{T}}^{\mathrm{miss}}$ (lower left), and first lepton p_{T} (lower right) distributions in L2T1-OnZ with $p_{\mathrm{T}}^{\mathrm{miss}} < 50\,\mathrm{GeV}$ CR (last bin includes overflow). Uncertainty bands in the ratio plots in the lower panel include statistical uncertainties only.

- 2 light lepton plus a leading tau with an OSSF pair with $p_{\mathrm{T}}^{\mathrm{miss}} < 50$ GeV (Fig.).
- 2 light lepton plus a leading tau with an OSSF pair "On-Z" with $p_{\mathrm{T}}^{\mathrm{miss}} < 50$ GeV (Fig.).
- 2 light lepton plus a leading tau with an OSSF pair "Off-Z" with $p_{\mathrm{T}}^{\mathrm{miss}} < 50$ GeV (Fig.).

The WZ and ZZ backgrounds have systematic uncertainties of 7% and 5%, respectively, arising from the normalization factor measurements. The rare backgrounds have an uncertainty of 50% on the theory cross section, along with the uncertainty of 2.4% due to luminosity measurement. The final misidentified background estimate is assigned an uncertainty of 30%. This uncertainty arises due to the uncertainty on fake rates and additional correction factors. The photon conversion background also has a 7% uncertainty. All other systematic uncertainties are adapted from the table 6.5. Additional uncertainties due to the tau id and isolation(5%) and tau energy scale(3-7%) are also applied.

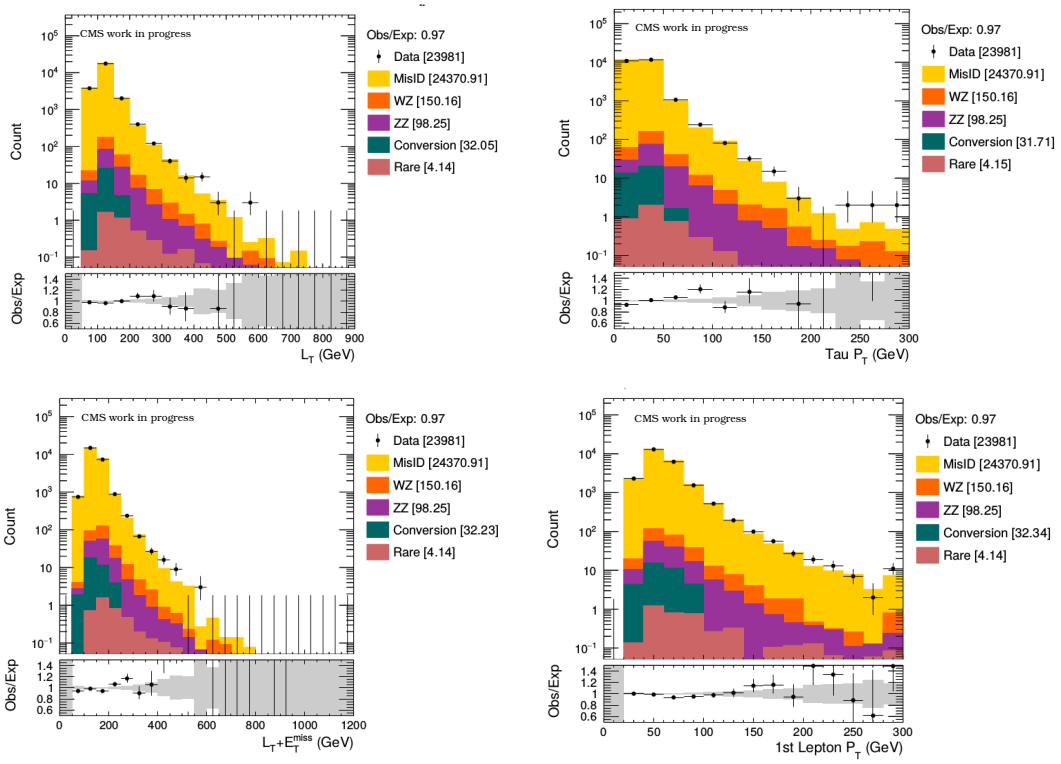

FIGURE 8.3: L_{T} (upper left), Tau p_{T} (upper right), $L_{\mathrm{T}} + p_{\mathrm{T}}^{\mathrm{miss}}$ (lower left), and first lepton p_{T} (lower right) distributions in L2T1 Off-Z with $p_{\mathrm{T}}^{\mathrm{miss}} < 50\,\mathrm{GeV}$ CR (last bin includes overflow). Uncertainty bands in the ratio plots in the lower panel include statistical uncertainties only.

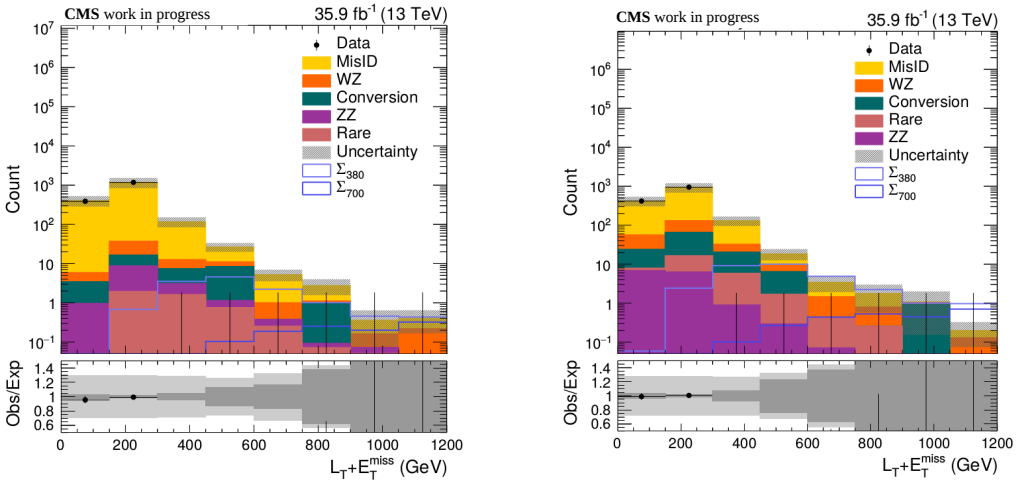

FIGURE 8.4: Partially un-blinded $L_{\mathrm{T}} + p_{\mathrm{T}}^{\mathrm{miss}}$ distributions in L2T1 Above Z(left), and L2T1 OSSF0 (right) signal regions. Uncertainty bands in the ratio plots in the lower panel include statistical as well as systematic uncertainties.

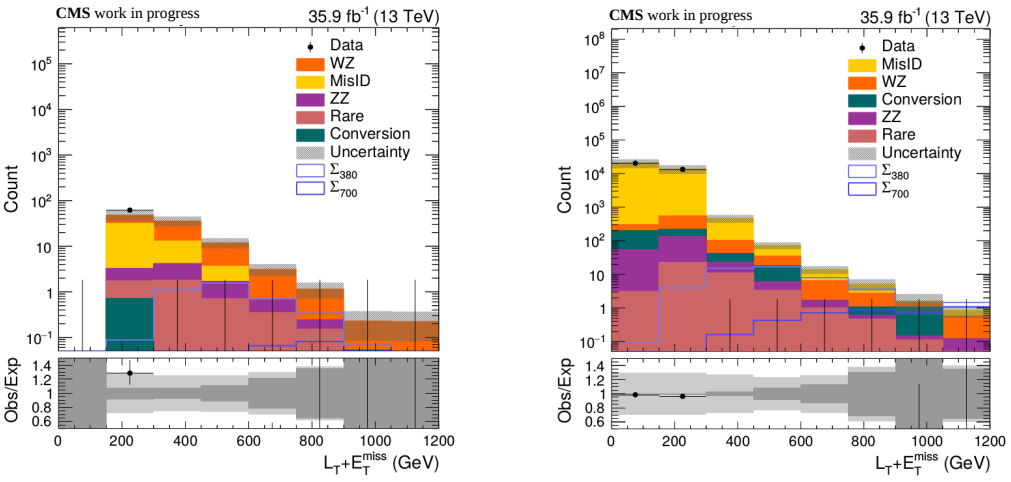

FIGURE 8.5: Partially un-blinded $L_{\mathrm{T}} + p_{\mathrm{T}}^{\mathrm{miss}}$ distributions in L2T1 On-Z(left), and L2T1 Below-Z (right) signal regions. Uncertainty bands in the ratio plots in the lower panel include statistical as well as systematic uncertainties.

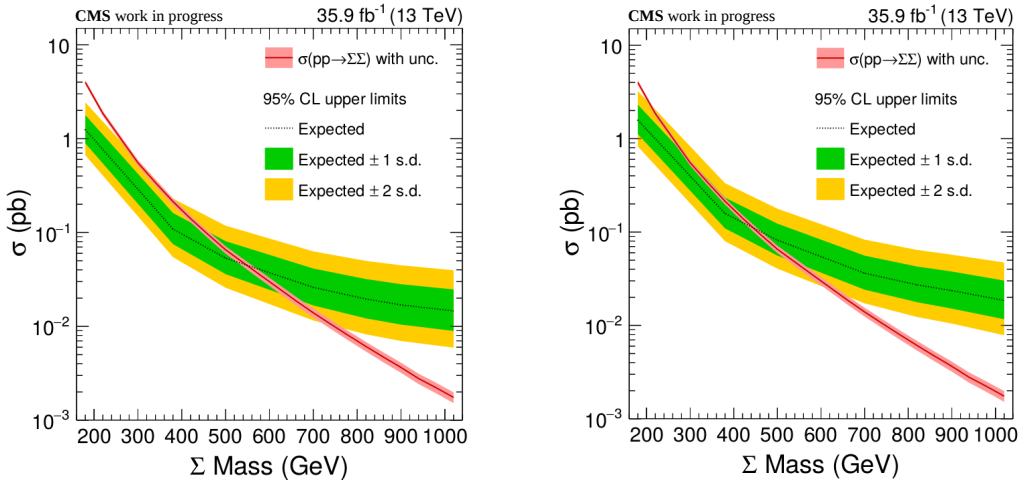

FIGURE 8.6: Expected limit plots in L2T1 channels with democratic(left) and tau only(right) branching ratio scenario.

Figure 8.4, 8.5 shows the partially unblinded $L_{\mathrm{T}} + p_{\mathrm{T}}^{\mathrm{miss}}$ distributions in various signal regions of L2T1 channel. The data is unblinded for first two bins *i.e.* $L_{\mathrm{T}} + p_{\mathrm{T}}^{\mathrm{miss}} < 300$ GeV, since these two bins are background dominated. The data in the bins matches well with predicted backgrounds within the systematic uncertainties described above. I use this result to calculate the expected limit in L2T1 channel in democratic and tau only scenarios and compare them to the results from light lepton only channels.

Using the methods described in Chapter 7, an expected limit is calculated on the production cross-section Σ pairs using the asymptotic CL_S method at 95% CL, where a counting experiment is performed in each signal bin for the statistical analysis. The uncertainties on the mean values of expected signal and background yields are treated

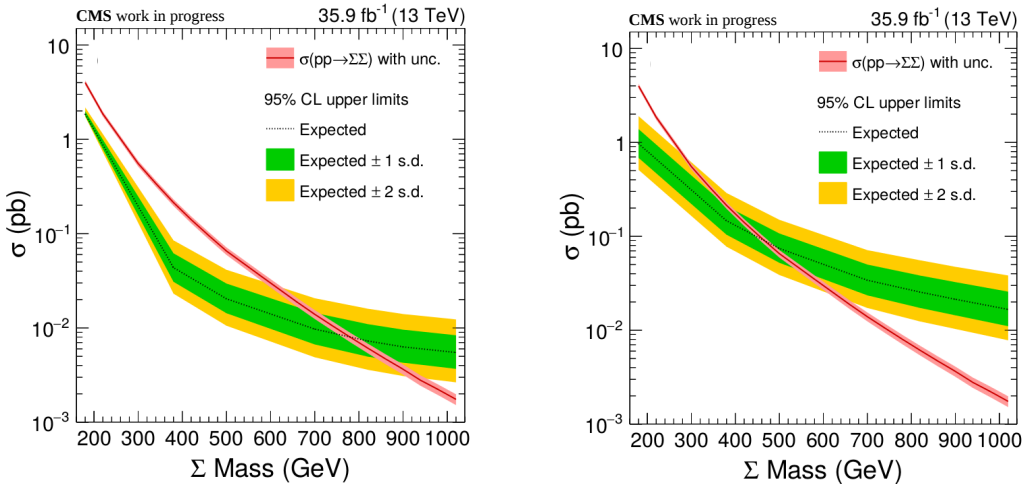

FIGURE 8.7: Expected limit plots in all the channels combined (light lepton plus L2T1) with democratic(left) and tau only(right) branching ratio scenario.

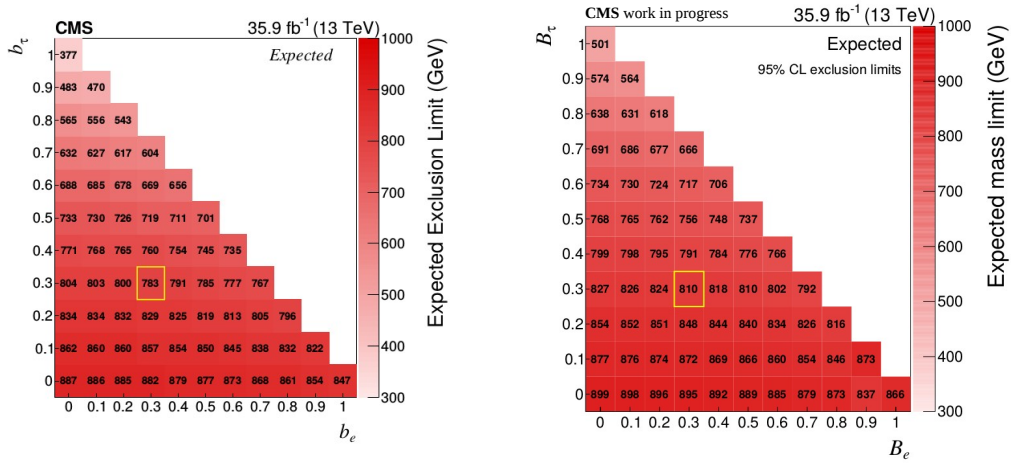

FIGURE 8.8: Comparison of expected limits of published result(left) and possible extension(right) in all branching ratio scenario's represented in 2D plot by varying the tau and electron branching ratios.

as nuisance parameters modeled by log-normal and gamma distributions for systematic and statistical uncertainties, respectively. Statistical uncertainties on the signal and background yields are assumed to be fully uncorrelated, whereas all other systematic uncertainties are assumed to be fully correlated among the 32 signal channels. The left half of the Fig. 8.6 shows the expected limit plots for L2T1 channels with democratic branching ratio scenario whereas the right half shows the expected limits in a scenario when all the final state leptons are tau only i.e. tau branching ratio is 1, where as electron and muon branching ratios are 0. If we combine the expected limits for all light lepton channels (in total 48) from Chapter 7 with the results from the 32 L2T1 channels, the combined expected limit will be as shown in Fig. 8.7.

It is clear from Fig. 8.6 and 8.7 the expected limit is set to rise in the L2T1 channel. After combining all the channels of this analysis (light lepton as well as L2T1 signal regions), The expected limit in tau only scenario shows quite an improvement(From 377 GeV to 501 GeV). Other branching fraction scenario also shows an improvement as compared to light lepton channels as demonstrated in 2D plots of various expected limits in Fig. 8.8.

Finally it can be said that adding L2T1 channel improves expected limit quite significantly in certain branching ratio scenario's. It overall improves the reach of the analysis and might be useful in discovering new physics (if any) hidden in these cases.

Appendix A

List of Data-sets and Triggers

TABLE A.1: Dilepton data samples and corresponding luminosities in 2016.

Dataset Name	Run Range	L [pb^{-1}]
/MuonEG/Run2016B-03Feb2017_ver2-v2/MINIAOD	272007 - 275376	5788
/MuonEG/Run2016C-03Feb2017-v1/MINIAOD	275657 - 276283	2573
/MuonEG/Run2016D-03Feb2017-v1/MINIAOD	276315 - 276811	4248
/MuonEG/Run2016E-03Feb2017-v1/MINIAOD	276831 - 277420	4009
/MuonEG/Run2016F-03Feb2017-v1/MINIAOD	277772 - 278808	3102
/MuonEG/Run2016G-03Feb2017-v1/MINIAOD	278820 - 280385	7540
/MuonEG/Run2016H-03Feb2017_ver2-v1/MINIAOD	280919 - 284035	8391
/MuonEG/Run2016H-03Feb2017_ver3-v1/MINIAOD	284036 - 284044	215
	Total luminosity:	35867
/DoubleMuon/Run2016B-03Feb2017_ver2-v2/MINIAOD	272007 - 275376	5788
/DoubleMuon/Run2016C-03Feb2017-v1/MINIAOD	275657 - 276283	2573
/DoubleMuon/Run2016D-03Feb2017-v1/MINIAOD	276315 - 276811	4248
/DoubleMuon/Run2016E-03Feb2017-v1/MINIAOD	276831 - 277420	4009
/DoubleMuon/Run2016F-03Feb2017-v1/MINIAOD	277772 - 278808	3102
/DoubleMuon/Run2016G-03Feb2017-v1/MINIAOD	278820 - 280385	7540
/DoubleMuon/Run2016H-03Feb2017_ver2-v1/MINIAOD	280919 - 284035	8391
/DoubleMuon/Run2016H-03Feb2017_ver3-v1/MINIAOD	284036 - 284044	215
	Total luminosity:	35867
/DoubleEG/Run2016B-Run2016B-03Feb2017_ver2-v2/MINIAOD	272007 - 275376	5788
/DoubleEG/Run2016C-03Feb2017-v1/MINIAOD	275657 - 276283	2573
/DoubleEG/Run2016D-03Feb2017-v1/MINIAOD	276315 - 276811	4248
/DoubleEG/Run2016E-03Feb2017-v1/MINIAOD	276831 - 277420	4009
/DoubleEG/Run2016F-03Feb2017-v1/MINIAOD	277772 - 278808	3102
/DoubleEG/Run2016G-03Feb2017-v1/MINIAOD	278820 - 280385	7540
/DoubleEG/Run2016H-03Feb2017_ver2-v1/MINIAOD	280919 - 284035	8391
/DoubleEG/Run2016H-03Feb2017_ver3-v1/MINIAOD	284036 - 284044	215
	Total luminosity:	35867

TABLE A.2: List of dilepton triggers used in this analysis. All triggers are unprescaled and a logical or is to be understood over those valid in the same dataset and run range.

Dataset	HLT Path Name	Run Range
DoubleEG	HLT_Ele23_Ele12_CaloIdL_TrackIdL_IsoVL_DZ	272007-284044
DoubleMuon	HLT_Mu17_TrkIsoVVL_Mu8_TrkIsoVVL	272007-280385
	HLT_Mu17_TrkIsoVVL_TkMu8_TrkIsoVVL	272007-280385
	HLT_Mu17_TrkIsoVVL_Mu8_TrkIsoVVL_DZ	280919-284044
	HLT_Mu17_TrkIsoVVL_TkMu8_TrkIsoVVL_DZ	280919-284044
MuonEG	HLT_Mu23_TrkIsoVVL_Ele8_CaloIdL_TrackIdL_IsoVL	272007-280385
	HLT_Mu8_TrkIsoVVL_Ele23_CaloIdL_TrackIdL_IsoVL	272007-280385
	HLT_Mu23_TrkIsoVVL_Ele8_CaloIdL_TrackIdL_IsoVL_DZ	280919-284044
	HLT_Mu8_TrkIsoVVL_Ele23_CaloIdL_TrackIdL_IsoVL_DZ	280919-284044

Appendix B

Dilepton Trigger Efficiencies in Data

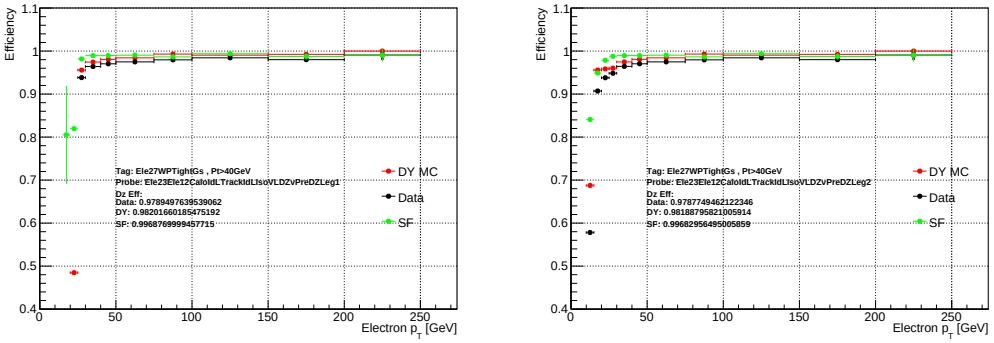

FIGURE B.1: Leading (left) and subleading (right) electron leg efficiencies for the HLT- _Ele23_Ele12_CaloIdL_TrackIdL_IsoVL_DZ trigger path as measured in events with a dielectron pair in the full 2016 dataset and in MC, collected by a single electron trigger. The DZ filter efficiency is found to be 0.98 both in data and MC.

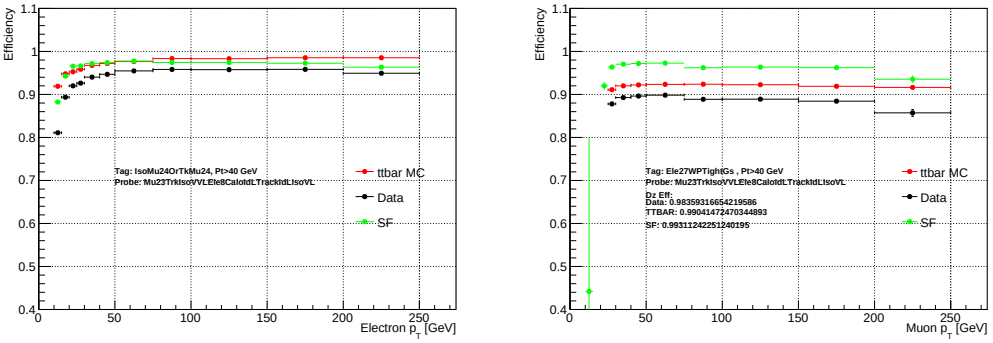

FIGURE B.2: Electron (left) and muon (right) leg efficiencies for the HLT-_Mu23_TrkIso-VVL_Ele8_CaloIdL_TrackIdL_IsoVL trigger path as measured in events with a muon+electron pair in the full 2016 dataset and in MC, collected by a single muon or a single electron trigger, respectively. The DZ filter efficiency is found to be 0.98 in data and 0.99 in MC.

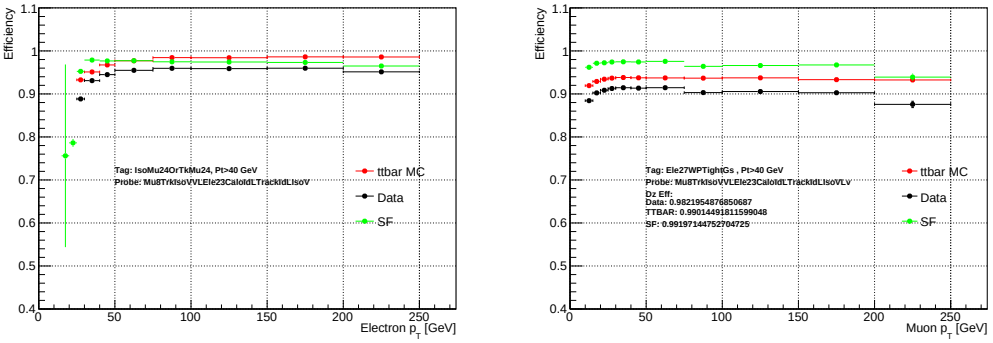

FIGURE B.3: Electron (left) and muon (right) leg efficiencies for the HLT_Mu8_TrkIso-VVL_Ele23_CaloIdL_TrackIdL_IsoVL trigger path as measured in events with a muon+electron pair in the full 2016 dataset and in MC, collected by a single muon or a single electron trigger, respectively. The DZ filter efficiency is found to be 0.98 in data and 0.99 in MC.

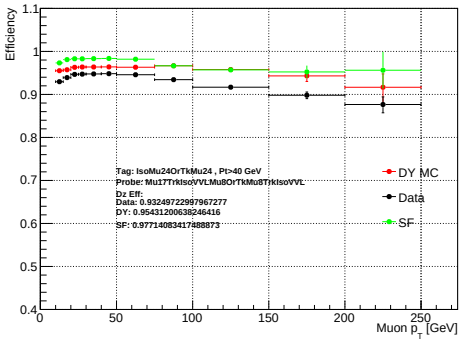

FIGURE B.4: Muon leg trigger efficiency for the HLT_Mu17_TrkIsoVVL_Mu8_TrkIsoVVL_DZ trigger path as measured in events with a dimuon pair in the full 2016 dataset and in MC, collected by a single muon trigger. The DZ filter efficiency is found to be 0.93 in data and 0.95 in MC.

Appendix C

Photon to Lepton Conversion Rate Measurements

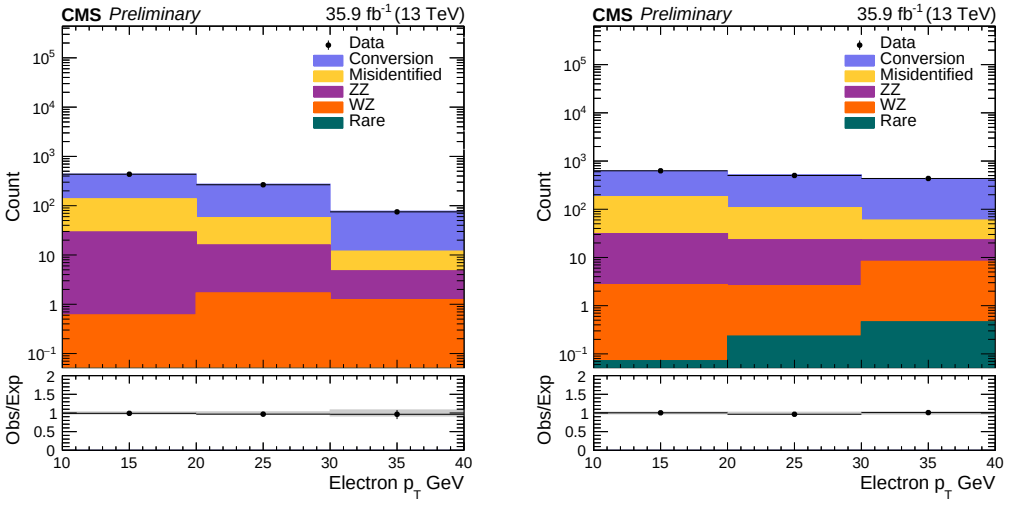

FIGURE C.1: Electron p_{T} distribution in a selection of $\mu^{\pm}\mu^{\mp}e$ events with $L_{\mathrm{T}} < 80$ GeV (left) and $L_{\mathrm{T}} > 80$ GeV (right), where additionally $E_{\mathrm{T}}^{\mathrm{miss}} < 50\,\mathrm{GeV}$, $\mathrm{M}(2\mu)$ is below-Z and $\mathrm{M}(2\mu + \mathrm{e})$ is on-Z. The conversion background component is composed of $\mu^{\pm}\mu^{\mp}\gamma$ events where the photon is assigned and treated as an electron proxy. These bins correspond to the parametrization of photon-to-electron conversion rates as discussed in Section 6.5, and the conversion lepton background component is scaled by the calculated conversion rate such that the total expected and observed number of events match by construction (measurement region). All non-conversion backgrounds are subtracted in the calculation of conversion rates, and a conservative 30% (50%) uncertainty is assigned to the misidentified/WZ/ZZ/rare background components. The last bin also includes overflow events, and the uncertainty bands in the ratio plots in the lower panel include statistical uncertainties only.

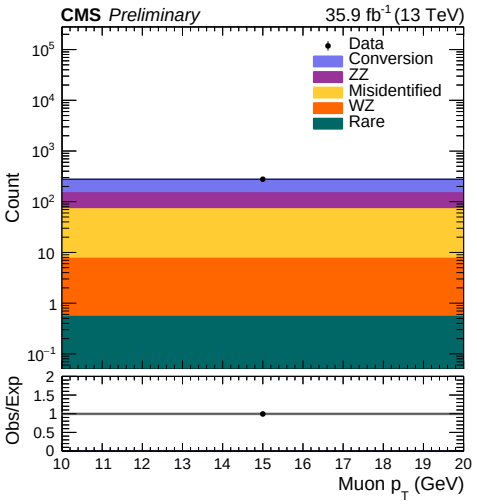

FIGURE C.2: Muon p_{T} distribution in a selection of $e^{\pm}e^{\mp}\mu$ events with $E_{\mathrm{T}}^{\mathrm{miss}} < 50\,\mathrm{GeV}$, where additionaly M($2\mu$) is below-$Z$ and M($2e + \mu$) is on-Z. Since the measurement for muon fake rate is an inclusive measurement, everything is shown in one bin for illustration. The conversion background component is composed of $e^{\pm}e^{\mp}\gamma$ events where the photon is assigned and treated as an muon proxy. This bin corresponds to the parametrization of photon-to-muon conversion rates as discussed in Section 6.5, and the conversion lepton background component is scaled by the calculated conversion rate such that the total expected and observed number of events match by construction (measurement region). All non-conversion backgrounds are subtracted in the calculation of conversion rates, and a conservative 30% (50%) uncertainty is assigned to the misidentified/WZ/ZZ/rare background components.

Appendix D

Contamination due to Misidentified Leptons in $3\ell + \gamma$ Events

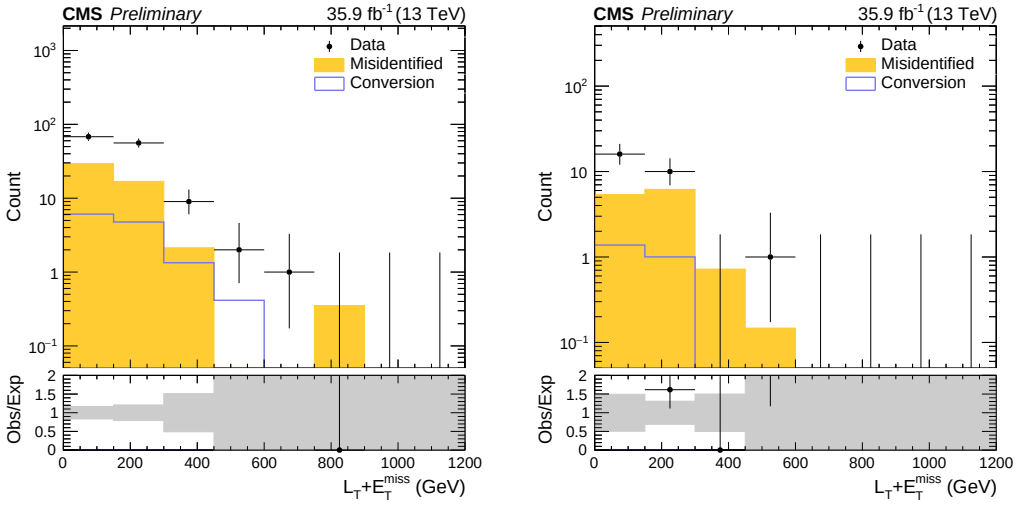

FIGURE D.1: $L_{\mathrm{T}} + E_{\mathrm{T}}^{\mathrm{miss}}$ distributions of $3\ell + \gamma$ events as used in the conversion background estimate in this analysis in L4OSSF1 (left) and L4OSSF2 (right) signal regions. The last bins include overflow events, and the uncertainty bands in the ratio plots in the lower panels include statistical uncertainties only. The data points represent the raw count of $3\ell + \gamma$ events where the photon is randomly assigned an electric charge and a lepton flavor, the misidientifed contribution represents the subset of these events where at least one of the 3 leptons is a misidentified lepton as estimated via the matrix method, and the conversion component given in solid overlay style represents the uncorrected conversion background estimate. The conversion background estimate used in 4 lepton signal regions in this analysis is estimated after subtracting the misidentified fraction of $3\ell + \gamma$ events in each bin.

Bibliography

[1] C. Patrignani et al. Review of Particle Physics. *Chin. Phys.*, C40(10):100001, 2016. doi: 10.1088/1674-1137/40/10/100001.

[2] G. Senjanovic. Neutrino mass: From LHC to grand unification. *Riv. Nuovo Cim.*, 34:1–68, 2011. doi: 10.1393/ncr/i2011-10061-8.

[3] CMS. Lhc guide. [Online; accessed 15-January-2018], Mar 2017. URL https://cds.cern.ch/record/2255762.

[4] CMS. Cms luminosity - public results, 2017. URL https://twiki.cern.ch/twiki/bin/view/CMSPublic/LumiPublicResults. [Online; accessed 15-January-2018].

[5] S. Chatrchyan et al. The CMS experiment at the CERN LHC. *JINST*, 3:S08004, 2008. doi: 10.1088/1748-0221/3/08/S08004.

[6] CMS. *CMS Physics: Technical Design Report Vol. 1: Detector Performance and Software*. Technical Design Report CMS. CERN, Geneva, 2006. URL https://cds.cern.ch/record/922757.

[7] S Chatrchyan et al. Performance of the CMS Hadron Calorimeter with Cosmic Ray Muons and LHC Beam Data. *JINST*, 5:T03012, 2010. doi: 10.1088/1748-0221/5/03/T03012.

[8] S. Abdullin et al. Design, performance, and calibration of CMS hadron-barrel calorimeter wedges. *Eur. Phys. J.*, C55:159–171, 2008. doi: 10.1140/epjc/s10052-008-0573-y.

[9] S Chatrchyan et al. Precise Mapping of the Magnetic Field in the CMS Barrel Yoke using Cosmic Rays. *JINST*, 5:T03021, 2010. doi: 10.1088/1748-0221/5/03/T03021.

[10] CMS. Overview of cms physics goals and detector, 2015. URL https://twiki.cern.ch/twiki/bin/view/CMSPublic/WorkBookCMSExperiment. [Online; accessed 20-January-2018].

[11] CMS Collaboration. Performance of reconstruction and identification of tau leptons in their decays to hadrons and tau neutrino in LHC Run-2. 2016.

[12] ATLAS and CMS Collaborations. Procedure for the LHC Higgs boson search combination in summer 2011. Technical Report CMS NOTE-2011/005, ATL-PHYS-PUB-2011-11, 2011. URL https://cds.cern.ch/record/1379837.

[13] Bruce et al. LHC Run 2: Results and Challenges. Technical Report CERN-ACC-2016-0103, CERN, Geneva, Jul 2016. URL https://cds.cern.ch/record/2201447.

[14] S. L. Glashow. Partial Symmetries of Weak Interactions. *Nucl. Phys.*, 22:579–588, 1961. doi: 10.1016/0029-5582(61)90469-2.

[15] Steven Weinberg. A Model of Leptons. *Phys. Rev. Lett.*, 19:1264–1266, 1967. doi: 10.1103/PhysRevLett.19.1264.

[16] Abdus Salam. Weak and Electromagnetic Interactions. *Conf. Proc.*, C680519: 367–377, 1968.

[17] Peter W. Higgs. Broken Symmetries and the Masses of Gauge Bosons. *Phys. Rev. Lett.*, 13:508–509, 1964. doi: 10.1103/PhysRevLett.13.508.

[18] Peter W. Higgs. Broken symmetries, massless particles and gauge fields. *Phys. Lett.*, 12:132–133, 1964. doi: 10.1016/0031-9163(64)91136-9.

[19] Peter W. Higgs. Spontaneous Symmetry Breakdown without Massless Bosons. *Phys. Rev.*, 145:1156–1163, 1966. doi: 10.1103/PhysRev.145.1156.

[20] F. Englert and R. Brout. Broken Symmetry and the Mass of Gauge Vector Mesons. *Phys. Rev. Lett.*, 13:321–323, 1964. doi: 10.1103/PhysRevLett.13.321.

[21] G. S. Guralnik, C. R. Hagen, and T. W. B. Kibble. Global Conservation Laws and Massless Particles. *Phys. Rev. Lett.*, 13:585–587, 1964. doi: 10.1103/PhysRevLett.13.585.

[22] Alan Martin Francis Halzen. *Quarks and Leptons*. Wiley, 1984.

[23] G. Moore C. Burgess. *The Standard Model, a primer*. Cambridge University Press, 2013.

[24] D. Griffiths. *Introduction to elementry particles*. Wiley-VCH, 2008.

[25] W. Buchmuller and C. Ludeling. Field Theory and Standard Model. In *High-energy physics. Proceedings, European School, Kitzbuehel, Austria, August 21-September, 2005*, 2006. URL https://inspirehep.net/record/726283/files/arXiv:hep-ph_0609174.pdf.

[26] Serguei Chatrchyan et al. Observation of a new boson at a mass of 125 GeV with the CMS experiment at the LHC. *Phys. Lett.*, B716:30–61, 2012. doi: 10.1016/j.physletb.2012.08.021.

[27] Georges Aad et al. Observation of a new particle in the search for the Standard Model Higgs boson with the ATLAS detector at the LHC. *Phys. Lett.*, B716:1–29, 2012. doi: 10.1016/j.physletb.2012.08.020.

[28] Serguei Chatrchyan et al. Evidence for the direct decay of the 125 GeV Higgs boson to fermions. *Nature Phys.*, 10:557–560, 2014. doi: 10.1038/nphys3005.

[29] Julia Woithe, Gerfried J Wiener, and Frederik F Van der Veken. Lets have a coffee with the standard model of particle physics! *Physics Education*, 52(3): 034001, 2017. URL http://stacks.iop.org/0031-9120/52/i=3/a=034001.

[30] A. Pomarol. Beyond the Standard Model. In *High-energy Physics. Proceedings, 18th European School, ESHEP 2010, Raseborg, Finland, 20 Jun. - 3 Jul., 2010*, pages 115–151, 2012. URL https://inspirehep.net/record/1088246/files/arXiv:1202.1391.pdf.

[31] Yorikiyo Nagashima. *Beyond the standard model of elementary particle physics*. Wiley-VCH, Weinheim, USA, 2014. ISBN 9783527411771, 9783527665051. URL http://www.wiley-vch.de/publish/dt/books/ISBN3-527-41177-1.

[32] Pierre Ramond. Journeys beyond the standard model. *Front. Phys.*, 101:1–390, 1999.

[33] Stephen P. Martin. A Supersymmetry primer. pages 1–98, 1997. doi: 10.1142/9789812839657_0001,10.1142/9789814307505_0001. [Adv. Ser. Direct. High Energy Phys.18,1(1998)].

[34] Fred Jegerlehner. The hierarchy problem of the electroweak Standard Model revisited. 2013.

[35] NASA/WMAP Science Team. Wilkinson microwave anisotropy probe, 2018. URL https://map.gsfc.nasa.gov/site/citations.html. [Online; accessed 04-May-2018].

[36] L. Chevalier and M. Spiro. Dark Matter, Dark Energy and the Future of Particle Physics. *Acta Phys. Polon.*, B46(3):729–735, 2015. doi: 10.5506/APhysPolB.46.729.

[37] W. Buchmuller, P. Di Bari, and M. Plumacher. Cosmic microwave background, matter - antimatter asymmetry and neutrino masses. *Nucl. Phys.*, B643:367–390, 2002. doi: 10.1016/S0550-3213(02)00737-X,10.1016/j.nuclphysb.2007.11.030. [Erratum: Nucl. Phys.B793,362(2008)].

[38] A. D. Sakharov. Violation of CP Invariance, C asymmetry, and baryon asymmetry of the universe. *Pisma Zh. Eksp. Teor. Fiz.*, 5:32–35, 1967. doi: 10.1070/PU1991v034n05ABEH002497. [Usp. Fiz. Nauk161,no.5,61(1991)].

[39] Y. Fukuda et al. Measurements of the solar neutrino flux from Super-Kamiokande's first 300 days. *Phys. Rev. Lett.*, 81:1158–1162, 1998. doi: 10.1103/PhysRevLett.81.1158. [Erratum: Phys. Rev. Lett.81,4279(1998)].

[40] Q. R. Ahmad et al. Measurement of the rate of $\nu_e + d \rightarrow p + p + e^-$ interactions produced by ^8B solar neutrinos at the Sudbury Neutrino Observatory. *Phys. Rev. Lett.*, 87:071301, 2001. doi: 10.1103/PhysRevLett.87.071301.

[41] Q. R. Ahmad et al. Direct evidence for neutrino flavor transformation from neutral current interactions in the Sudbury Neutrino Observatory. *Phys. Rev. Lett.*, 89: 011301, 2002. doi: 10.1103/PhysRevLett.89.011301.

[42] K. Abe et al. Upper bound on neutrino mass based on T2K neutrino timing measurements. *Phys. Rev.*, D93(1):012006, 2016. doi: 10.1103/PhysRevD.93.012006.

[43] Julien Lesgourgues and Sergio Pastor. Neutrino mass from Cosmology. *Adv. High Energy Phys.*, 2012:608515, 2012. doi: 10.1155/2012/608515.

[44] Susanne Mertens. Direct Neutrino Mass Experiments. *J. Phys. Conf. Ser.*, 718 (2):022013, 2016. doi: 10.1088/1742-6596/718/2/022013.

[45] Antoine Kouchner. Next-generation atmospheric neutrino experiments. *Physics of the Dark Universe*, 4:60 – 74, 2014. ISSN 2212-6864. doi: https://doi.org/10.1016/j.dark.2014.09.001. URL http://www.sciencedirect.com/science/article/pii/S2212686414000259. DARK TAUP2013.

[46] Ernesto Kemp. The Deep Underground Neutrino Experiment: The Precision Era of Neutrino Physics. *Astron. Nachr.*, 338(9-10):993–999, 2017. doi: 10.1002/asna.201713417.

[47] Shakeel Ahmed et al. Physics Potential of the ICAL detector at the India-based Neutrino Observatory (INO). *Pramana*, 88(5):79, 2017. doi: 10.1007/s12043-017-1373-4.

[48] Vardan Khachatryan et al. Search for heavy neutrinos or third-generation leptoquarks in final states with two hadronically decaying τ leptons and two jets in proton-proton collisions at $\sqrt{s} = 13$ TeV. *JHEP*, 03:077, 2017. doi: 10.1007/JHEP03(2017)077.

[49] Search for a heavy composite Majorana neutrino in the final state with two leptons and two quarks at $\sqrt{s} = 13$ TeV. *Physics Letters B*, 775:315 – 337, 2017. ISSN 0370-2693. doi: https://doi.org/10.1016/j.physletb.2017.11.001. URL http://www.sciencedirect.com/science/article/pii/S0370269317308936.

[50] Giovanna Cottin, Juan Carlos Helo, and Martin Hirsch. Searches for light sterile neutrinos with multitrack displaced vertices. *Phys. Rev.*, D97(5):055025, 2018. doi: 10.1103/PhysRevD.97.055025.

[51] CMS Collaboration. Search for evidence of the type-iii seesaw mechanism in multilepton final states in proton-proton collisions at $\sqrt{s} = 13$ TeV. *Phys. Rev. Lett.*, 119:221802, Dec 2017. doi: 10.1103/PhysRevLett.119.221802. URL https://link.aps.org/doi/10.1103/PhysRevLett.119.221802.

[52] Steven Weinberg. Baryon- and Lepton-Nonconserving Processes. *Phys. Rev. Lett.*, 43:1566–1570, Nov 1979. doi: {10.1103/PhysRevLett.43.1566}. URL https://link.aps.org/doi/10.1103/PhysRevLett.43.1566.

[53] Pavel Fileviez Perez. Type III seesaw and left-right symmetry. *JHEP*, 03:142, 2009. doi: 10.1088/1126-6708/2009/03/142.

[54] Abdesslam Arhrib, Borut Bajc, Dilip Kumar Ghosh, Tao Han, Gui-Yu Huang, Ivica Puljak, and Goran Senjanovic. Collider signatures for the heavy lepton triplet in the type I+III seesaw mechanism. *Phys. Rev. D*, 82:053004, 2010. doi: 10.1103/PhysRevD.82.053004.

[55] F. del Aguila and J. A. Aguilar-Saavedra. Electroweak scale seesaw and heavy Dirac neutrino signals at LHC. *Phys. Lett. B*, 672:158, 2009. doi: 10.1016/j.physletb.2009.01.010.

[56] Roberto Franceschini, Thomas Hambye, and Alessandro Strumia. Type-III seesaw mechanism at CERN LHC. *Phys. Rev. D*, 78:033002, 2008. doi: 10.1103/PhysRevD.78.033002.

[57] Kristian L. McDonald. Probing exotic fermions from a seesaw/radiative model at the LHC. *JHEP*, 11:131, 2013. doi: 10.1007/JHEP11(2013)131.

[58] Ran Ding, Zhi-Long Han, Yi Liao, Hong-Jun Liu, and Ji-Yuan Liu. Phenomenology in the minimal cascade seesaw mechanism for neutrino masses. *Phys. Rev. D*, 89:115024, 2014. doi: 10.1103/PhysRevD.89.115024.

[59] Oliver Sim Brning, Paul Collier, P Lebrun, Stephen Myers, Ranko Ostojic, John Poole, and Paul Proudlock. *LHC Design Report*. CERN Yellow Reports: Monographs. CERN, Geneva, 2004. URL http://cds.cern.ch/record/782076.

[60] Lyndon Evans and Philip Bryant. LHC Machine. *JINST*, 3:S08001, 2008. doi: 10.1088/1748-0221/3/08/S08001.

[61] C E Hill. Ion and electron sources. (CERN-PS-94-36. CERN-PS-94-36-HI):18 p, Sep 1994. URL https://cds.cern.ch/record/276893.

[62] CMS. Cms data quality information, 2017. URL https://twiki.cern.ch/twiki/bin/view/CMSPublic/DataQuality. [Online; accessed 15-January-2018].

[63] CMS Collaboration. CMS luminosity measurements for the 2016 data taking period. CMS Physics Analysis Summary CMS-PAS-LUM-17-001, 2017. URL http://cds.cern.ch/record/2257069.

[64] CMS Collaboration. Pileup removal algorithms. CMS Physics Analysis Summary CMS-PAS-JME-14-001, 2014. URL http://cds.cern.ch/record/1751454.

[65] CMS Collaboration. Pileup json files for run-ii data, 2017. URL https://twiki.cern.ch/twiki/bin/viewauth/CMS/PileupJSONFileforData#Pileup_JSON_Files_For_Run_II. [Online; accessed 04-May-2018].

[66] V Karimki, M Mannelli, P Siegrist, H Breuker, A Caner, R Castaldi, K Freudenreich, G Hall, R Horisberger, M Huhtinen, and A Cattai. *The CMS tracker system project: Technical Design Report*. Technical Design Report CMS. CERN, Geneva, 1997. URL https://cds.cern.ch/record/368412.

[67] Addendum to the CMS tracker TDR. 2000.

[68] *The CMS electromagnetic calorimeter project: Technical Design Report*. Technical Design Report CMS. CERN, Geneva, 1997. URL https://cds.cern.ch/record/349375.

[69] R.M. Brown. Avalanche photodiodes and vacuum phototriodes for the cms electromagnetic calorimeter. *Nuclear Instruments and Methods in Physics Research Section A: Accelerators, Spectrometers, Detectors and Associated Equipment*, 572(1):26 – 28, 2007. ISSN 0168-9002. doi: https://doi.org/10.1016/j.nima.2006.10.160. URL http://www.sciencedirect.com/science/article/pii/S0168900206019693. Frontier Detectors for Frontier Physics.

[70] S Chatrchyan et al. Performance and Operation of the CMS Electromagnetic Calorimeter. *JINST*, 5:T03010, 2010. doi: 10.1088/1748-0221/5/03/T03010.

[71] Luca Brianza. Precision crystal calorimetry in LHC Run II with the CMS ECAL. *JINST*, 12(01):C01069. 13 p, 2017. URL https://cds.cern.ch/record/2275004.

[72] *The CMS hadron calorimeter project: Technical Design Report.* Technical Design Report CMS. CERN, Geneva, 1997. URL https://cds.cern.ch/record/357153.

[73] Vardan Khachatryan et al. Performance of the CMS missing transverse momentum reconstruction in pp data at $\sqrt{s} = 8$ TeV. *JINST*, 10:P02006, 2015. doi: 10.1088/1748-0221/10/02/P02006.

[74] Christian W. Fabjan and Fabiola Gianotti. Calorimetry for particle physics. *Rev. Mod. Phys.*, 75:1243–1286, Oct 2003. doi: 10.1103/RevModPhys.75.1243. URL https://link.aps.org/doi/10.1103/RevModPhys.75.1243.

[75] C. DAmbrosio and H. Leutz. Hybrid photon detectors. *Nuclear Instruments and Methods in Physics Research Section A: Accelerators, Spectrometers, Detectors and Associated Equipment*, 501(2):463 – 498, 2003. ISSN 0168-9002. doi: https://doi.org/10.1016/S0168-9002(03)00431-5. URL http://www.sciencedirect.com/science/article/pii/S0168900203004315.

[76] Seth I. Cooper. Phase i upgrade of the cms hadron calorimeter. *Nuclear and Particle Physics Proceedings*, 273-275:1002 – 1007, 2016. ISSN 2405-6014. doi: https://doi.org/10.1016/j.nuclphysbps.2015.09.157. URL http://www.sciencedirect.com/science/article/pii/S240560141500646X. 37th International Conference on High Energy Physics (ICHEP).

[77] *The CMS magnet project: Technical Design Report.* Technical Design Report CMS. CERN, Geneva, 1997. URL https://cds.cern.ch/record/331056.

[78] *The CMS muon project: Technical Design Report.* Technical Design Report CMS. CERN, Geneva, 1997. URL https://cds.cern.ch/record/343814.

[79] CMS Collaboration. CMS technical design report, volume II: Physics performance. *J. Phys. G*, 34:995–1579, 2007. doi: 10.1088/0954-3899/34/6/S01.

[80] C Anderson, Victor Barashko, S Korenblit, Andrey Korytov, and Guenakh Mitselmakher. Effect of Gas Composition on the Performance of Cathode Strip Chambers for the CMS Endcap Muon System. Technical Report CMS-NOTE-2004-033, CERN, Geneva, Dec 2004. URL https://cds.cern.ch/record/837542.

[81] C. Battilana. The cms muon system: status and upgrades for lhc run-2 and performance of muon reconstruction with 13tev data. *Journal of Instrumentation*, 12(01):C01048, 2017. URL http://stacks.iop.org/1748-0221/12/i=01/a=C01048.

[82] Measurement of the inelastic proton-proton cross section at $\sqrt{s} = 13$ TeV. Technical Report CMS-PAS-FSQ-15-005, CERN, Geneva, 2016. URL http://cds.cern.ch/record/2145896.

[83] M. Aaboud et al. Measurement of the Inelastic Proton-Proton Cross Section at $\sqrt{s} = 13$TeV with the ATLAS Detector at the LHC. *Phys. Rev. Lett.*, 117(18): 182002, 2016. doi: 10.1103/PhysRevLett.117.182002.

[84] Hans Peter Beck. Triggering at high luminosity colliders. *New J. Phys.*, 9:334, 2007. doi: 10.1088/1367-2630/9/9/334.

[85] Vardan Khachatryan et al. The CMS trigger system. *JINST*, 12:P01020, 2017. doi: 10.1088/1748-0221/12/01/P01020.

[86] Alexander Tapper. The CMS Level-1 Trigger for LHC Run II. Technical Report CMS-CR-2016-303, CERN, Geneva, Oct 2016. URL https://cds.cern.ch/record/2230802.

[87] A M Sirunyan et al. Particle-flow reconstruction and global event description with the CMS detector. *JINST*, 12:P10003, 2017. doi: 10.1088/1748-0221/12/10/P10003.

[88] CMS Collaboration. Particle-Flow Event Reconstruction in CMS and Performance for Jets, Taus, and MET. CMS Physics Analysis Summary CMS-PAS-PFT-09-001, 2009. URL https://cds.cern.ch/record/1194487.

[89] Florian Beaudette. The CMS Particle Flow Algorithm. In *Proceedings, International Conference on Calorimetry for the High Energy Frontier (CHEF 2013): Paris, France, April 22-25, 2013*, pages 295–304, 2013. URL https://inspirehep.net/record/1279774/files/arXiv:1401.8155.pdf.

[90] Serguei Chatrchyan et al. Description and performance of track and primary-vertex reconstruction with the CMS tracker. *JINST*, 9(10):P10009, 2014. doi: 10.1088/1748-0221/9/10/P10009.

[91] P. Billoir. Progressive track recognition with a Kalman-like fitting procedure. *Computer Physics Communications*, 57:390–394, December 1989. doi: 10.1016/0010-4655(89)90249-X.

[92] Pierre Billoir and S. Qian. Simultaneous pattern recognition and track fitting by the Kalman filtering method. *Nucl. Instrum. Meth.*, A294:219–228, 1990. doi: 10.1016/0168-9002(90)91835-Y.

[93] R. Mankel. A Concurrent track evolution algorithm for pattern recognition in the HERA-B main tracking system. *Nucl. Instrum. Meth.*, A395:169–184, 1997. doi: 10.1016/S0168-9002(97)00705-5.

[94] R. Fruhwirth. Application of Kalman filtering to track and vertex fitting. *Nucl. Instrum. Meth.*, A262:444–450, 1987. doi: 10.1016/0168-9002(87)90887-4.

[95] CMS Collaboration. Offline primary vertex reconstruction with deterministic annealing clustering. CMS Note 2011/014, 2011.

[96] R Fruhwirth, Wolfgang Waltenberger, and Pascal Vanlaer. Adaptive Vertex Fitting. Technical Report CMS-NOTE-2007-008, CERN, Geneva, Mar 2007. URL https://cds.cern.ch/record/1027031.

[97] Matteo Cacciari, Gavin P. Salam, and Gregory Soyez. The anti-k_t jet clustering algorithm. *JHEP*, 04:063, 2008. doi: 10.1088/1126-6708/2008/04/063.

[98] Matteo Cacciari, Gavin P. Salam, and Gregory Soyez. FastJet user manual. *Eur. Phys. J. C*, 72:1896, 2012. doi: 10.1140/epjc/s10052-012-1896-2.

[99] Gavin P. Salam. Towards Jetography. *Eur. Phys. J.*, C67:637–686, 2010. doi: 10.1140/epjc/s10052-010-1314-6.

[100] Vardan Khachatryan et al. Jet energy scale and resolution in the CMS experiment in pp collisions at 8 TeV. *JINST*, 12(02):P02014, 2017. doi: 10.1088/1748-0221/12/02/P02014.

[101] CMS Collaboration. Determination of jet energy calibration and transverse momentum resolution in CMS. *Journal of Instrumentation*, 6:11002, November 2011. doi: 10.1088/1748-0221/6/11/P11002.

[102] Jane Nachtman, Ismail Okan Atakisi, Milos Dordevic, Mithat Kaya, Ozlem Kaya, Henning Kirschenmann, and Fengwangdong Zhang. Performance of the CMS Jets and Missing Transverse Energy Trigger at LHC Run 2. *PoS*, ICHEP2016:756, 2017.

[103] CMS. Introduction to jet energy corrections at cms, 2015. URL https://twiki.cern.ch/twiki/bin/view/CMS/IntroToJEC#Mandatory_Jet_Energy_Corrections?rev=6. [Online; accessed 22-January-2018].

[104] Vardan Khachatryan et al. Performance of electron reconstruction and selection with the CMS detector in proton-proton collisions at $\sqrt{s} = 8\,\text{TeV}$. *JINST*, 10: P06005, 2015. doi: 10.1088/1748-0221/10/06/P06005.

[105] CMS Collaboration. Egamma phyics object group - cut based electron identification for run-2, 2016. URL https://twiki.cern.ch/twiki/bin/view/CMS/CutBasedElectronIdentificationRun2?rev=39. [Online; accessed 04-May-2018].

[106] CMS Collaboration. Performance of cms muon reconstruction in pp collision events at $\sqrt{s} = 7$. Submitted to *J. Inst.*, 2012.

[107] Giovanni Abbiendi. The CMS muon system in Run2: preparation, status and first results. *PoS*, EPS-HEP2015:237, 2015.

[108] CMS Collaboration. Muon phyics object group - muon identification for run-2, 2016. URL https://twiki.cern.ch/twiki/bin/view/CMS/SWGuideMuonIdRun2?rev=26. [Online; accessed 04-May-2018].

[109] Vardan Khachatryan et al. Reconstruction and identification of lepton decays to hadrons and at CMS. *JINST*, 11(01):P01019, 2016. doi: 10.1088/1748-0221/11/01/P01019.

[110] CMS Collaboration. Performance of τ-lepton reconstruction and identification in CMS. *Journal of Instrumentation*, 7:1001, January 2012. doi: 10.1088/1748-0221/7/01/P01001.

[111] A. K. Kalsi, N. Dhingra, J. B. Singh, V. Bhatnagar, and K. Mazumdar. Tau Reconstruction and Identification with Upgraded CMS Detector at LHC. *Springer Proc. Phys.*, 174:585–589, 2016. doi: 10.1007/978-3-319-25619-1_89.

[112] CMS Collaboration. Tau phyics object group - tau identification for run-2, 2017. URL https://twiki.cern.ch/twiki/bin/view/CMS/TauIDRecommendation13TeV. [Online; accessed 04-May-2018].

[113] P. Minkowski. $\rightarrow e\gamma$ at a rate of one out of 10^9 muon decays? *Phys. Lett. B*, 67:421, 1977. doi: 10.1016/0370-2693(77)90435-X.

[114] Rabindra N. Mohapatra and Goran Senjanoviç. Neutrino mass and spontaneous parity violation. *Phys. Rev. Lett.*, 44:912, 1980. doi: 10.1103/PhysRevLett.44.912.

[115] M. Magg and C. Wetterich. Neutrino mass problem and gauge hierarchy. *Phys. Rev. B*, 94:61, 1980. doi: 10.1016/0370-2693(80)90825-4.

[116] R. N. Mohapatra and G. Senjanovic. Neutrino masses and mixings in gauge models with spontaneous parity violation. *Phys. Rev. D*, 23:165, 1981. doi: 10.1103/PhysRevD.23.165.

[117] J. Schechter and J. W. F. Valle. Neutrino masses in SU(2)⊗U(1) theories. *Phys. Rev. D*, 22:2227, 1980. doi: 10.1103/PhysRevD.22.2227.

[118] J. Schechter and J. W. F. Valle. Neutrino decay and spontaneous violation of lepton number. *Phys. Rev. D*, 25:774, 1982. doi: 10.1103/PhysRevD.25.774.

[119] R. Foot, H. Lew, X. G. He, and G. C. Joshi. See-saw neutrino masses induced by a triplet of leptons. *Z. Phys. C*, 44:441, 1989. doi: 10.1007/BF01415558.

[120] Rabindra N. Mohapatra. Mechanism for understanding small neutrino mass in superstring theories. *Phys. Rev. Lett.*, 56:561, 1986. doi: 10.1103/PhysRevLett.56.561.

[121] R. N. Mohapatra and J. W. F. Valle. Neutrino mass and baryon-number nonconservation in superstring models. *Phys. Rev. D*, 34:1642, 1986. doi: 10.1103/PhysRevD.34.1642.

[122] Weijian Wang and Zhi-Long Han. Naturally small Dirac neutrino mass with intermediate $SU(2)_L$ multiplet fields. *JHEP*, 04:166, 2016. doi: 10.1007/JHEP04(2017)166.

[123] Tong Li and Xiao-Gang He. Neutrino masses and heavy triplet leptons at the LHC: Testability of type III seesaw. *Phys. Rev. D*, 80:093003, 2009. doi: 10.1103/PhysRevD.80.093003.

[124] Frank F. Deppisch, P. S. Bhupal Dev, and Apostolos Pilaftsis. Neutrinos and collider physics. *New J. Phys.*, 17:075019, 2015. doi: 10.1088/1367-2630/17/7/075019.

[125] CMS Collaboration. Search for evidence of Type-III seesaw mechanism in multilepton final states in pp collisions at $\sqrt{s} = 13$ TeV. 2017.

[126] C. Biggio and F. Bonnet. Implementation of the Type III seesaw model in FeynRules/MadGraph and prospects for discovery with early LHC data. *Eur. Phys. J. C*, 72:1899, 2012. doi: 10.1140/epjc/s10052-012-1899-z.

[127] Benjamin Fuks, Michael Klasen, David R. Lamprea, and Marcel Rothering. Gaugino production in proton-proton collisions at a center-of-mass energy of 8 TeV. *JHEP*, 10:081, 2012. doi: 10.1007/JHEP10(2012)081.

[128] Benjamin Fuks, Michael Klasen, David R. Lamprea, and Marcel Rothering. Precision predictions for electroweak superpartner production at hadron colliders with Resummino. *Eur. Phys. J. C*, 73:2480, 2013. doi: 10.1140/epjc/s10052-013-2480-0.

[129] Johan Alwall, Michel Herquet, Fabio Maltoni, Olivier Mattelaer, and Tim Stelzer. MadGraph 5: Going Beyond. *JHEP*, 06:128, 2011. doi: 10.1007/JHEP06(2011)128.

[130] Richard D. Ball et al. Parton distributions for the LHC Run II. *JHEP*, 04:040, 2015. doi: 10.1007/JHEP04(2015)040.

[131] Torbjörn Sjöstrand, Stephen Mrenna, and Peter Z. Skands. A brief introduction to PYTHIA 8.1. *Comput. Phys. Commun.*, 178:852–867, 2008. doi: 10.1016/j.cpc.2008.01.036.

[132] S. Chatrchyan et al. Search for heavy lepton partners of neutrinos in proton-proton collisions in the context of the type III seesaw mechanism. *Phys. Lett. B*, 718:348, 2012. doi: 10.1016/j.physletb.2012.10.070.

[133] G. Aad et al. Search for type-III seesaw heavy leptons in pp collisions at $\sqrt{s} = 8$ TeV with the ATLAS detector. *Phys. Lett. D*, 92:032001, 2015. doi: 10.1103/PhysRevD.92.032001.

[134] Search for Type-III Seesaw Heavy Fermions with Multilepton Final States using 2.3/fb of 13 TeV proton-proton Collision Data. Technical Report CMS-PAS-EXO-16-002, CERN, Geneva, 2016. URL https://cds.cern.ch/record/2140978.

[135] CMS Collaboration. Jetmet phyics object group - missing et filters recommendation for run-2, 2017. URL https://twiki.cern.ch/twiki/bin/view/CMS/MissingETOptionalFiltersRun2. [Online; accessed 04-May-2018].

[136] Paolo Nason. A new method for combining NLO QCD with shower Monte Carlo algorithms. *JHEP*, 11:040, 2004. doi: 10.1088/1126-6708/2004/11/040.

[137] Stefano Frixione, Paolo Nason, and Carlo Oleari. Matching NLO QCD computations with parton shower simulations: the POWHEG method. *JHEP*, 11:070, 2007. doi: 10.1088/1126-6708/2007/11/070.

[138] Yanyan Gao, Andrei V. Gritsan, Zijin Guo, Kirill Melnikov, Markus Schulze, and Nhan V. Tran. Spin determination of single-produced resonances at hadron colliders. *Phys. Rev. D*, 81:075022, 2010. doi: 10.1103/PhysRevD.81.075022.

[139] Sara Bolognesi, Yanyan Gao, Andrei V. Gritsan, Kirill Melnikov, Markus Schulze, Nhan V. Tran, and Andrew Whitbeck. On the spin and parity of a single-produced resonance at the LHC. *Phys. Rev. D*, 86:095031, 2012. doi: 10.1103/PhysRevD.86.095031.

[140] Ian Anderson, Sara Bolognesi, Fabrizio Caola, Yanyan Gao, Andrei V. Gritsan, Christopher B. Martin, Kirill Melnikov, Markus Schulze, Nhan V. Tran, Andrew Whitbeck, , and Yaofu Zhou. Constraining anomalous HVV interactions at proton and lepton colliders. *Phys. Rev. D*, 89:035007, 2014. doi: 10.1103/PhysRevD.89.035007.

[141] Andrei V. Gritsan, Raoul Röntsch, Markus Schulze, and Meng Xiao. Constraining anomalous Higgs boson couplings to the heavy flavor fermions using matrix element techniques. *Phys. Rev. D*, 94:055023, 2016. doi: 10.1103/PhysRevD.94.055023.

[142] Torbjörn Sjöstrand, Stephen Mrenna, and Peter Z. Skands. PYTHIA 6.4 physics and manual. *JHEP*, 05:026, 2006. doi: 10.1088/1126-6708/2006/05/026.

[143] Torbjörn Sjöstrand, Stefan Ask, Jesper R. Christiansen, Richard Corke, Nishita Desai, Philip Ilten, Stephen Mrenna, Stefan Prestel, Christine O. Rasmussen, and Peter Z. Skands. An introduction to PYTHIA 8.2. *Comput. Phys. Commun.*, 191: 159, 2015. doi: 10.1016/j.cpc.2015.01.024.

[144] Serguei Chatrchyan et al. Measurement of the $\mathrm{t\bar{t}}$ production cross section in the dilepton channel in pp collisions at $\sqrt{s} = 7$ TeV. *JHEP*, 11:067, 2012. doi: 10.1007/JHEP11(2012)067.

[145] Vardan Khachatryan et al. Search for Third-Generation Scalar Leptoquarks in the $\mathrm{t}\tau$ Channel in Proton-Proton Collisions at $\sqrt{s} = 8$ TeV. *JHEP*, 07: 042, 2015. doi: 10.1007/JHEP11(2016)056,10.1007/JHEP07(2015)042. [Erratum: JHEP11,056(2016)].

[146] Richard C. Gray, Can Kilic, Michael Park, Sunil Somalwar, and Scott Thomas. Backgrounds to Higgs Boson searches from $\mathrm{W}\gamma^* \to \ell\nu\ell(\ell)$ asymmetric internal conversion. 2011.

[147] CMS Collaboration. Jetmet phyics object group - jet energy correction recommendation for run-2, 2016. URL https://twiki.cern.ch/twiki/bin/view/CMSPublic/WorkBookJetEnergyCorrections. [Online; accessed 04-May-2018].

[148] CMS Collaboration. Jetmet phyics object group - missing et uncertainty prescription for run-ii, 2016. URL https://twiki.cern.ch/twiki/bin/view/CMS/MissingETUncertaintyPrescription?rev=64#Instructions_for_8_0_X_X_26_patc. [Online; accessed 04-May-2018].

[149] CMS Collaboration. Jetmet phyics object group - jet resolution uncertainty prescription for run-ii, 2016. URL https://twiki.cern.ch/twiki/bin/view/CMS/JetResolution?rev=56. [Online; accessed 04-May-2018].

[150] CMS Collaboration. Egamma physics object group - electron scale and resolution uncertainty recommendation for run-ii, 2016. URL https://twiki.cern.ch/twiki/bin/view/CMS/EGMSmearer#ECAL_scale_and_resolution_co_AN1. [Online; accessed 04-May-2018].

[151] CMS Collaboration. Muon physics object group - muon scale and resolution uncertainty recommendation for run-ii, 2016. URL https://twiki.cern.ch/twiki/bin/view/CMS/MuonReferenceScaleResolRun2#RefRun. [Online; accessed 04-May-2018].

[152] CMS Collaboration. Search for SUSY in same-sign dilepton events at 13 TeV. Technical Report CMS-PAS-SUS-16-020, 2016.

[153] Thomas Junk. Confidence level computation for combining searches with small statistics. *Nucl. Inst. Meth. A*, 434:435, 1999. doi: 10.1016/S0168-9002(99)00498-2.

[154] A. L. Read. Presentation of search results: the CL_s technique. In *Durham IPPP Workshop: Advanced Statistical Techniques in Particle Physics*, page 2693, Durham, UK, March 2002. doi: 10.1088/0954-3899/28/10/313. [J. Phys. G 28 (2002) 2693].

[155] Glen Cowan, Kyle Cranmer, Eilam Gross, and Ofer Vitells. Asymptotic formulae for likelihood-based tests of new physics. *Eur. Phys. J. C*, 71:1554, 2011. doi: 10.1140/epjc/s10052-011-1554-0. [Erratum: 10.1140/epjc/s10052-013-2501-z].

[156] K. Cranmer. Statistical challenges for searches for new physics at the LHC. 2008. URL https://cds.cern.ch/record/1021125.

[157] Alexander L. Read. Modified frequentist analysis of search results (The CL(s) method). In *Workshop on confidence limits, CERN, Geneva, Switzerland, 17-18 Jan 2000: Proceedings*, page 81, 2000. URL http://weblib.cern.ch/abstract?CERN-OPEN-2000-205.